Study of Linear and Nonlinear Talbot Effects for Sensing Applications

A thesis submitted in partial fulfilment of

the requirements for the degree of

Doctor of Philosophy

by

Saumya Jyoti Sarkar

(Roll No. 19330017)

Under the supervision of

Prof. Goutam K. Samanta

Professor

Atomic, Molecular and Optical Physics Division

Physical Research Laboratory, Ahmedabad, India

DISCIPLINE OF PHYSICS

INDIAN INSTITUTE OF TECHNOLOGY GANDHINAGAR

2024

To

my family

Declaration

I declare that this written submission represents my ideas in my own words and where others' ideas or words have been included, I have adequately cited and referenced the original sources. I also declare that I have adhered to all principles of academic honesty and integrity and have not misrepresented or fabricated or falsified any idea/data/fact/-source in my submission. I understand that any violation of the above will be cause for disciplinary action by the Institute and can also evoke penal action from the sources which have thus not been properly cited or from whom proper permission has not been taken when needed.

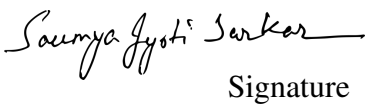

Signature

Name: Saumya Jyoti Sarkar

(Roll No: 19330017)

Date: 16/10/2024

CERTIFICATE

It is certified that the work contained in the thesis titled **"Study of Linear and Non-linear Talbot Effects for Sensing Applications"** by Mr. Saumya Jyoti Sarkar (Roll No. 19330017), has been carried out under my supervision and that this work has not been submitted elsewhere for a degree.

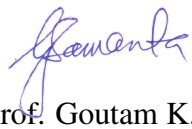

Prof. Goutam K. Samanta
Professor
Atomic, Molecular and Optical Physics Division,
Physical Research Laboratory,
Ahmedabad, India.

(Thesis Supervisor)

Date: 01/10/2024

Acknowledgments

This thesis would not have been possible without the incredible support and guidance of many individuals. I am deeply grateful to all of those who made me capable of writing this thesis.

First and foremost, I would like to express my deepest gratitude to my supervisor, Prof. Goutam Kumar Samanta, for his invaluable guidance, insight, and unwavering support throughout the course of my research. His expertise and constant encouragement have helped me navigate the complexities of nonlinear optics and diffractive optics, and I am profoundly thankful to him for all the insightful discussions and providing lab facilities in every possible way, even in COVID time and afterwards. We also used to play football together in our Vikramnagar and Thaltej ground. It has left a remarkable impression on my mind, in spite of having injuries. It was really wonderful for me to work under his supervision.

In addition, I would like to extend my heartfelt thanks to my DSC members, Dr. Mudit Kumar Srivastava, Dr. Naveen Chauhan, and Prof. Partha Konar, for their thorough review of my work. Their support, guidance, and patience have been invaluable throughout this process. Their constructive feedback and encouraging demeanor consistently motivated me in my thesis work. Our discussions during DSC meetings and area seminars greatly deepened my understanding of my research.

I would like to sincerely thank PRL for providing the essential resources that made my research possible. I am grateful to the members of the PRL academic committee for their valuable insights and encouragement throughout my journey. A special thanks to Prof. R. P. Singh, whose mentorship and support have been a constant source of motivation. I also wish to extend my appreciation to the Director, PRL for ensuring

a well-structured support system. I am also deeply thankful to the academic and administrative staff at IIT Gandhinagar for their assistance with the registration process and their role in facilitating the Ph.D. degree.

Moreover, I would like to take this opportunity to express my heartfelt gratitude to all my teachers, from every stage of my education, who nurtured my passion for physics. I am especially grateful to Partha Banerjee from my school, Dr. Sanat Kumar Manik, Prof. Debashis Bhattacharya, and Dr. Atanu Dan from my college years, as well as Prof. Partha Mitra, Dr. Abhijit Chakaraborty, and Prof. Tanmoy Banerjee from my university, and Prof. V Balakrishnan for his insightful online lectures throughout the years following my BSc. Their unwavering support and mentorship have been crucial in helping me achieve this significant milestone and complete my doctoral thesis.

I want to express my heartfelt gratitude to my friends who have made my life simpler and supported my growth, shaping me into the person I am today. In the lab, Sandeep has always been my go-to for any challenge, offering thoughtful advice—whether academic or personal. Vimlesh da, with his blend of high professionalism and selflessness, has consistently made my life easier, whether by automating the translation stage or retrieving my lab data. Anirban da, like a caring elder brother, inspires me with his passion for academia, and he's also a fantastic cook, hosting most of our gatherings with warmth and generosity. Shreya has been a constant source of support, whether in personal matters or tirelessly proof-reading my thesis. Anupam is the most energetic person I've met, bringing vibrancy to our group. My deep discussions with Subith gave me immense joy in exploring Physics, while Bharath's generosity and computational skills have made my life easier. Tanya, being a benevolent friend, has always been there during my troubles. I am grateful to Chahat, Ayan, Milan, Sanjan, Rutuj, Soumya Kohli, Swagata, Kamalesh, Amrit, Niladri, Amritash, and Aloke

for always being there whenever I needed help. I also want to thank Vardaan, Pooja, JK, Arijit da, Jayanth, Ayan da, Sharika, Satya, and Anju for their unwavering support.

My five years in Ahmedabad were deeply enriched by friends like Birendra, Vineet, Sanjay, Trinesh, Kimi, Neha, Rithvik, Santunu, Sandipan, Aditya, Arup, Wafikul, Malika, Arijit, Soumik, Dibyendu, Goldy, Sana, and Subham da. I will miss PRL and Ahmedabad dearly because of you all. From late-night parties to our "clouded thoughts at night," I'll cherish every moment. My heartfelt thanks to Vikash, Naren, Gourav, Bijoy, Kshitiz, Ajayeta, Swagatika, Bharti, Yogesh, Satyam, Kiran, Varsha, Shreya Mehta and Arup Chakrobarty for always being there. A special thanks to Jhuma for her constant support and to Tanya Srivastava for forcing me find my mental balance and spiritual growth.

I must also thank my childhood friends—Bishal, Emam, and Riju—who shaped my early years, as well as my college friends—Joy, Partha, Sandip, Tania, Zeba, Gourab, Ayan, Tanju, Soumya, Subhadip, Subir, Sharbashish, and Atmadip—and my university friends—Moumita, Sayantani, Tapas, and Bidisha Di—who have been essential part to my journey.

I would also like to extend my heartfelt thanks to my football friends at Vikram Nagar, who helped me maintain balance in life. Rishi Da, Deepak, Chandan, Uttam, Suna, Aravind, and Arvind Sir, your camaraderie on and off the field gave me the perfect escape when I needed it most.

I am also grateful to all the PRL support staff, who made our hostel a wonderful place to live, and the canteen staff, who kept us fed for five years while patiently listening to our complaints.

Lastly, I am deeply grateful to my family, without whom none of this would have

been possible. Maa, Baba, Thakuma, Dada, Vicky, and every member of my family have been my constant pillars of strength, supporting me through every chapter of my life, especially in my academic journey. Words will never be enough to express my gratitude for their sacrifices, love, and unwavering belief in me. My exuberance is a reflection of their endless encouragement, and I owe it all to them.

Abstract

Talbot length, the distance between two consecutive self-image planes along the propagation axis for a periodic diffraction object (grating) illuminated by a plane wave, depends on the period of the object and the wavelength of illumination. This thesis demonstrates a novel approach to control the Talbot length in both pump and second harmonic frequencies, offering a tunable range for the Talbot effect. Using a 25 μm grating period and 632.8 nm wavelength laser, we produced long range tunable Talbot length that is 25 times greater than its original Talbot length. We also discussed the limitations of the range of tunable Talbot length. In another experiment, by employing a microlens array (MLA) illuminated at 1064 nm and projecting onto a 1.2-mm-thick BiBO crystal, we observed the second harmonic Talbot effect at 532 nm with a Talbot length twice that of the fundamental wavelength. However, we overcame the usual fixed dependence of Talbot length on the object period and illumination wavelength by applying a Fourier transformation-based experimental framework. This method enabled independent control over the Talbot lengths in both the pump and second harmonic frequencies, allowing us to tune the pump Talbot length from 26 cm to 62.4 cm and the second harmonic Talbot length from 12.4 cm to 30.8 cm, providing significantly increased flexibility for generating long-range self-images in various experimental configurations.

Another core contribution of this work is the demonstration of nonlinear frequency upconversion of the Talbot effect with tunable Talbot lengths, with remarkably high nonlinear efficiency. By focusing the 1064 nm laser onto the BiBO crystal and placing the MLA at suitable position, we achieved high-efficiency nonlinear upconversion of the Talbot effect. This process resulted in a single-pass conversion efficiency of 2.91% W^{-1}, which represents an enhancement by a factor of 10^6 compared to previously

reported results. The ability to adjust the Talbot length in both fundamental and second harmonic beams provides a flexible framework for controlling the positions of Talbot planes. This flexibility eliminates the need for adjustments of wavelength or grating period, facilitating the generation of desired self-images in specific spatial planes for applications requiring precision, such as Talbot lithography and advanced photonic systems.

The tunable Talbot length also proves effective for sensing minute variations in the period of periodic diffraction objects (gratings). The Talbot effect, which depends on the grating period and the illumination wavelength, offers a straightforward method for measuring the grating period by determining the Talbot length. However, the quadratic dependence of Talbot length on grating period makes traditional techniques less effective for smaller periods or minor variations. Using our tunable Talbot length approach, we measured grating periods as small as a few micrometers and detected sub-wavelength variations with high accuracy. This capability establishes our method as a powerful tool for precision metrology, where variations in grating structures need to be identified with extreme sensitivity.

In addition to its applications in nonlinear optics and grating period sensing, we utilized non-paraxial Talbot effect for studying and correcting aberrations in thick lenses. By measuring the Talbot length of gratings imaged through a system combining a thick lens with short focal length and a thin lens with long focal length and large aperture, we determined the effective focal length of the thick lens for imaging Talbot effect in non-paraxial regime. Our experimental results closely matched our theoretical prediction, highlighting the utility of the non-paraxial Talbot effect in optical sensing applications. The ability to account for lens aberrations using the non-paraxial Talbot effect opens new avenues for improving the precision of optical systems in both imaging and

photonic applications.

Keywords: Talbot effect, Near Field Diffraction, Talbot Length, Upconversion Imaging, Nonlinear Talbot Effct, Sensing Periodicity, Sensing Aberration, Metrology.

Abbreviations

BS	Beam Splitter
PBS	Polarizing Beam Splitter
HWP	Half-Wave Plate
QWP	Quarter-Wave Plate
SHG	Second Harmonic Generation
MLA	Micro-Lens Array
SLM	Spatial Light Modulator
BiBO	Bismuth Borate
PPKTP	Periodically Poled Potassium Titanyl Phosphate
PPLN	Periodically Poled Lithium Niobate
CCD	Charge-Coupled Device

Contents

List of Figures

List of Tables

Chapter 1

Introduction

1.1 Diffraction

The phenomenon of bending of waves through an aperture or an obstacle into a geometrically shadowed region of the aperture or obstacle is commonly known as diffraction. It is not due to an obstacle or a slit; diffraction occurs for any object which creates a substantial change in phase of the incident wave. Since light is an electromagnetic wave, it has a characteristic spatial and temporal frequency which determines the direction of propagation and the time evolution of the wave respectively. A plane electromagnetic wave can be represented by an electric field as,

$$\vec{E}(\vec{r},t) = \vec{E}_0 \ \sin(\vec{k}\cdot\vec{r} - \omega t) \tag{1.1}$$

where $\vec{k}/2\pi$ is the spatial frequency and $\omega/2\pi$ is the temporal frequency of the wave. An electromagnetic wave having definite spatial frequency is called spatially coherent, and having definite temporal frequency is called temporally coherent. In practice,

we do not have absolute coherence but a range within which the wave maintains the coherence, known as the coherence length. In order to have diffraction or interference at any point in space, the superposing waves must be within the range of coherence length.

When an object is placed in path of a spatially monochromatic wave, i.e. a unidirectional wave, the interaction of wave with the object gives rise to some new spatial frequencies which further get separated after certain evolution in space and that is why we see diffraction in far field [1]. However, in the near field, diffraction shows very unique characteristics. This thesis work majorly explores the near-field diffraction, focusing on a particular phenomenon known as the Talbot effect. Before delving into further details, here is a brief account of chronological events.

1.1.1 A brief history of diffraction

The phenomenon of diffraction was first observed and documented by Francesco Maria Grimaldi in the 17th century. In his work "Physico-mathesis de lumine, coloribus, et iride," published posthumously in 1665, Grimaldi described how light bends around obstacles and produces fringes of light and dark bands, coining the term "diffraction" [2]. Christiaan Huygens,in his 1690 work "Traité de la lumière," proposed that every point on a wavefront acts as a source of secondary spherical wavelets, spreading out in the forward direction [3]. Newton with his corpuscular theory of light [4], explained reflection and refraction quite satisfactorily but failed to encompass the phenomenon of diffraction, naming it $inflexion$. Thomas Young's groundbreaking work of double-slit experiment in 1801 demonstrated that light can exhibit interference patterns, providing strong evidence for the wave nature of light [5]. In the early 1820s Augustin-Jean Fresnel made the pivotal contributions to the wave theory of light, through several

experiments and formulating a comprehensive mathematical theory of diffraction [6]. He introduced the Huygens-Fresnel principle, which states that each point on a wavefront is a source of secondary wavelets, and the wave amplitude at any point is the superposition of these wavelets.

Fresnel diffraction applies to situations where the distance between the diffracting object and the observation screen is relatively short, such that the curvature of the wavefront cannot be neglected. This type of diffraction typically occurs in the near-field region and results in complex patterns that are more challenging to analyze compared to Fraunhofer diffraction [7]. Fresnel's work on diffraction included his study of the diffraction by apertures and obstacles of various shapes. His results explained a range of optical phenomena, from the fringes observed around shadows to the intricate patterns seen when light passes through small apertures or edges [1]. Fresnel's mathematical framework for diffraction was countered by Simeon Denis Poisson who predicted the presence of a bright point at the center of the shadow cast by a circular object, now referred to as the Poisson spot or Arago spot. To Poisson's surprise, Dominique Arago experimentally confirmed this prediction, providing strong validation for the wave theory of light [8]. In 1836 H. F. Talbot discovered a remarkable self-imaging phenomenon in near field diffraction of a grating, now known as the Talbot effect [9].

Joseph von Fraunhofer made significant contributions to the study of diffraction, optics, and spectroscopy. Fraunhofer's investigations focused on diffraction patterns produced at a large distance from the diffracting object, or equivalently, in the focal plane of a converging lens. This type of diffraction, known as Fraunhofer diffraction, is the far-field diffraction pattern and is much simpler to analyze than Fresnel diffraction. Fraunhofer diffraction occurs when both the light source and the observation screen

are large distant apart, resulting in near parallel wavefronts. The resulting diffraction patterns are characterized by sharp, well-defined fringes [10]. Fraunhofer's studies included the diffraction patterns produced by single slits, double slits, and diffraction gratings. His work with diffraction gratings led to the development of spectrometry, allowing for the precise measurement of wavelength of light. This was crucial in the analysis of light spectra from various sources, including the sun, leading to the identification of spectral lines known as Fraunhofer lines [11].

James Clerk Maxwell's theory of electromagnetism, formulated in the 1860s, unified the understanding of electricity, magnetism, and light. Maxwell's equations predicted that light is an electromagnetic wave, providing a deeper theoretical foundation for the wave nature of light and diffraction [12]. The early 20th century saw the development of quantum mechanics, which provided new insights into the nature of light and matter. Louis de Broglie proposed that particles such as electrons exhibit wave-like propertieswhich led to the establishment of matter-wave theory. This hypothesis was experimentally demonstrated and confirmed by the electron diffraction experiments of Clinton Davisson and Lester Germer, and independently by George Paget Thomson [13]. X-ray diffraction, discovered by Max von Laue, became a powerful tool for studying the atomic structure of crystals. Laue's discovery was followed by the development of Bragg's law by William Henry Bragg and William Lawrence Bragg, relating the angles of diffracted X-rays to the spacing of crystal planes [14]. This technique revolutionized crystallography and led to the determination of numerous molecular structures, including that of DNA. Electron and neutron diffraction techniques provided complementary methods for investigating atomic and molecular structures. Electron diffraction became essential in material science and chemistry for studying the surface structure of solids [15]. Neutron diffraction, facilitated by the development of nuclear reactors, became invaluable for studying magnetic structures and light

elements in crystals [16].

Dennis Gabor's invention of holography in 1947, for which he later received the Nobel Prize, was another significant application of diffraction principles. Holography involves recording and reconstructing the light field scattered by an object, enabling three-dimensional imaging [17]. Research into surface plasmon resonance (SPR) and metamaterials has expanded our understanding of diffraction at subwavelength scales. SPR involves the excitation of electrons at the surface of a conductor by incident light and has become a cornerstone of modern sensing technologies [18]. Metamaterials, engineered to have properties not found in naturally occurring materials, have led to novel diffraction phenomena, such as negative refraction and the development of superlenses [19]. Photonic crystals, materials with periodic dielectric structures, have enabled precise control over the propagation of light through diffraction and interference effects. These structures have applications in creating highly efficient LEDs, solar cells, and optical fibers [20]. Nanophotonics, the study of light behavior on the nanometer scale, continues to push the boundaries of diffraction and interference, leading to innovations in microscopy and telecommunications. Recent developments in topological photonics have explored how topological states of matter, initially studied in electronic systems, can be manifested in photonic systems. These studies lay out a strong scope for robust, disorder-resistant optical devices. Over the years, research in quantum diffraction has also tremendously evolved, with researchers investigating the diffraction of quantum particles, such as Bose-Einstein condensates and entangled photons, providing deeper insights into quantum mechanics and potential applications in quantum computing and communications [21].

In the upcoming sections, we will begin by exploring the Huygens-Fresnel principle, which forms the foundational basis of wave propagation. This principle will

lead us into a discussion of the Fresnel and Fraunhofer approximations, two important models that simplify the analysis of wave diffraction in different regimes. Specifically, we will examine how these approximations apply to scenarios involving near-field (Fresnel) and far-field (Fraunhofer) diffraction. As we progress, we will identify the conditions under which the Talbot effect emerges, linking it to the Fresnel regime of diffraction.

1.1.2 The Huygens-Fresnel Principle in Rectangular Coordinates

We commence by first stating the Huygens-Fresnel principle in rectangular coordinate system and further work out the approximations for appropriate scenario. As shown in Fig. 1.1, the light is propagating in positive z direction and diffracted by an aperture whose transverse coordinates are given by (x', y') at $z = 0$ plane (as conventional source point). The electric field at the field point (x, y), according to the Huygens-Fresnel

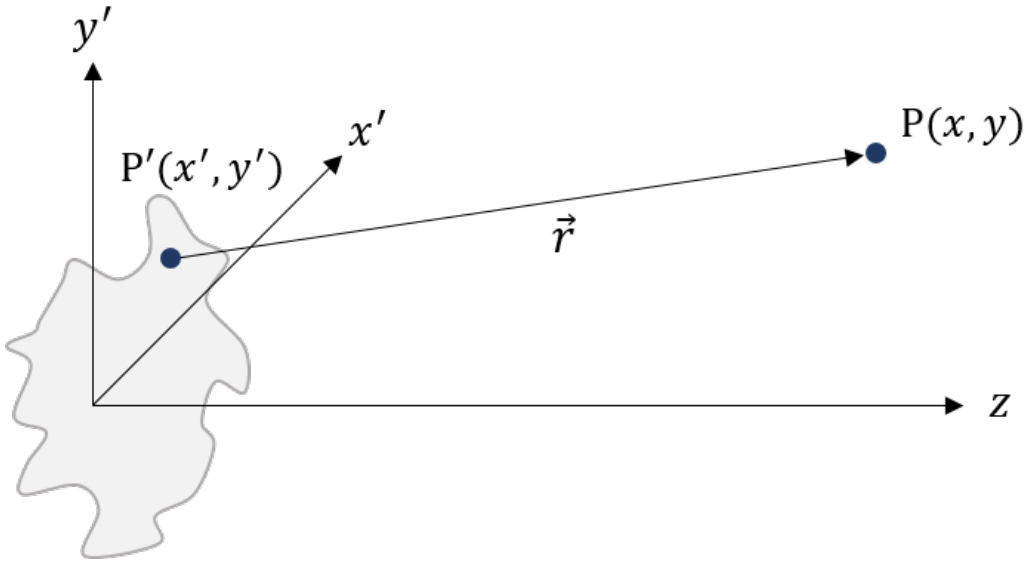

Figure 1.1: Schematic of source point and field point for Huygens-Fresnel principle

principle, can be written as [10]

$$E(x,y) = \frac{z}{i\lambda} \iint_S E(x',y') \frac{\exp(ikr)}{r^2} dx'dy', \tag{1.2}$$

where the distance r is given by

$$r = \sqrt{z^2 + (x-x')^2 + (y-y')^2} \tag{1.3}$$

The above expression comes from scalar theory of Helmholtz equation using the approximation that the field point (x,y) is significantly separated from the source point (x',y') compared to the wavelength of the light (λ), $r >> \lambda$. Now, looking at the major conditions for the two scenarios, i.e. Fresnel and Fraunhofer approximations. The Fraunhofer approximations will be very briefly discussed as part of this work whereas, there will be a detailed discussion on Fresnel approximations owing to the fact that the central ideas of this thesis, which is Talbot effect, is a near-field diffraction phenomenon and hence, falls under Fresnel approximations.

1.1.3 Fresnel approximation

To simplify the Huygens-Fresnel principle and make it more manageable for practical use, we approximate the distance, r, between the source point, $\mathrm{P}'(x',y')$ and the field point, $\mathrm{P}(x,y)$. If we apply binomial expansion approximation of the square root term in Eq. 1.3, we get

$$r \approx z \left[1 + \frac{1}{2} \left(\frac{x-x'}{z} \right)^2 + \frac{1}{2} \left(\frac{y-y'}{z} \right)^2 \right]. \tag{1.4}$$

A natural question to ask at this point is whether the first term in the equation suffices or if other terms are required in the approximation. For instances where r^2 appears in the denominator of the equation, simplifying the expression by using only the first term z (ignoring the rest of the expansion) typically results in a very small and manageable error. This is because the variations in the higher-order terms contribute minimally to the overall result in the denominator, so they can be safely neglected without compromising accuracy. However, when r appears in the exponent, the situation is quite different. The exponent involves a factor k, which is the wave number and is defined as $k = \dfrac{2\pi}{\lambda}$, where λ is the wavelength of the light. In the visible spectrum, k can be extremely large (often greater than 10^6 for typical wavelengths around less than a micron). Even a small error in r due to neglecting higher-order terms in the expansion can result in a significant phase shift because the error gets multiplied by this large number k. Therefore, in the exponent, both terms of the binomial expansion must be retained to ensure precision.

Given this consideration, the expression for the electric field $E(x,y)$ at the field point, $\mathrm{P}(x,y)$ becomes

$$E(x,y) = \frac{e^{ikz}}{i\lambda z} \iint_{-\infty}^{\infty} E(x',y') \; e^{\left\{i\frac{k}{2z}\left[(x-x')^2+(y-y')^2\right]\right\}} \; dx'dy', \tag{1.5}$$

Here, $E(x',y')$ is the field at the aperture plane, and the limits of integration correspond to the boundaries of the aperture.

This equation can be understood as a convolution process, which is a mathematical operation that expresses how the shape of one function is modified by another, to produce a third function. In this context, the convolution represents how the initial light field $E(x',y')$ is modified as it propagates to the observation plane.

The convolution form of the equation is given by,

$$E(x,y) = \int_{-\infty}^{\infty} E(x',y') \;\; h(x-x',y-y') \;\; dx'dy'$$

where $h(x,y)$ is the convolution kernel given by,

$$h(x,y) = \frac{e^{ikz}}{i\lambda z} \exp\left[\frac{ik}{2z}\left(x^2+y^2\right)\right].$$

Alternatively, Eq. 1.5 can be written in a different form by factoring out the quadratic phase term $\exp\left[\frac{ik}{2z}\left(x^2+y^2\right)\right]$ from the integral, yielding

$$E(x,y) = \frac{e^{ikz}}{i\lambda z} e^{i\frac{k}{2z}\left(x^2+y^2\right)} \iint_{-\infty}^{\infty} \left\{E(x',y') e^{i\frac{k}{2z}\left(x'^2+y'^2\right)}\right\} e^{-i\frac{2\pi}{\lambda z}(xx'+yy')} \;\; dx'dy', \qquad (1.6)$$

This form reveals that the resultant field is essentially the Fourier transform of the product of the initial field $e(x',y')$ and a quadratic phase factor.

Both the forms of Eq. 1.5 and Eq. 1.6 are known as the Fresnel diffraction integral, which describes how light propagates and diffracts when it passes through an aperture. When the approximation is valid, the observer is considered to be in the Fresnel diffraction zone, also known as the near-field region of the aperture.

1.1.4 Fraunhofer approximation

When the observation point is located at a much larger distance from the source, the Fraunhofer approximation can be applied, which greatly simplifies the analysis of

wave propagation and diffraction. This approximation is particularly useful in the far-field region, where the wavefronts from the source are almost planar by the time they reach the observation point. Under these conditions, all the spatial frequencies generated due to the aperture are separated in the far field. This separation of spatial frequencies allows for a clearer and more distinct analysis of diffraction patterns, as each frequency component can be treated independently. Mathematically, we can neglect the terms $\frac{x'^2}{2z}$ and $\frac{y'^2}{2z}$ from Eq. 1.4. Thus the Eq. 1.6 can be modified further and becomes,

$$E(x,y) = \frac{e^{ikz}}{i\lambda z} e^{i\frac{k}{2z}(x^2+y^2)} \iint_{-\infty}^{\infty} E(x',y') e^{-i\frac{2\pi}{\lambda z}(xx'+yy')} \, dx'dy', \tag{1.7}$$

Excluding the multiplicative phase factor that precedes the integral, this expression essentially represents the Fourier Transform of the aperture's distribution, evaluated at specific spatial frequencies, $f_x = \frac{x}{\lambda z}$ and $f_y = \frac{y}{\lambda z}$. We will see the importance of spatial frequencies in upcoming chapters.

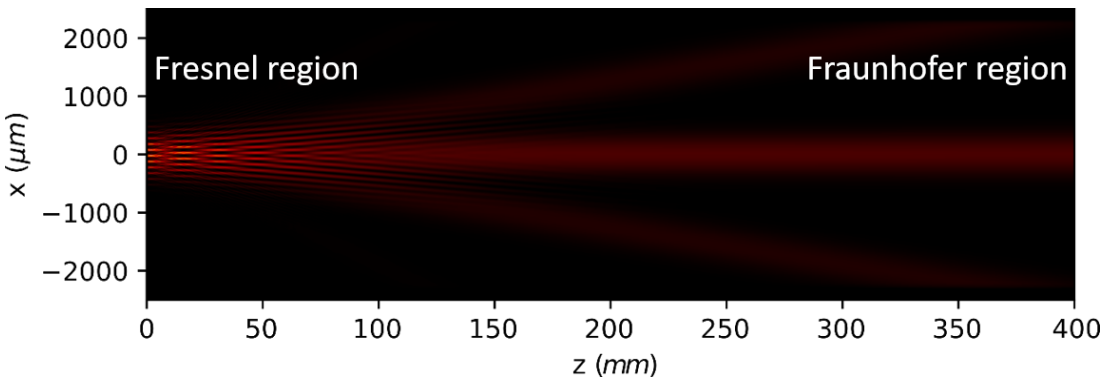

Figure 1.2: Simulation of diffraction from a grating to show Fresnel and Fraunhofer regions

To distinctly identify the regions where Fresnel and Fraunhofer approximations are valid, a simulation of a gaussian beam of wavelength 632.8 nm and beam waist 450 μm getting diffracted by a grating of period 100 μm, is shown in the Fig. 1.2. Here,

one can clearly see how the spatial frequencies get separated in the far field (Fraunhofer region). In the near field (Fresnel region), the overlapping spatial frequencies create a pattern along the propagation direction. Due to a transverse periodicity, a longitudinal periodicity has been generated in the near field (Fresnel region) as shown in the Fig. 1.2. This repetitive pattern along propagation in near field diffraction is known as Talbot effect.

In the next two sections, we will delve into the Talbot effect and explore its various applications. Following this discussion, we will transition to addressing the objective of this thesis.

1.2 The Talbot effect

The Talbot effect, a fascinating phenomenon in wave physics, was first observed by Henry Fox Talbot in 1836 [9]. This effect occurs when a periodic grating is illuminated by coherent light, resulting in the formation of self-images at specific distances known as Talbot distances. These self-images are essentially replicas of the original grating, appearing at regular intervals without the need for a lens. Talbot's discovery, while initially an intriguing curiosity, was mathematically described by Lord Rayleigh in 1881 [22]. From theory of coherent wave diffraction, Rayleigh derived the critical parameter in the Talbot effect named the Talbot length, $Z_T = \frac{2\Lambda^2}{\lambda}$, where Λ represents the grating period and λ is the wavelength of the incident light. The intensity profile is similarly replicated at half the Talbot length, though with a lateral displacement of $\Lambda/2$. This mathematical relationship indicates that the distance at which self-images occur depends on both the physical dimensions of the grating and the properties of the illuminating light. Fig. 1.3 illustrates the Talbot effect due to a grating period Λ illuminated with a light of wavelength λ. The Talbot carpet shown in the Fig. 1.3 is

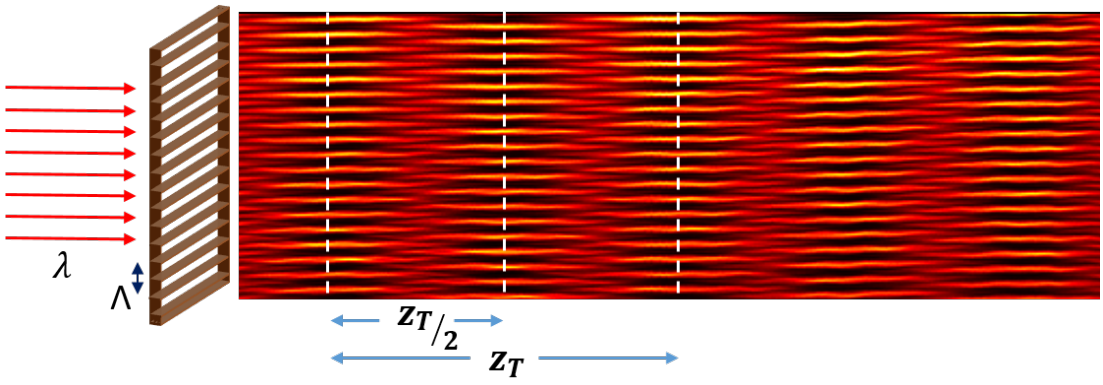

Figure 1.3: Talbot effect arising from a grating period Λ with illuminating wavelength λ

generated using a 25 μm grating period and a 632.8 nm wavelength He-Ne laser in our lab.

Over the years, the Talbot effect has found applications across various scientific fields, including classical optics, nonlinear optics, and quantum optics, each leveraging the unique properties of this phenomenon [23, 24]. Throughout the late 19th and early 20th centuries, several researchers delved deeper into the intricacies of this effect. Winkelmann [25], Weisel [26], and Wolfke [27], for instance, investigated the formation of grating images in microscopy, contributing significantly to the foundational understanding of self-imaging phenomena. In the 1950s, Cowley and Moodie extended these studies by examining Fresnel diffraction fields behind periodic objects [28]. Their work introduced important concepts such as Fourier images and Fresnel images, which describe the different diffraction patterns observed at various distances from the grating [28–31].

In the 1960s, Montgomery further solidified the terminology and understanding of the Talbot effect, coining the term ”self-imaging” to describe the periodic reproduction of the grating images [32]. Montgomery’s contributions were pivotal in standardizing

the concepts of "strong and weak imaging" to describe Fresnel diffraction and Fourier imaging as a whole and hence Talbot effect. This period also saw the rise of affordable coherent light sources, with development of lasers, which rekindled interest in the Talbot effect and facilitated new experimental investigations [24].

1.2.1 Fundamentals of Talbot effect

At its core, the Talbot effect arises from the principles of Fresnel diffraction of coherent waves. When a spatially coherent monochromatic wavefront encounters a periodic grating, it undergoes diffraction, resulting in a series of diffracted waves that interfere with each other. This interference pattern leads to the formation of self-images of the grating at regular intervals along the propagation axis. The Talbot distance, Z_T, is the specific distance at which these self-images recur, and it is determined by the grating period and the wavelength of the light. The phenomenon can be understood through both Fourier optics and Fresnel diffraction theories. In Fourier optics, the Talbot effect is viewed as the constructive and destructive interference of plane waves originating from the periodic grating. These waves combine to form images of the grating at specific distances, known as Talbot planes. The whole picture can be deduced from optical response function [10]. On the other hand, Fresnel diffraction theory provides an intuitive understanding by considering the phase evolution of the diffracted waves as they propagate from the grating [22].

In between two Talbot self-image plane, there exist multiple planes which also reappear along propagation direction in a distance of the Talbot length multiplied by a factor of rational numbers, $(\frac{p}{q})Z_T$ (where p and q are co-prime integers). These planes are called fractional Talbot planes [33, 34]. The fractional Talbot effect, contributing to even fields outside optics [35, 36], gained much attention after Talbot array

illuminators [37].

One of the fascinating aspects of the Talbot effect is its manifestation in both spatial and temporal domains [38]. In the spatial domain, the effect is observed as periodic self-imaging of the grating along the propagation axis. In the temporal domain, known as the temporal Talbot effect, periodic temporal signals propagate through dispersive media, resulting in self-imaging in the time domain [39]. This temporal analogue has practical applications in fields such as ultrahigh-rate optical communications and data processing [40, 41]. In recent times, spatio-temporal Talbot effect has also been observed [42].

1.3 Applications of Talbot effect in several fields

The Talbot effect has found numerous applications in classical optics, quantum optics, nonlinear optics, metrology and other fields as well, leveraging its unique self-imaging properties for various practical uses.

1.3.1 Talbot-Lau interferometry

Talbot-Lau interferometry is an instrumental technique in imaging and metrology, particularly valued for its capacity to operate with particle beams of modest coherence without needing spatially resolving detectors. This technique has been pivotal in high-precision measurements and imaging applications. One of the most prominent uses is in x-ray phase contrast imaging, where it employs gratings to transform phase shifts induced by a sample into measurable intensity variations [43]. This application is crucial for visualizing fine internal structures in various materials, including biological specimens and composite materials, with high contrast [44].

A significant breakthrough in x-ray phase imaging using Talbot-Lau interferometry was demonstrated with synchrotron radiation beams, enabling high-quality imaging in the hard x-ray wavelength range [45]. This method has shown particular promise in medical imaging, enhancing the visibility of soft tissues which are often challenging to image with traditional x-ray techniques [46, 47]. For instance, the internal structure of a small spider and a mouse tail were revealed with remarkable detail using this technique [44]. Moreover, the technique has extended its utility to the study of fundamental physics. It has been used to explore matter wave interference with Na_2 molecules [48], the properties of Bose-Einstein condensates [49] and fullerene molecules [50], providing insights into near field Talbot-Lau interferometry. The ability to operate with heavy particles and the favorable scaling properties of the Talbot-Lau effect make it a robust tool for exploring new frontiers in quantum optics and matter-wave interferometry.

1.3.2 Materials science and plasmonics

The Talbot effect has significant applications in material science, lithography and plasmonics. It has been exploited for advanced lithography techniques, enabling the fabrication of high-resolution patterns necessary for engineering nanoscale devices. Displacement Talbot lithography technique employed various periodic nanopatterns including nanodots, nanoholes, nanorings etc [51]. Talbot lithography is not only usefull in material science domain but has also empowered atomic lithography [48] and cold atom imaging [52].

In the realm of plasmonics, the Talbot effect has been observed with surface plasmon polaritons (SPPs). Plasmonic Talbot carpets have been demonstrated using Au gratings [53]. Plasmon Talbot carpet has also been observed using cylindrical gold nanostructures [54]. These have opened up possibilities for manipulating light at sub-

wavelength scales, which is vital for developing plasmonic circuits and enhancing optical communication systems. Talbot effect of exciton polaritons in a microsturcture semiconductor cavity has been demonstrated theoretically and experimentally [55]. Moreover, the super Talbot effect has been theoretically proposed in indefinite metamaterials, showing that even when the period is much smaller than the incident wavelength, self-imaging can still occur due to the unique properties of these anisotropic metamaterials [56]. This is particularly useful for applications requiring high precision and miniaturization, such as in optical data storage and sensor technology. The ability to convert evanescent waves back into propagating waves in metamaterials further broadens the scope of the Talbot effect in advanced material applications.

1.3.3 Nonlinear optics

The principles of the Talbot effect have been also extended to explore the behavior of light in nonlinear media. Nonlinear optical materials exhibit properties that depend on the intensity of the light passing through them, leading to interesting phenomena such as self-focusing, soliton formation, and harmonic generation [57]. Talbot effect in nonlinear media is a comparatively recent field. Nonlinear interaction of Talbot effect was first time experimentally realized in 2010, using 1D and 2D periodically poled $LiTaO_3$ crystals by spurting laser across the periods leading to direct Second Harmonic Genration (SHG) [58]. Since across the period, the phase matching condition is not satisfied for a PPLT crystal, the nonlinear efficiency was feeble. Later, SHG of fractional Talbot effect was also experimentally demonstrated [59]. Recent reports have demonstrated second-harmonic generation (SHG) of Talbot images using a pump beam modified by a spatial light modulator (SLM) [60]. However, these studies are constrained to lower power levels due to the SLM's lower damage threshold.

Another prominent application of the Talbot effect in nonlinear optics is enhancement of Two Wave Mixing. TWM in a photorefractive crystal transfers energy between beams, and using a photorefractive liquid-crystal light valve, this effect leads to high-gain optical amplification in the Raman-Nath regime. Leveraging the Talbot effect, the TWM gain can be further increased by employing multiple LC light valves [61].

1.3.4 Quantum optics

Advances in quantum optics have been significantly propelled by the Talbot effect. Since Berry's description of quatum carpets [62], a lot of attempts have been made to understand Talbot effect in quantum domain and subsequently different applications showed up. One of the prominent applications is in quantum imaging, where the Talbot effect is employed to surpass the classical diffraction limit. By harnessing the quantum interference of biphotons generated through Spontaneous Parametric Down-Conversion (SPDC), researchers have achieved resolutions unattainable by traditional imaging methods. In 2009, the first theoretical proposal on the Talbot effect in quantum optics was introduced, utilizing entangled photon pairs within the framework of quantum ghost imaging [63]. This study also extended to quantum lithography, revealing a doubled Talbot length compared to the conventional value, which sparked significant interest and further research into higher-order correlation functions. Later, the spatial interference pattern of two-photon correlation functions was examined for a phased array of emitters, demonstrating an N^2 dependence that amplified nonclassical light [64]. They also showed that the spatial distribution of correlations could be controlled by lasers. Further, the Talbot effect in the time domain for entangled photon pairs was explored, observing complex phenomena in coherence propagation [65]. The periodic evolution of photon correlation functions was studied in multimode waveguides, finding that the correlation revival period could exceed the intensity revival period under

certain symmetries [66]. The experimental observations on the second-order Talbot effect using pseudo-thermal light and entangled photon pairs ensured quantum Talbot effects [67].

Quantum Talbot effect has varoius other direction apart from quantum imaging and lithography. The electromagnetically induced quantum Talbot effect has expanded the scope of light-matter interactions using ultracold atoms and molecules at the quantum level [68]. Recently, quantum gravity has also been approached through nonlinear Talbot effect [69].

1.3.5 Metrology

The Talbot effect has greatly advanced metrology, providing highly precise and non-invasive measurement techniques. Utilizing the Talbot effect, researchers have been able to enhance optical metrology by exploiting self-imaging properties of periodic structures, leading to highly accurate surface profiling and wavefront sensing. Apart from applications discussed in section 1.3.1, Talbot interferometry laid out several other applications in metrology as measuring small angle variation due to a tilt of object surface [70]. Self imaging technique has been used to measure intensity and angle of incidence of a light field [71]. In 2016, a miniature Talbot spectrometer was demonstrated 0.9 nm accuracy in optical spectrum, by generating Fourier transform of the spectra recorded using a tilted image sensor [72].

Furthermore, advancements in Talbot lithography have enabled the fabrication of precise and complex microstructures, which are used as calibration standards in metrological applications. This technique allows for the creation of patterns with nanoscale accuracy, providing reference structures that are critical for calibrating measurement instruments [51]. Overall, the integration of the Talbot effect in metrology has led

to significant improvements in measurement accuracy and resolution, enhancing the capabilities of various scientific and industrial applications.

1.4 Objective of the thesis

In various applications of the Talbot effect, the Talbot length serves as a critical parameter that influences system performance, whether in Talbot interferometry, lithography, or sensing techniques. The Talbot length is fundamentally determined by the grating period, Λ and the wavelength of the incident light, λ. Therefore, to achieve self-imaging planes at specific locations, one has to manipulate either the grating period or the wavelength, which can limit flexibility in certain practical scenarios.

To overcome this, a variable Talbot length is necessary, capable of adjusting the position of Talbot planes without requiring changes to the grating period or wavelength. Such a configuration would offer a significant advantage in Talbot interferometry setups and in enhancing sensing capabilities. It would allow more precise control over the self-imaging process and introduce a new dimension of flexibility in various optical systems.

Nonlinear Talbot effects have been studied for over a decade, but a major challenge remains in the efficiency of generation. Improving the efficiency of this nonlinear process, combined with a variable Talbot length, holds potential applications for high-energy domains, such as Talbot lithography. This approach could enable more versatile systems for precise pattern replication and sensing on very small scales.

The central goal of this thesis is to develop an experimental setup, supported by theoretical back up, that enables the generation of a variable Talbot length while integrating it with a highly efficient nonlinear upconversion process. This technique also

shows promise in sensing fine variations in grating periods on a subwavelength scale. Additionally, the use of non-paraxial Talbot effects will be explored as a method for detecting aberrations in thick lenses, expanding the sensing capabilities of non-paraxial Talbot effect.

1.5 Thesis structure

The whole work discussed in this thesis is organized as seven chapters in the thesis. The following are the description of content of each of the thesis chapters.

The first chapter introduces the fundamental concepts of diffraction and the Talbot effect, starting with historical perspectives and progressing toward modern applications. It explains Fresnel and Fraunhofer diffraction region, to understand the domain where Talbot effect occurs. The chapter further delves into fundamentals of Talbot effect, where the periodic self-imaging of gratings is discussed in detail. After discussing the mathematical formulation of the Talbot effect, several applications of the Talbot effect in various domains like Talbot-Lau interferometry, lithography, quantum imaging, and optical metrology are introduced, followed by the objective of the thesis and the thesis structure.

Chapter 2 describes the fundamentals to explore the main part of the thesis, covering the principles of Fourier optics and their role in understanding light propagation through optical systems. It explains how lenses act as Fourier transforming elements, converting incident light into its constituent spatial frequency distributions. This property is crucial for developing a setup for variable Talbot length, which is explored in next three chapters. The chapter then transitions to nonlinear optics, discussing phenomena like second harmonic generation (SHG) and its relevance to the nonlinear Talbot effect. The theoretical treatment of SHG is provided, where the generation of

light at twice the frequency of the input is discussed. This discussion is essential for delving into nonlinear upconversion of Talbot effect as discussed in chapter 4.

In chapter 3, the concept of a tunable Talbot range is explored. Traditionally, the Talbot distance is a fixed value based on the grating period and the wavelength of light. Utilizing an appropriate theoretical framework, we devised a versatile experimental approach grounded in the Fourier transform technique, allowing for continuous and independent control of Talbot lengths for any periodic structure. This method effectively overcomes the strict dependence of self-images on grating period and wavelength. Here, we have produced tunable Talbot lengths of a wide range, up to 25 times greater than the original range. This generic technique can be useful in application areas such as Talbot lithography, Talbot-lau interferometry and various other applications of metrology. In the next two chapters we will extend this technique for nonlinear frequency upconversion of Talbot effect with tunable Talbot length, and sensing variation in periodicity of smaller grating periods.

Chapter 4 investigates the nonlinear Talbot effect using second harmonic generation (SHG). By introducing a nonlinear crystal (BiBO) into the optical system, the traditional Talbot effect is altered, allowing for the formation of new diffraction patterns at second harmonics with modified Talbot length. This experiment has successfully demonstrated single-pass second harmonic generation of the Talbot effect with notable conversion efficiency. Using a microlens array as a two-dimensional periodic object illuminated by pump radiation, we explored the single-pass upconversion of this structure in a BiBO crystal. The study confirmed that the Talbot length is doubled during the upconversion process, specifically through second harmonic generation (SHG). By employing Fourier transformation techniques, we developed a straightforward method to control and tune the Talbot length at both the pump and upconverted

wavelengths, significantly enhancing nonlinear conversion efficiency. This adaptable method allowed for precise adjustments of the Talbot length to target specific planes, enabling the measurement of periodic objects with small pitch sizes without relying on advanced microscopy. The highly efficient nonlinear upconversion demonstrated in this work shows great potential for applications such as Talbot lithography and other high-energy processes involving the Talbot effect.

Chapter 5 begins by discussing the sensitivity of the Talbot effect to periodicity. Because the Talbot effect relies on the periodic nature of a grating to produce self-images, any deviation in the grating's structure or periodicity will alter the resulting Talbot pattern. This sensitivity makes the Talbot effect a valuable tool for detecting subtle changes in periodic structures, i.e. sensing sub-wavelength level variation of grating periods. By tuning the Talbot distance, the periodic structure of optical components can be analyzed with high precision. The sensor effectively detected small periodicity variations in a grating at scales smaller than the wavelength of light used, demonstrating its ability to operate within the challenging subwavelength regime. Conventional optical systems are typically constrained by diffraction limits, which restrict their resolution, but this sensor overcame those limitations by utilizing a tunable Talbot length. By doing so, it eliminated the need for complex, high-magnification microscopes and instead leveraged the Talbot effect to resolve fine structural details directly, offering a simpler and more efficient approach for detecting subtle periodic features.

Chapter 6 extends the application of the Talbot effect to the detection of aberrations, particularly in thick lenses. Aberrations are deviations from the ideal wavefront that can significantly degrade image quality. This chapter explores mathematical expression for the effective focal length of a thick lens in the context of spherical aberra-

tion by examining its influence on the imaging of the non-paraxial Talbot effect, linking the focal length to the grating period used, and the findings are also experimentally verified. This chapter investigates both theoretical and experimental techniques for detecting and quantifying aberrations with the non-paraxial Talbot effect. By studying the changes in Talbot length caused by different grating periods in an imaging setup, in non-paraxial regime, the effective focal length of a thick lens is mapped for a range of grating periods.

The final chapter summarizes the findings of the thesis and discusses potential areas for future research. The thesis has demonstrated the versatility of the Talbot effect, both in its traditional form and in nonlinear optics, for applications in sensing periodicity and aberrations. Future work could involve extending these principles to quantum ghost imaging, exploring nature of electric field in near field diffraction by using vector beams as the input of the grating field, and the phenomenon of superoscillation of the grating field in near field diffraction.

Chapter 2

Some Fundamentals of Fourier and Nonlinear Optics

2.1 Introduction

The analysis of light propagation as a wave phenomena and interactions within optical systems is essential to understand the intricate behavior of periodic structures and their imaging. Two critical theoretical frameworks, Fourier optics and nonlinear optics serve as the foundation for the upcoming chapters which involves working with concepts of Fourier imaging and its nonlinear image-upconversion.

Fourier Optics provides a robust framework for analyzing and understanding how light fields, represented as spatial distributions, are transformed and manipulated within optical systems. Using Fourier analysis, complex optical fields can be broken down into their individual spatial frequency components. This decomposition is crucial for interpreting how various optical elements, such as lenses and apertures, affect the prop-

agation and imaging. The Fourier transform and its associated principles enable us to understand the formation of images and diffraction patterns.

On the other hand, Nonlinear Optics explores the behavior of optical materials under high-intensity light fields. Nonlinear optical effects, such as second-harmonic generation (SHG), occur when higher order (second order for SHG) susceptibility of a material is large enough to induce nonlinear polarizability due to the incident electric field. For the purpose of this thesis work, the nonlinear frequency upconversion of Talbot patterns will be discussed in chapter 4, wherein the interaction of periodic fields with nonlinear crystals will be dealt in details.

In this chapter, we will systematically examine the principles of Fourier optics and nonlinear optics with a focus on their relevance in understanding and analyzing second harmonic generation in context of imaging Talbot effect. By establishing a theoretical foundation in these areas, this chapter will provide the framework necessary for a detailed investigation of how these optical principles inform the analysis of specific techniques in Talbot imaging in the subsequent chapters.

2.2 Fundamentals of Fourier transform in optics

Fourier transform operation translates a function from one domain, such as space or time, to its canonically conjugate domain, spatial frequency or temporal frequency respectively (sometimes multiplied with Planck's constant). In the context of optics, this means transforming a light field from a spatial representation, where we consider the distribution of light intensity across a plane, to a frequency representation, where we analyze how different spatial frequencies contribute to the overall field.

For a one-dimensional optical field, the Fourier transform of a function $E(x)$ is

expressed as,

$$\tilde{E}(f_x) = \int_{-\infty}^{\infty} E(x) e^{-i2\pi f_x x} dx. \tag{2.1}$$

In this equation, f_x represents the spatial frequency, and $\tilde{E}(f_x)$ gives us a measure of 'how much' of a particular frequency is present in the original field $E(x)$.

When dealing with two-dimensional optical fields, which are common in imaging applications, the Fourier transform is also extended to two dimensions,

$$\tilde{E}(f_x, f_y) = \int_{-\infty}^{\infty} \int_{-\infty}^{\infty} E(x,y) e^{-i2\pi(f_x x + f_y y)} dx dy \tag{2.2}$$

Here, f_x and f_y are the spatial frequencies along the x and y axes, respectively. The function $\tilde{E}(f_x, f_y)$ gives us a complete description of spatial frequency contents of the optical field.

Physical interpretation of Fourier transform in the context of optics extends quite interestingly beyond just a mathematical abstraction. Each spatial frequency component corresponds to a plane wave traveling in a specific direction, with the amplitude of the component indicating the strength of that particular wave. Therefore, an optical field can be visualised as a superposition of plane waves with different directions and amplitudes.

One of the most important properties of the Fourier transform in optics is its relationship to convolution. The convolution theorem states that the Fourier transform of the convolution of two functions is equal to the product of their individual Fourier transforms. This property is crucial in understanding how images are formed by optical set-ups, as it explains how the system's point spread function (PSF), which describes how a single point of light is spread out, convolves with the object to produce the final image.

2.3 Lens acting as a Fourier transforming element

Lenses are central to many optical systems, and in the framework of Fourier optics, they are particularly interesting because they act as Fourier transformers. When light passes through a lens, the lens transforms the incoming wavefront into a new wavefront at the focal plane, performing a Fourier transform on the optical field in the process.

To understand this, consider a simple case where a plane wave (which can be thought of as a wave with constant phase across its wavefronts) incident on a lens parallel to its axis. The lens bends the wavefronts, focusing the light at the focal plane on the axis of the lens. Let us say that the plane wave has a spatial frequency, k_0 (k is simply $2\pi f$). Suppose another plane wave with spatial frequency k_1 is incident on the lens at a different angle with x-axis and the lens-axis. These two waves can be represented as $E_0 \sim C_0 e^{ik_0 x}$ and $E_1 \sim C_1 e^{ik_1 x}$, as shown in the Fig. 2.1 with red and orange colored rays respectively. Thus, a wave with many such constituent spatial frequencies can be represented as,

$$E(x) \sim \sum_n C_n e^{ik_n x} \tag{2.3}$$

where the coefficient C_n represents the amplitude of the n-th spatial frequency. Essentially, each plane wave here forms a basis in function space and thus any incident wave consisting of several spatial frequencies gets distributed according to its component elements in k-space as represented by Eq. 2.3. In continuous domain C_n becomes $\tilde{E}(f_x)$ of Eq. 2.1. Hence, this phenomenon of extracting the constituent spatial frequency components through a lens is identified as Fourier transform, and the focal plane of a lens is referred to as Fourier plane.

This property of lenses forms the basis for a wide range of optical systems. For example, in a simple imaging system, light from an object passes through a lens and

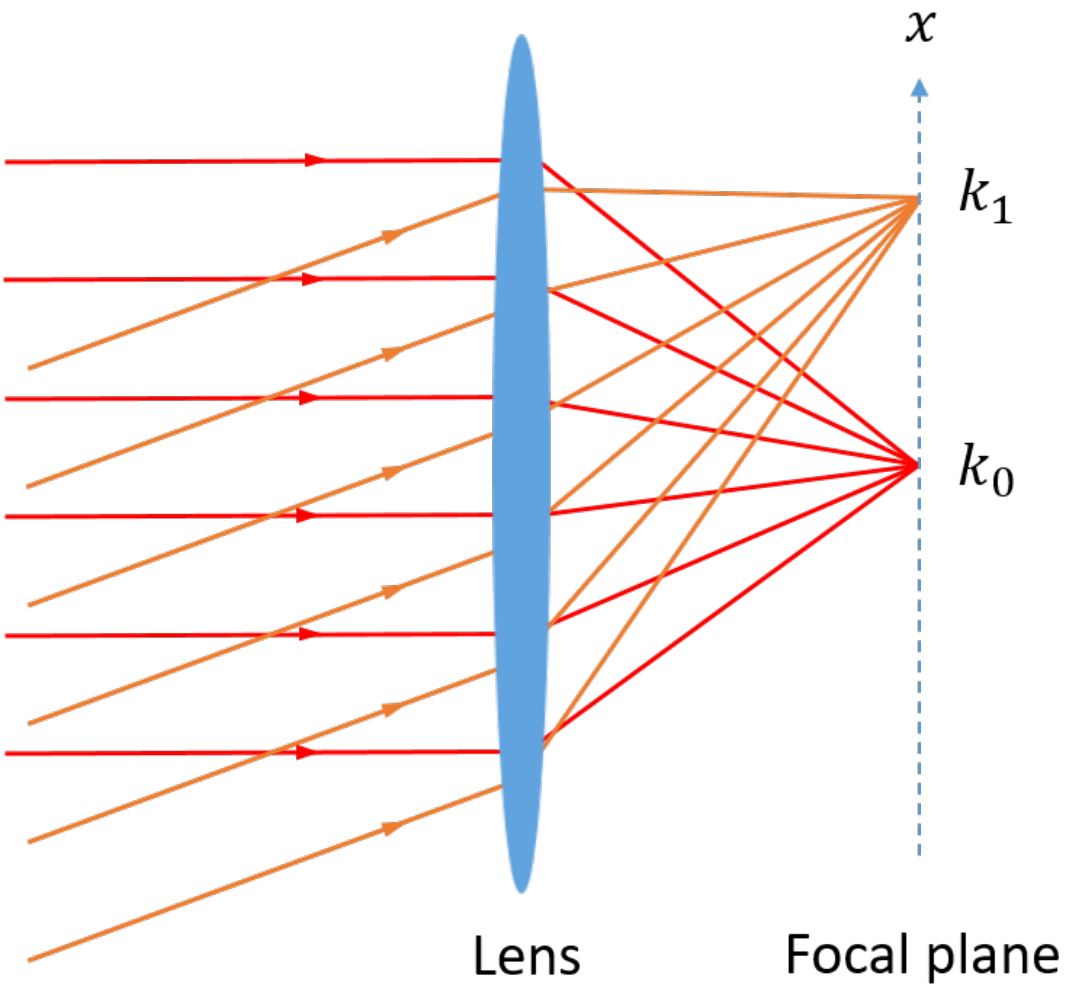

Figure 2.1: Lens acting as a Fourier transforming element by separating the constituent spatial frequencies.

forms an image on a screen or detector. The image can be thought of as the inverse Fourier transform of the light field at the lens's focal plane, hence implying that the lens has effectively transformed the spatial frequencies of the object into the spatial distribution of light in the image plane.

Lenses also play a key role in systems like the $4f$ optical processing setup, where two lenses are used to perform Fourier transformation in sequence. In this setup, the first lens generates the Fourier transform of the object field, and the second lens per-

forms an inverse Fourier transform to produce an image. By placing filters or other optical elements in the Fourier plane between the lenses, one can manipulate the spatial frequency contents of the image, allowing for sophisticated image processing techniques like spatial filtering, edge detection, and contrast enhancement. In chapter 4, we will discuss about using a nonlinear crystal for image-upconversion at the Fourier plane of a lens and an effective spatial filtering due to second harmonic generation process there.

2.4 Image Formation

In Fourier optics, image formation is understood through the concept of spatial frequencies and how they are manipulated by the optical system. Traditional optics explains image formation in terms of ray tracing and geometric optics, but Fourier optics provides a deeper insight by taking into account the effects of the wave nature of light on the final image.

Point spread function (PSF) is an important aspect to understand image formation in Fourier optics, that describes how a single point of light from the object is spread out by a given optical system. The PSF is closely related to the optical transfer function (OTF), which is the Fourier transform of the PSF and describes how different spatial frequencies are transmitted by the system. The OTF provides a complete description of the system's response to different spatial frequencies, allowing us to predict how the system will transform various features of the object, such as edges, fine details, and texture.

Fig. 2.2 shows a $4f$ imaging set up, where the plane waves are shown as parallel rays. The object plane is situated at the front focal plane of the first lens L_1, where the optical field or object is positioned. Light emanating from this plane passes through

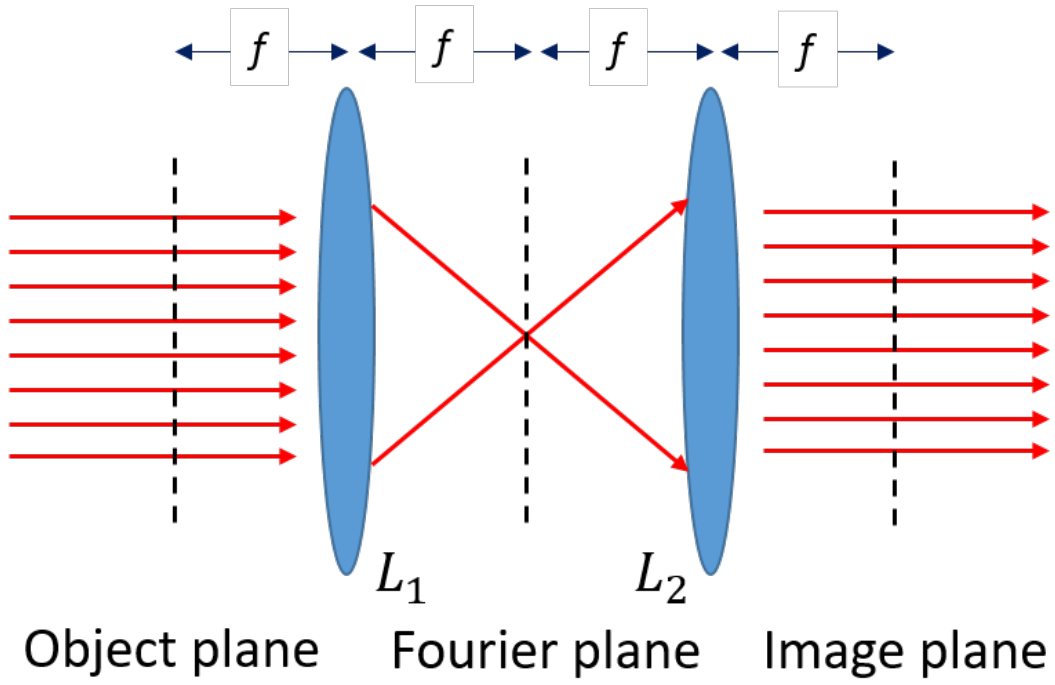

Figure 2.2: $4f$ imaging system with lenses L_1 and L_2. The dashed lines are representing object plne, Forier plane and image plane respectively

L_1, which performs a Fourier transform, converting the spatial information into its frequency domain representation at the Fourier plane, located between the two lenses. Although, at the Fourier plane the beams are shown to be meeting at a point in the Fig. 2.2, the spot size has a diameter greater than $\lambda/2$ for any lens system (where λ is the wavelength of incident light). The second lens L_2, positioned at a focal length f from the Fourier plane, then performs an inverse Fourier transformation on these frequency components. The result is an image formed at the image plane, which is located at the back focal plane of L_2. This setup allows for precise control over spatial frequencies and is instrumental in applications such as optical filtering and image processing. When light from an object passes through an optical system, each point on the object produces a wavefront that propagates through the system. The system's PSF describes how this wavefront is modified, resulting in the formation of an image.

In Fourier optics, we analyze this process by decomposing the object's light field into its spatial frequency components, applying the system's OTF to each component, and then recombining the components to form the final image.

This approach is particularly helpful for understanding how aberrations and other imperfections in the optical system affect image quality. For example, if the system has a limited aperture at the Fourier plane, it will act as a low-pass filter, blocking high spatial frequencies and resulting in a loss of fine detail in the image. Similarly, aberrations can introduce distortions in the phase of the wavefronts, leading to blurring or other artifacts in the final image. The convolution theorem plays a crucial role in this process, as it allows to express the final image as the convolution of the object's light field with the system's PSF. This means that the image is essentially a smeared version of the object, with the extent of the smearing determined by the PSF.

2.5 Fourier transform for different positions of the object

Although the object is placed at the front focal plane of a lens to get exact Fourier transform at the Fourier plane, one can put the object at any other position to achieve the same with different phase factors. We will see three different cases of Fourier transform here as shown in the Fig. 2.3. This section is mainly adapted from [10].

2.5.1 Object placed against the lens

Consider a planar input transparency (a transparent phase-object) with amplitude transmittance $t_A(x,y)$ placed immediately in front of a converging lens with focal length f, as depicted in Fig. 2.3 (a). The input transparency is uniformly illuminated by a

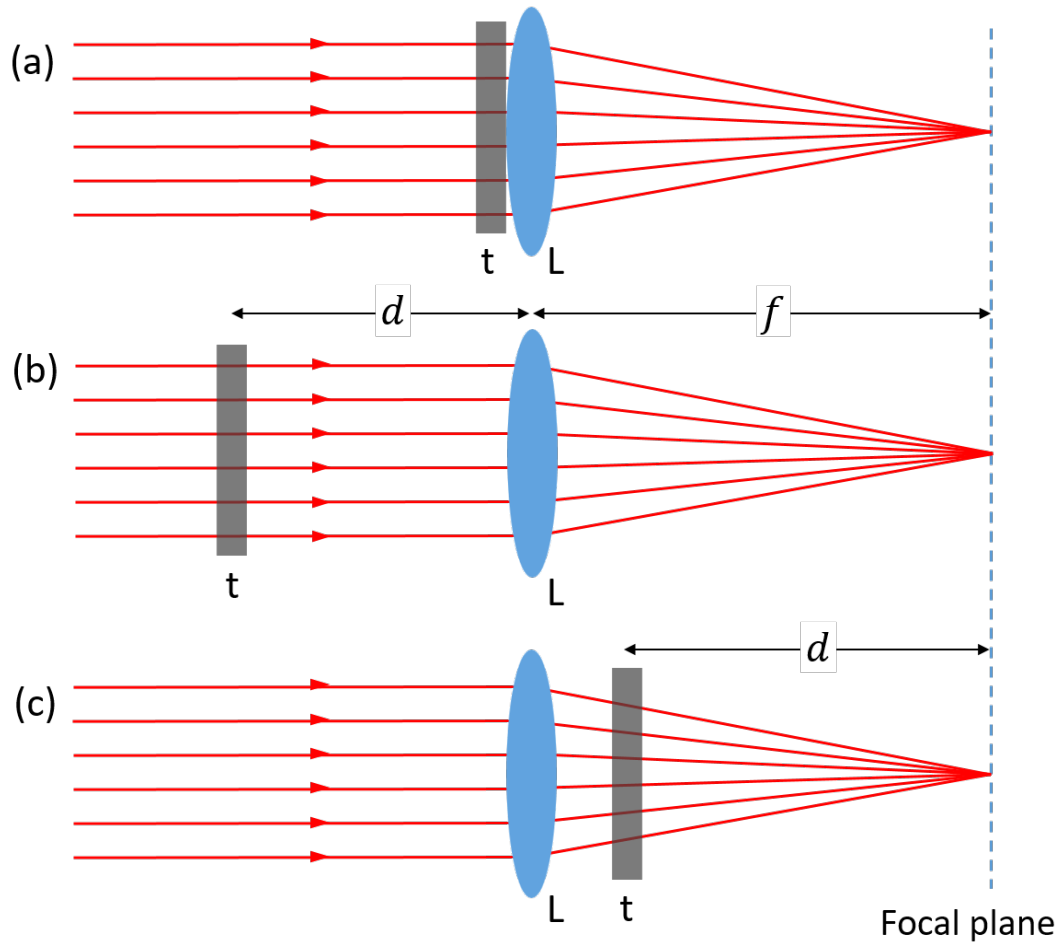

Figure 2.3: Different positions of object,t to get Fourier Transform at the focal plane of the lens, L. Object positions are (a) directly against the lens, (b) d distance apart in front of the lens, and (c) d distance apart in front of the focal plane, behind the lens

normally incident, monochromatic plane wave with amplitude A. The optical field incident on the lens is then given by,

$$E_l(x,y) = At_A(x,y)$$

Since we are using laser source, we assume that the entire input field passes through the lens without any obstruction. The amplitude distribution behind the lens is then modified by $\exp\left(-i\frac{k}{2f}\left(x^2+y^2\right)\right)$, which represents the quadratic phase shift intro-

duced by the lens. This phase shift depends on the coordinates x and y within the plane of the lens and is responsible for focusing the incoming light.

$$E_l'(x,y) = E_l(x,y)\exp\left(-i\frac{k}{2f}\left(x^2+y^2\right)\right)$$

To find the field distribution $E_f(u,v)$ in the back focal plane of the lens, we apply the Fresnel diffraction formula, assuming $z = f$,

$$E_f(u,v) = \frac{\exp\left(i\frac{k}{2f}\left(u^2+v^2\right)\right)}{i\lambda f}\int_{-\infty}^{\infty}\int_{-\infty}^{\infty}E_l'(x,y)\exp\left(-i\frac{2\pi}{\lambda f}(ux+vy)\right)dxdy.$$

Substituting $E_l'(x,y)$ into this expression, and noting that the quadratic phase factors cancel out, the resulting field distribution in the focal plane becomes,

$$E_f(u,v) = \frac{\exp\left(i\frac{k}{2f}\left(u^2+v^2\right)\right)}{i\lambda f}\int_{-\infty}^{\infty}\int_{-\infty}^{\infty}At_A(x,y)\exp\left(-i\frac{2\pi}{\lambda f}(ux+vy)\right)dxdy \quad (2.4)$$

This expression shows that the complex amplitude distribution of the field in the focal plane of the lens is proportional to the two-dimensional Fourier transform of the incident field on the lens as given by Eq. 1.7 in the previous chapter. It's significant to note that Fraunhofer diffraction is typically observed when the distance between the object and the observation plane is very large; however, in this special configuration, the Fraunhofer diffraction can be observed at the focal plane of the lens, even though the plane is relatively close to the lens and that is why we see Fourier transform on the focal plane.

2.5.2 Object placed in front of the lens

Now consider a more general case where the input transparency is placed at a distance d in front of the lens as shown in the Fig. 2.3 (b). The input transparency is again illuminated by a normally incident plane wave with amplitude A, and the amplitude transmittance is $t_A(x,y)$. The Fourier spectrum of the light transmitted by the input transparency is represented by $F_o(f_X, f_Y)$, and the spectrum of the light incident on the lens by $F_l(f_X, f_Y)$, such that

$$F_l(f_X, f_Y) = F_o(f_X, f_Y) \exp\left(-i\pi\lambda d\left(f_X^2 + f_Y^2\right)\right)$$

Neglecting the finite extent of the lens aperture (at least the beam size is smaller than the lens aperture), the field distribution in the focal plane of the lens is

$$E_f(u,v) = \frac{A \exp\left(i\frac{k}{2f}\left(u^2+v^2\right)\right)}{i\lambda f} F_o\left(\frac{u}{\lambda f}, \frac{v}{\lambda f}\right)$$

Substituting the expression for F_o, we obtain,

$$\begin{aligned} E_f(u,v) = & \frac{A \exp\left[i\frac{k}{2f}\left(1-\frac{d}{f}\right)\left(u^2+v^2\right)\right]}{i\lambda f} \\ & \times \iint_{-\infty}^{\infty} t_A(\xi,\eta) \exp\left[-i\frac{2\pi}{\lambda f}(\xi u + \eta v)\right] d\xi d\eta \end{aligned} \tag{2.5}$$

This shows that the amplitude and phase of the light at coordinates (u,v) in the focal plane are directly related to the amplitude and phase of the object's Fourier spectrum at the corresponding spatial frequencies $\frac{u}{\lambda f}$ and $\frac{v}{\lambda f}$. When $d = f$, the quadratic phase factor vanishes, yielding an exact Fourier transform relation.

2.5.3 Object placed behind the lens

Finally, consider the case where the input transparency is positioned behind the lens, at a distance d in front of the rear focal plane as shown in the Fig. 2.3 (c). Imagine a converging spherical wave that is directed towards the back focal point of the lens. The wave illuminates the object, which now lies a certain distance d behind the lens. Due to the convergence, the diameter of the beam illuminating the object decreases in size proportionally with the distance d. The amplitude of this converging spherical wave at the object plane is scaled by the factor $\frac{f}{d}$, since the energy remains conserved as the beam converges.

At the object plane, the effective illuminated region is determined by the intersection of the cone of light rays with the object. If the lens is circular, this means that a circular region of the object, whose diameter is $l\frac{d}{f}$, gets illuminated, where l represents the beam diameter at the lens plane. The amplitude of the spherical wave impinging on the input transparency (object) is $A\frac{f}{d}$, and the illuminated region corresponds to the intersection of the cone of rays with the object plane.

The wave transmitted through the input transparency under the paraxial approximation is described by,

$$E_o(\xi,\eta) = \left(A\frac{f}{d}\right)\exp\left(-i\frac{k}{2d}\left(\xi^2+\eta^2\right)\right)t_A(\xi,\eta)$$

To find the field distribution at the focal plane, we need to apply Fresnel diffraction, which calculates the wave's evolution as it propagates. Since the object is illuminated by a spherical wave, the phase distribution at the object contains a quadratic phase term associated with the curvature of the wavefront. When this quadratic phase term

is included in the Fresnel integral, it cancels out a similar term, simplifying the overall calculation, and the field distribution at the back focal plane becomes,

$$E_f(u,v) = \frac{A\frac{f}{d}\exp\left(i\frac{k}{2d}\left(u^2+v^2\right)\right)}{i\lambda d}\int_{-\infty}^{\infty}\int_{-\infty}^{\infty} t_A(\xi,\eta)\exp\left(-i\frac{2\pi}{\lambda d}(u\xi+v\eta)\right)d\xi\,d\eta$$

This equation shows that, aside from a quadratic phase factor, the field distribution in the focal plane is the Fourier transform of the input transparency. The scaling factor of the Fourier transform depends on the distance d, which can be adjusted to control the size of the transform, providing flexibility in applications like spatial filtering or tunability of effective image size. This particular configuration of Fourier transform will be largely useful in our next chapters.

Now a very essential part of nonlinear optics will be discussed here, which will be important for understanding the context of chapter 4.

2.6 Optical nonlinearity

When an electromagnetic wave interacts with a dielectric material, it generates polarization, which refers to the dipole moment per unit volume. This moment is primarily caused by the displacement of valence electrons from their normal orbits. The magnitude and direction of this polarization are influenced by the strength of the electric field, its direction of propagation, and the polarization of the electric field applied within the medium. The induced polarization, P, can be represented as a power series expansion in terms of the electric field, expressed as,

$$P = \varepsilon_0\left(\chi^{(1)}E + \chi^{(2)}E^2 + \chi^{(3)}E^3 + \ldots\right) = P_{\mathrm{L}} + P_{\mathrm{NL}}$$

Here, ε_0 is the permittivity of free space, E represents the electric field component of the wave, and $\chi^{(m)}$ denotes the susceptibility tensor of the m-th order, with a rank of $(m+1)$. The term for linear polarization, P_L, is given by,

$$P_{\mathrm{L}} = \varepsilon_0 \chi^{(1)} E \tag{2.6}$$

On the other hand, nonlinear polarization, P_{NL}, is written as,

$$P_{\mathrm{NL}} = \varepsilon_0 \left(\chi^{(2)} E^2 + \chi^{(3)} E^3 + \dots \right) \tag{2.7}$$

In everyday situations, the electric field strength is typically small, meaning the polarization induced in the material is directly proportional to the applied field, which can be described by Eq. 2.6. This results in common optical phenomena such as reflection, refraction, dispersion, and diffraction. However, when the electric field becomes sufficiently intense, as in the case of laser light, the displacement of the electron cloud relative to the nucleus becomes nonlinear with respect to the electric field. Consequently, the higher-order terms in Eq. 2.7 become significant, leading to the generation of new frequencies. Laser light is generally required for this, as it provides the necessary intensity to produce these new frequencies. The field of nonlinear optics is often regarded as beginning with the first observation of second-harmonic generation (SHG) in quartz [73], following the invention of the laser in 1960 [74].

Since nonlinear optics is an extensive area, the discussion here will focus primarily on second-order nonlinear interactions, which involve the second-order susceptibility, $\chi^{(2)}$. For more information on other nonlinear interactions, refer to [57].

2.7 Second-order nonlinear processes

The second-order nonlinear polarization is expressed as,

$$P_{\mathrm{NL}} = \varepsilon_0 \chi^{(2)} EE \tag{2.8}$$

where $\chi^{(2)}$ represents the second-order nonlinear susceptibility tensor, which is only present in non-centrosymmetric materials—those without inversion symmetry in their point group. In experimental literature, it is common to use the d-tensor notation instead of $\chi^(2)$, and we will follow that convention. The d-tensor is defined as,

$$\chi^{(2)}_{ijk} = 2d_{ijk}$$

Using the Kleinman symmetry approximation [57], which applies when all interacting frequencies are far from resonances, the second-order susceptibility tensor can be simplified into a 3×6 matrix form,

$$\begin{pmatrix} P_x \\ P_y \\ P_z \end{pmatrix} = 2\varepsilon_0 K \begin{pmatrix} d_{11} & d_{12} & d_{13} & d_{14} & d_{15} & d_{16} \\ d_{21} & d_{22} & d_{23} & d_{24} & d_{25} & d_{26} \\ d_{31} & d_{32} & d_{33} & d_{34} & d_{35} & d_{36} \end{pmatrix} \begin{pmatrix} E_x^2 \\ E_y^2 \\ E_z^2 \\ E_yE_z + E_zE_y \\ E_zE_x + E_xE_z \\ E_xE_y + E_yE_x \end{pmatrix}$$

where K is a degeneracy factor, equal to $1/2$ for processes such as SHG and optical rectification, and 1 for other conversion processes. Now, if the applied electric field is composed of two different frequency components,ω_1 and ω_2, we can express the field

as,

$$E(t) = E_1 e^{-i\omega_1 t} + E_2 e^{-i\omega_2 t} + \text{c.c.}$$

Substituting this into Eq. 2.8, the second-order nonlinear polarization becomes,

$$P_{\text{NL}}(t) = \sum_{n=1,2} P(\omega_n) e^{-i\omega_n t} = \chi^{(2)} \Big[E_1^2 e^{-2i\omega_1 t} + E_2^2 e^{-2i\omega_2 t} + 2E_1 E_2 e^{-i(\omega_1+\omega_2)t} + 2E_1 E_2^* e^{-i(\omega_1-\omega_2)t} + \text{c.c.} \Big] + 2\chi^{(2)} \left[E_1 E_1^* + E_2 E_2^* \right]$$

The first two terms represent second-harmonic generation (SHG), while the third and fourth terms correspond to sum-frequency generation (SFG) and difference-frequency generation (DFG), respectively. The final term is known as optical rectification (OR). The complex conjugates (c.c.) in the above equation are not considered, as they do not contribute any additional processes beyond those already mentioned.

Fig. 2.4 illustrates the frequency conversion process in case of SFG. Two photons with frequencies ω_1 and ω_2 traverse the nonlinear medium, and produce frequency ω_3. The energy of the photons involved in the nonlinear interaction is conserved. Similarly for DFG, their energies are subtracted. Thus, the processes SHG or DFG lead to the emission of a photon with energy $\omega_3 = \omega_1 \pm \omega_2$. In second-harmonic generation (SHG), two photons with the same frequency ω combine, resulting in a photon with double the energy, given by $\omega_3 = 2\omega$.

2.7.1 Coupled wave equations

The previous discussion highlights how electromagnetic waves at specific frequencies can stimulate responses at other frequencies when propagating through a nonlinear

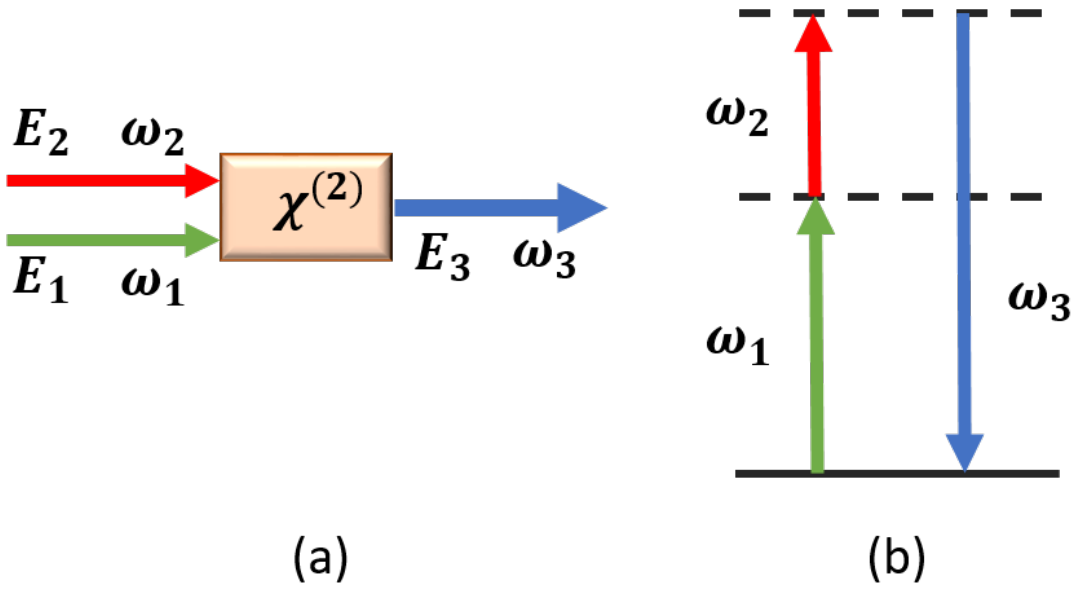

Figure 2.4: SFG process in a $\chi^{(2)}$ material, showing (a) two different field generating a third field, and (b) schematic transition of photons in virtual energy levels

medium. To delve deeper into how new frequencies are generated and how energy is exchanged between the interacting waves, we must examine Maxwell's equations in such media.

In a nonlinear, non-magnetic dielectric medium devoid of currents and free charges, Maxwell's equations simplify into the wave equation, now modified by a nonlinear source term as follows [57],

$$\nabla^2 E = \mu_0 \varepsilon_0 \frac{\partial^2 E}{\partial t^2} + \mu_0 \frac{\partial^2 P_{\mathrm{NL}}}{\partial t^2}$$

Here, μ_0 represents the permeability of free space. Generally, this equation is not solvable analytically, but by applying certain approximations, we can derive a form more suitable for computation. Suppose the electric field E and the polarization P

propagate along the z-axis. They can be expressed as,

$$E(z,t) = \frac{1}{2}\left[E(z,\omega)e^{-i(kz-\omega t)}\right] + \text{c.c.}$$

$$P(z,t) = \frac{1}{2}\left[P(z,\omega)e^{-i(kz-\omega t)}\right] + \text{c.c.}$$

In these equations, ω is the frequency, and k is the wave number, which can be described as,

$$k = \frac{n(\omega)\omega}{c} \tag{2.9}$$

The refractive index $n(\omega)$ at frequency ω is expressed as,

$$n(\omega) = \sqrt{\frac{\varepsilon(\omega)}{\varepsilon_0}}$$

where $\varepsilon(\omega)$ is the medium's permittivity at frequency ω, and ε_0 is the vacuum permittivity. The parameter c stands for the speed of light in a vacuum.

For both linear and nonlinear interactions where the fields' amplitudes vary slowly relative to the wavelength in space and the optical period in time, the Slowly Varying Envelope Approximation (SVEA) is applied [57]. This reduces the second-order wave equation to a first-order equation along the propagation direction,

$$\frac{\partial E(\omega)}{\partial z} = \frac{i\mu_0 c^2}{2n} P_{\text{NL}}(\omega)$$

For second-order nonlinear processes, where the fields mix, utilizing relevant equa-

tions leads to the formulation of three coupled wave equations,

$$\frac{\partial E_1}{\partial z} = i\frac{\omega_1}{2k_1 c} K d_{\text{eff}} E_3 E_2^* e^{i\Delta k z}$$

$$\frac{\partial E_2}{\partial z} = i\frac{\omega_2}{2k_2 c} K d_{\text{eff}} E_3 E_1^* e^{i\Delta k z}$$

$$\frac{\partial E_3}{\partial z} = i\frac{\omega_3}{2k_3 c} K d_{\text{eff}} E_1 E_2 e^{-i\Delta k z}$$

Here, K is the degeneracy factor, d_{eff} represents the effective nonlinearity, and $\Delta k = k_3 - k_2 - k_1$ is the phase mismatch between the interacting waves. These interactions comply with the frequency relation $\omega_3 = \omega_1 + \omega_2$. Efficient energy transfer occurs when $\Delta k = 0$, as discussed in the next section.

For second-harmonic generation (SHG), where $\omega_1 = \omega_2 = \omega$ and $\omega_3 = 2\omega$, only two waves are involved. The SHG coupled-wave equations are,

$$\frac{\partial E_{2\omega}}{\partial z} = i\frac{2\omega^2}{n_{2\omega} c} K d_{\text{eff}} E_\omega^2 e^{i\Delta k z}$$

$$\frac{\partial E_\omega}{\partial z} = i\frac{2\omega^2}{n_\omega c} K d_{\text{eff}} E_\omega^* E_{2\omega} e^{-i\Delta k z}$$

Here, $\Delta k = k_{2\omega} - 2k_\omega$ is the phase mismatch between the interacting waves, where k_ω and $k_{2\omega}$ are the wave vectors, and n_ω and $n_{2\omega}$ are the refractive indices for frequencies ω and 2ω, respectively. In the low-conversion regime (assuming negligible pump depletion), these equations simplify to a linear first-order equation, which can be solved analytically for plane waves. The resulting second-harmonic intensity is given by [57],

$$I_{2\omega}(L) = \frac{2\omega^2 d_{\text{eff}}^2 L^2 I_\omega^2}{\varepsilon_0 n_{2\omega} c^2 n_\omega} \text{sinc}^2\left(\frac{\Delta k L}{2}\right) \tag{2.10}$$

where L is the length of the nonlinear medium, I_ω is the pump intensity, and $n_\omega, n_{2\omega}$ are the refractive indices for the pump and second-harmonic frequencies. If pump depletion is considered, the SHG efficiency can be expressed as,

$$\eta_{\text{SHG}} = \tanh^2(\eta_{o,\text{SHG}})$$

where $\eta_{o,\text{SHG}}$ is the efficiency assuming no pump depletion, derived from,

$$\eta_{o,\text{SHG}} = \frac{2\omega^2 d_{\text{eff}}^2 L^2 I_\omega}{\varepsilon_0 n_{2\omega} n_\omega^2 c^3} \text{sinc}^2\left(\frac{\Delta kL}{2}\right) \tag{2.11}$$

2.8 Phase matching conditions

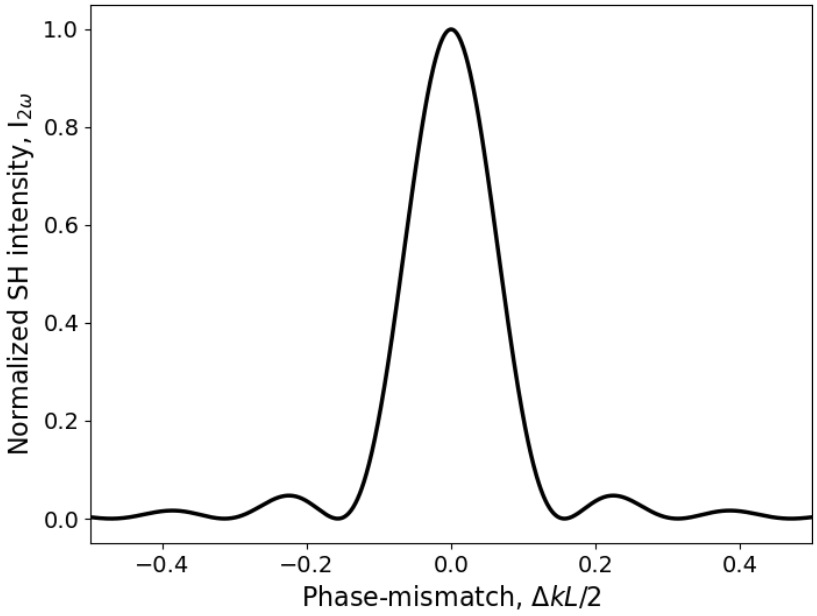

Figure 2.5: Variation of output SH intensity as a function of the phase mismatch, $\Delta kL/2$, demonstrating the sinc^2 dependence as given by Eq. 2.10

The Eq. 2.10 demonstrates that the intensity of second-harmonic generation (SHG),

$I_{2\omega}$, reaches its maximum when the phase mismatch, Δk, equals to zero. In other words, the condition of perfect phase-matching is required for optimal SHG efficiency. This relationship can be visualized in Fig. 2.5, which depicts the intensity of SHG as a function of the total phase mismatch $\Delta kL/2$. The sinc-squared profile illustrates how critical the phase-matching condition ($\Delta k = 0$) is for maximizing the SHG efficiency. Fig. 2.5 also highlights the dependence of SHG output on phase mismatch, showing that the closer the interaction is to perfect phase-matching ($\Delta k = 0$), the higher the second-harmonic power will be, according to the sinc-squared function in Eq. 2.11.

The question naturally arises: what leads to phase mismatch in the first place? According to Eq. 2.9, the wave vector k is proportional to the refractive index. Because a material's refractive index changes with wavelength (due to dispersion), different wavelengths propagate at different phase velocities in a medium, leading to phase mismatch between interacting waves.

If the waves do not meet the phase-matching condition, the SHG efficiency will vary along the length of the nonlinear crystal. This variation is caused by the oscillating relative phase between the driving nonlinear polarization and the newly generated wave, periodically reversing the flow of power. The critical length, known as the coherence length $L_c = \pi/\Delta k$, defines the distance over which the driving polarization and generated waves remain in phase, allowing power to transfer to the generated waves. However, beyond this coherence length, the waves fall out of phase, causing the energy to return to the driving wave. In the phase-matched scenario, the newly generated second harmonic radiation remains in phase with the earlier generated waves, leading to constructive interference and continuous energy transfer along the crystal. Achieving this phase-matching condition ensures efficient SH generation across the crystal length.

To attain phase-matching, two principal techniques are widely used: Birefringent Phase-Matching (BPM) and Quasi-Phase-Matching (QPM), which will be explored in the following sections.

2.8.1 Birefringent phase matching (BPM)

Birefringent phase-matching leverages the birefringence of an anisotropic nonlinear crystal, wherein the refractive index depends on the polarization of the electric field. The basic idea behind BPM is to polarize the interacting waves at different frequencies such that their phase velocities can be fine-tuned via the appropriate propagation direction within the crystal. In this way, the wave vectors satisfy the phase-matching conditions. Nonlinear crystals can be categorized based on the number of optical axes

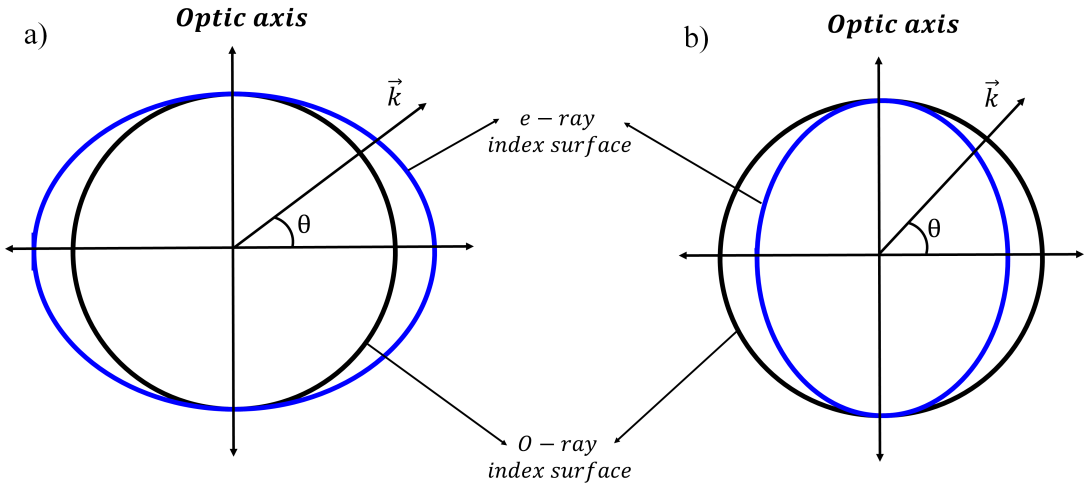

Figure 2.6: Index ellipsoids for (a) positive and (b) negative uniaxial crystals.

they possess, uniaxial crystals (with one optic axis) and biaxial crystals (with two optic axes). For simplicity, we will focus on uniaxial crystals to explain BPM. In a uniaxial crystal, birefringence can be described by two refractive indices: the ordinary index

(n_o) and the extraordinary index (n_e). The electric field that is polarized perpendicular to the optical axis always senses the ordinary refractive index, and is known as the ordinary beam. In contrast, the extraordinary beam, which is polarized orthogonally to the ordinary beam and lies in the plane containing the optical axis, experiences a refractive index $n_e(\theta)$ that depends on the angle between the optical axis and the propagation direction, θ as:

$$\frac{1}{|n_e(\theta)|^2} = \frac{\cos^2(\theta)}{n_o^2} + \frac{\sin^2(\theta)}{n_e^2}$$

Fig. 2.6 illustrates the birefringence of uniaxial crystals. In positive uniaxial crystals, the extraordinary index increases with angle, while in negative uniaxial crystals, it decreases. For both types, the extraordinary index can be fine-tuned by adjusting the angle θ of propagation relative to the optical axis.

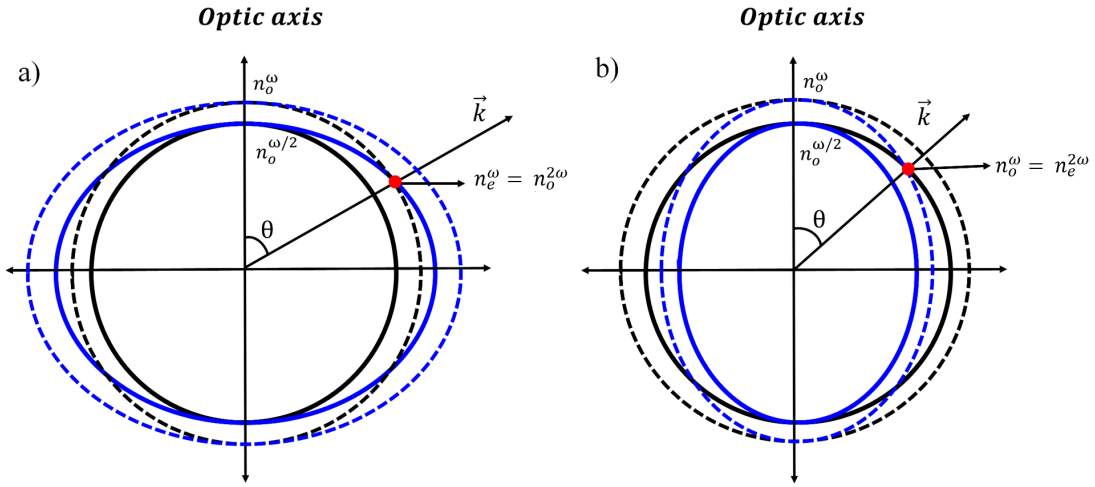

Figure 2.7: A demonstration of the BPM for (a) positive and (b) negative uniaxial crystals.

Fig. 2.7 shows how, at a particular angle θ, the extraordinary refractive index for the fundamental wave matches the ordinary refractive index for the second harmonic,

achieving perfect phase-matching in positive and negative uniaxial crystals.

In BPM, there are two configurations: type-I, where the interacting waves have the same polarization and the generated wave is polarized orthogonally; and type-II, where the interacting waves are orthogonally polarized.

Phase-matching that occurs when the propagation direction is perpendicular ($\theta = 90^{\circ}$) to the optical axis is known as noncritical phase-matching, whereas phase-matching for any other angle is called critical phase-matching. The term "critical" reflects the sensitivity of the process to beam misalignment, as phase-matching only works within a narrow range of beam angles.

2.8.2 Quasi phase matching (QPM)

Quasi-phase-matching (QPM) is an alternative technique to birefringent phase matching (BPM) used to compensate for phase mismatch in nonlinear optical processes, such as second harmonic generation (SHG). In nonlinear crystals, chromatic dispersion causes waves of different frequencies to propagate with different phase velocities, leading to phase mismatch. In BPM, birefringence is used to match these phase velocities. However, in materials where birefringence is low or where BPM is not feasible, QPM offers a solution.

In QPM, the phase mismatch is not perfectly eliminated. Instead, the interacting waves are allowed to experience some phase slip. As the waves propagate through the crystal, the phase difference between them gradually increases until it reaches a value of π, at which point the power flow begins to reverse. To prevent this reversal, QPM introduces a periodic correction to the phase. Specifically, every time the phase difference reaches π (after one coherence length, L_c), the sign of the nonlinear coefficient of

the material is reversed, effectively adding an additional phase shift of π. This brings the interacting waves back into phase and allows the power transfer to continue in a monotonic fashion, building up over the length of the crystal.

This periodic modulation of the nonlinear coefficient is achieved by periodically changing the sign of the coefficient with a period twice the coherence length ($\Lambda = 2L_c$) as shown in the Fig. 2.8. As a result, the generated output power increases in a stepwise manner rather than continuously, as it would in perfect phase matching. Although the power build-up is slower than in BPM, QPM offers other advantages, including access to higher nonlinear coefficients. One of the key benefits of QPM is

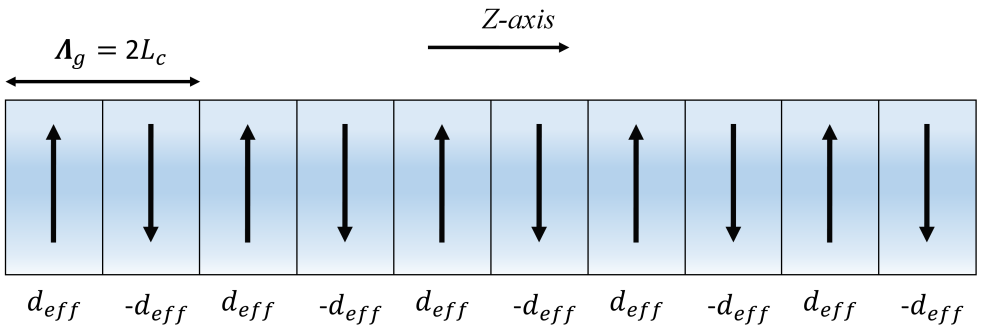

Figure 2.8: An illustration of a periodically poled nonlinear crystal to satisfy QPM

that it allows the same polarization direction for all interacting waves. In contrast to BPM, which requires different polarizations for different interacting waves, QPM can access the highest nonlinear tensor coefficients, often resulting in higher conversion efficiency. Moreover, QPM can be used in materials with low birefringence where BPM is not possible, and it can provide noncritical phase matching for a wide range of wavelengths, making it more versatile.

In terms of implementation, QPM is typically achieved by fabricating crystals with periodic structures, such as periodically poled ferroelectric materials like lithium nio-

bate (LiNbO3) or potassium titanyl phosphate (KTP). These materials have spontaneous electronic polarization, and by applying a strong electric field periodically, the polarization can be inverted. This inversion results in the periodic sign change of the nonlinear susceptibility tensor, creating a grating with a period that corresponds to the coherence length of the desired nonlinear process.

Although QPM is highly effective, there are some challenges and limitations.Achieving high-quality periodic poling is especially challenging for thick samples. Additionally, the number of materials available for QPM is limited, and the range of wavelengths that can be phase-matched in these materials is constrained.

In chapter 4 we used BiBO crystal as our nonlinear medium, which is birefringent-phase matched, type-I crystal. For sensing periodicity in chapter 5, and sensing aberration in chapter 6), we used periodically poled cystals as a grating object.

Chapter 3

Generation of Tunable Talbot Range

3.1 Introduction

As discussed in section 1.3, Talbot effect has proven to be a versatile phenomenon with applications ranging from spectrometry and metrology to advanced imaging techniques. Its ability to enhance our understanding of wave propagation and diffraction, combined with its practical applications in measuring and analyzing microstructures, underscores its importance in both fundamental and applied sciences.

One of the critical components to understand while working with the Talbot effect-based interferometry, lithography, or metrology is to resolve the desired Talbot planes accordingly. To instantiate, the Talbot length is given by [22]

$$Z_T = \frac{\lambda}{1 - \sqrt{\left(1 - \frac{\lambda^2}{\Lambda^2}\right)}} \approx \frac{2\Lambda^2}{\lambda}. \tag{3.1}$$

Here, Λ is the grating period, and λ is the wavelength of the incident radiation. From the Eq. 3.1, it is evident that the Talbot length is completely dependent on the grating period (Λ) and the wavelength of the incident light (λ). Hence, given the stringent dependence on the grating period and wavelength, it is quite complex to shift the integer and fractional Talbot planes at any other distance. The following section proposes and demonstrates a scheme to overcome these stringent conditions and produce tunable Talbot length.

3.2 Theory and experimental scheme

The concept of the tunable Talbot length is pictorially represented in Fig. 3.1. A lens, L_a, of focal length, f_a, is used to Fourier transform [10] a periodic object placed after the lens at a distance d from its back focal plane (Fourier plane). Subsequently, the second lens, L_b, of focal length, f_b, is used for inverse Fourier transformation resulting in the image of the periodic object at the image plane. In such a configuration, one can observe the Talbot effect at two regions, right after the periodic object and after the image plane named as Talbot range and modified Talbot range, respectively. According to Fourier transform theory [10], adjusting the position (distance, d) of the periodic object from the back focal plane of the lens, L_a, we can control the distribution of the spatial frequency of the object at the Fourier plane of lens L_a occurring due to the variation in the illuminated region of the object. In fact, it has been observed [75] that any periodic object results in an array of spots at the Fourier plane, and the spatial distribution of the array depends on the position of the periodic object away from the back focal plane of the lens. Each spot of the array has an intensity profile same as the input beam (here, Gaussian beam). The modified pitch of the Gaussian beam array at the Fourier plane of the lens, L_a, due to the period object of pitch Λ placed at a distance

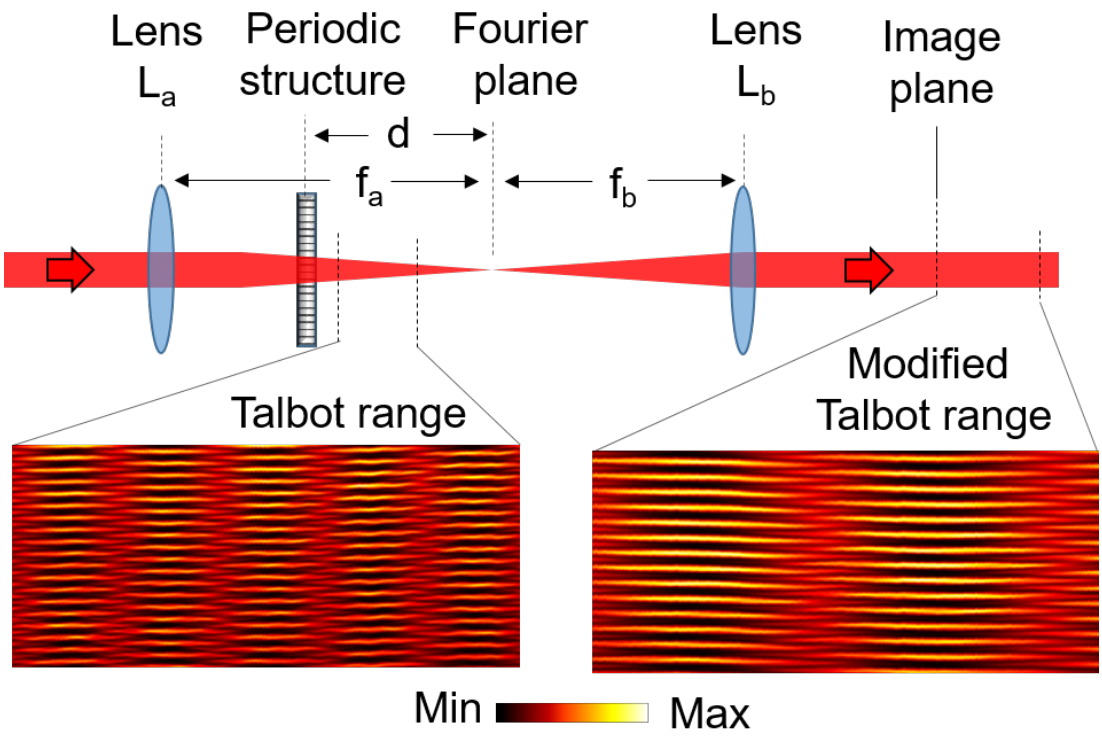

Figure 3.1: Schematic of the experimental setup to produce tunable Talbot length. f_a and f_b are the corresponding focal lengths of the lenses L_a and L_b. Inset intensity profiles show tunability of Talbot length by tuning the control parameter, d.

d from the back focal plane can be represented as [76],

$$\Lambda' = \frac{\lambda d}{\Lambda}. \tag{3.2}$$

Here, λ is the wavelength of the beam illuminating the object. The inverse Fourier transform of the Gaussian beam array using the lens L_b results in the image of the periodic object at the image plane with effective pitch or period as

$$\Lambda_{eff} = \frac{f_b \lambda}{\Lambda'} = \frac{f_b}{d}\Lambda. \tag{3.3}$$

As a result, the Talbot length, $Z_T = 2\Lambda^2/\lambda$, of the object of the period, Λ, measured right after the object (see the left inset Talbot range of Fig. 3.1) will be modified for the

measured Talbot length after the image plane (see the right side inset Modified Talbot range of Fig. 3.1). Using Eq. 3.2 and 3.3 we can find the modified Talbot length as,

$$Z_T^M = \frac{2\Lambda_{eff}^2}{\lambda} = \left(\frac{f_b}{d}\right)^2 \left(\frac{2\Lambda^2}{\lambda}\right) = \left(\frac{f_b}{d}\right)^2 Z_T. \tag{3.4}$$

It is evident from Eq. 3.4, that the Talbot length, z_T^M is modulated by a factor of $(f_b/d)^2$, square of the ratio of the focal length of the inverse Fourier transforming lens, L_b, and the position of the periodic object away from the back focal plane of the Fourier transforming lens, L_a. Therefore, for a given set of lenses, periodicity of the object and wavelength, tunable Talbot length can be accessed by simply varying the position of the object (i.e., the value of d).

To get the tunable Talbot length, we used a He-Ne laser of wavelength 632.8 nm and two lenses, L_a and L_b of same focal length, $f_a = f_b = 200$ mm. We used a one dimensional ronchi grating of period 25 μm (a part of Thorlabs R1S1L1N Negative Test Target) and placed it on a translation stage, d distance behind the focal plane of lens L_a, as shown in the Fig. 3.1. We used the translation stage to change the control parameter (d value), and consequently generated desired Talbot length (Z_T^M). At the image plane of the lens L_b, we placed the CCD (charge-coupled device) camera on another translation stage along the beam propagation to record the Talbot planes. We recorded the Talbot lengths for three different values of control parameter, d = 40 mm, 70 mm and 100 mm. We also measured the Talbot length in case of $4f$ imaging, i.e. placing the grating at the back focal plane of the lens L_a and the CCD camera at the focal plane (image plane for $4f$ imaging) of the lens L_b. To generate the Talbot carpet, we plotted the line profiles of the CCD images along propagation distance, by extracting the intensity profile of each of the CCD images from a fixed pixel line (here, pixels in the horizontal line) of width 6.45 μm and concatenating the pixel lines

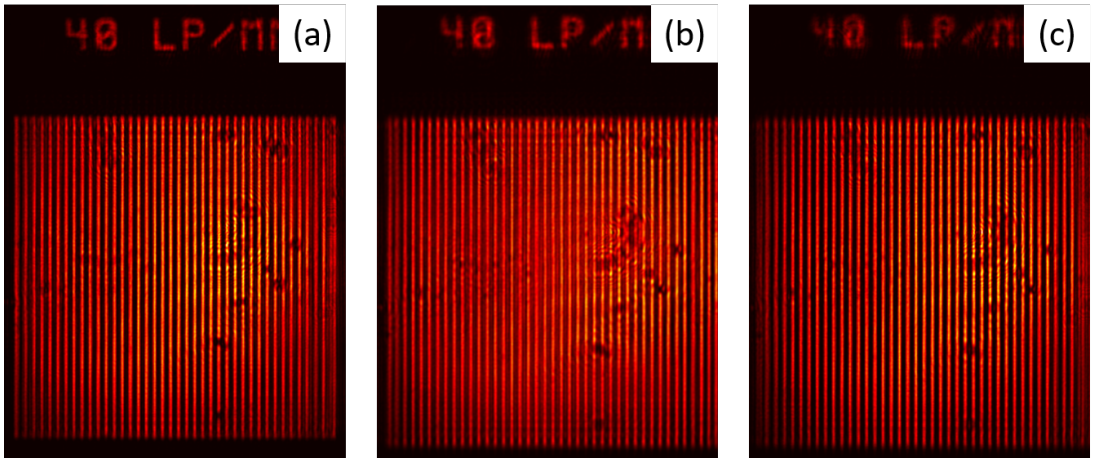

Figure 3.2: Three different transverse Talbot planes for the control parameter, d = 70 mm. (a), (b) and (c) shows the planes of z = 0, 0.25 Z_T and 0.5 Z_T respectively

to form a continuous image. We recorded the Talbot images up to a range of 50 mm with an interval of 0.1 mm for the four cases mentioned above.

3.3 Experimental results

The transverse planes of the image plane ($z = 0$), 0.25 Z_T and 0.5 Z_T are shown in the Fig. 3.2 for the control parameter, d = 70 mm. The disappearance and reappearance of the sharp grating lines are clearly visible here. According to our modified Talbot length (z_T) as suggested in Eq. 3.3, we should be able to surpass the stringent condition of grating periodicity (Λ) and wavelength (λ) now. With a grating of periodicity 25 μm, we get a Talbot length, $z_T = 1.97$ mm and confirm it with $4f$ imaging. Although the Talbot range can be varied continuously using our control parameter d, we recorded the Talbot range for three different values of d to demonstrate long range tunability. The Talbot ranges for these three d values are compared with Talbot range for $4f$ imaging, as shown in the Fig. 3.3. Due to the continuously variable control parameter, d, for a discrete set of grating period (Λ) and wavelength (λ), a continuous set of Talbot lengths were created. This experimental scheme produces long range

tunable Talbot length, strongly supported with theory of Fourier transform to predict the tunable Talbot length.

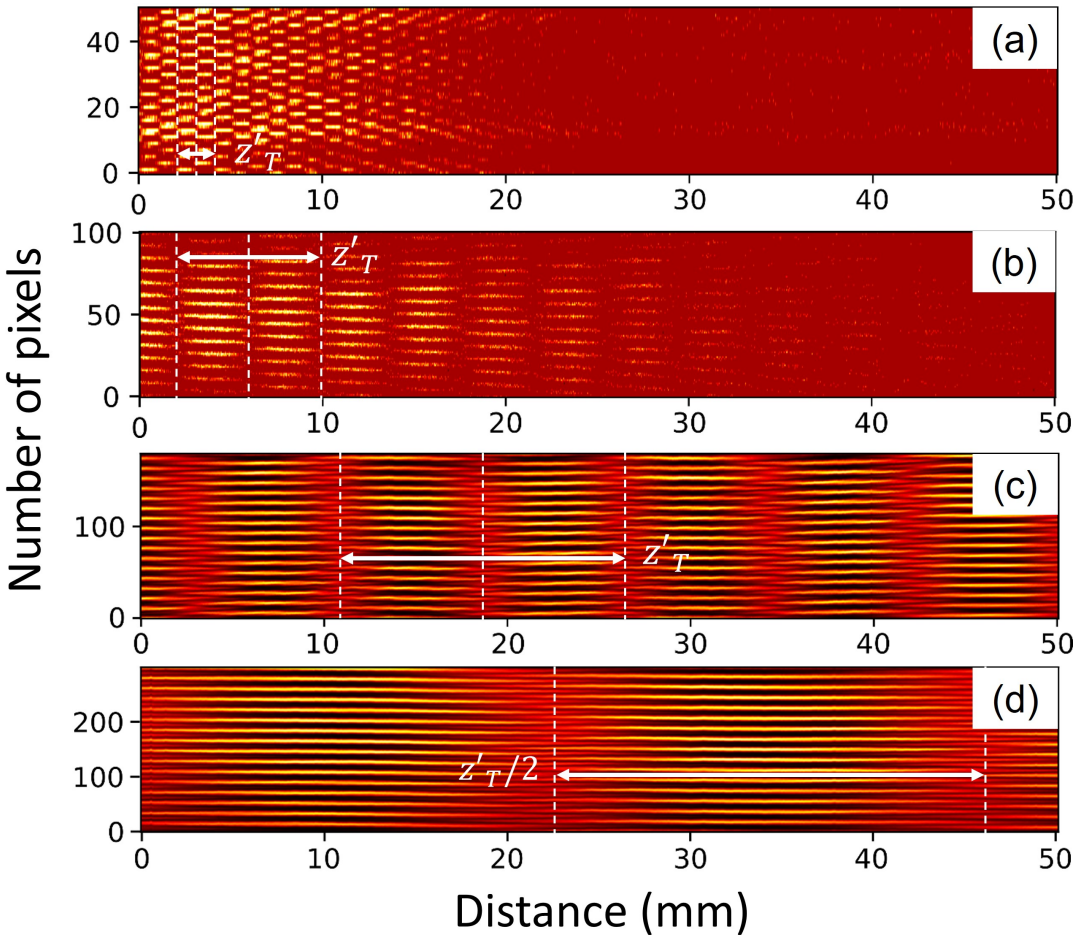

Figure 3.3: Tunable Talbot range for different values of the control parameter, d. (a), (b), (c) and (d) represents 4f imaging, d = 100 mm, d = 70 mm, and d = 40 mm respectively

Fig. 3.3 clearly shows that the Fresnel diffraction region, where the Talbot images are formed, is varying enormously with the control parameter, d. For $4f$ imaging the region is very small and as we decrease the d value, the region expands in the propagation direction, indicating higher longitudinal magnification of the Talbot range. We measured the Talbot lengths to be 1.975 mm, 7.93 mm, 15.83 mm and 49 mm corresponding to 4f imaging, $d = 100$ mm, $d = 70$ mm and $d = 40$ mm respectively.

Conclusively, changing the control parameter, we generated tunable Talbot length over a range of 1.97 mm (for $4f$ imaging) to 49 mm (for $d = 40$ mm) i.e. 25 times greater than the actual Talbot length, using a 25 μm grating period. In principle, we can continue to decrease d value and produce longer Talbot lengths, as suggested by the Eq. 3.4 ($Z_T^M \propto 1/d^2$). But, as we approach the focus of the lens L_a, the Gaussian beam spot decreases significantly and can not illuminate enough number of grating period to get a long range Talbot effect.

3.4 Discussion on limiting the control parameter

As mentioned in the above section, generation of longer Talbot length needs smaller values of the control parameter, d. For a smaller d value, the number of grating periods illuminated by the incident light decrease gradually. Since, the necessary condition to generate Talbot effect is periodicity and we proclaim an object periodic when the length of the periodic object is much larger than the length of a single period, naturally a question arises, how many slits are required to observe Talbot effect.

With a 100 μm grating period and the same 632.8 nm wavelength laser, we simulated and experimentally observed near field diffraction for different numbers of slits illuminated by the laser, required to produce Talbot effect. Two particular cases of three slits and five slits are shown in the Fig. 3.4. These simulations were done using a python module [77]. It is evident from the Fig. 3.4(a,b) that for illuminating three slits Talbot carpet does not arise; merely a fractal has appeared in propagation direction. In case of Fig. 3.4(c,d) that is for five slits, at least one Talbot length has appeared for both simulation and experimental results.

Based on the above study, we can conclude that at least five slits must be illuminated for the Talbot effect to manifest. In our setup, with focal lengths of $f_a = f_b = 200$

mm, we constrained our control parameter to $d = 40$ mm, allowing us to cover a minimum of 15 slits in the experiment in order to observe a long-range Talbot carpet.

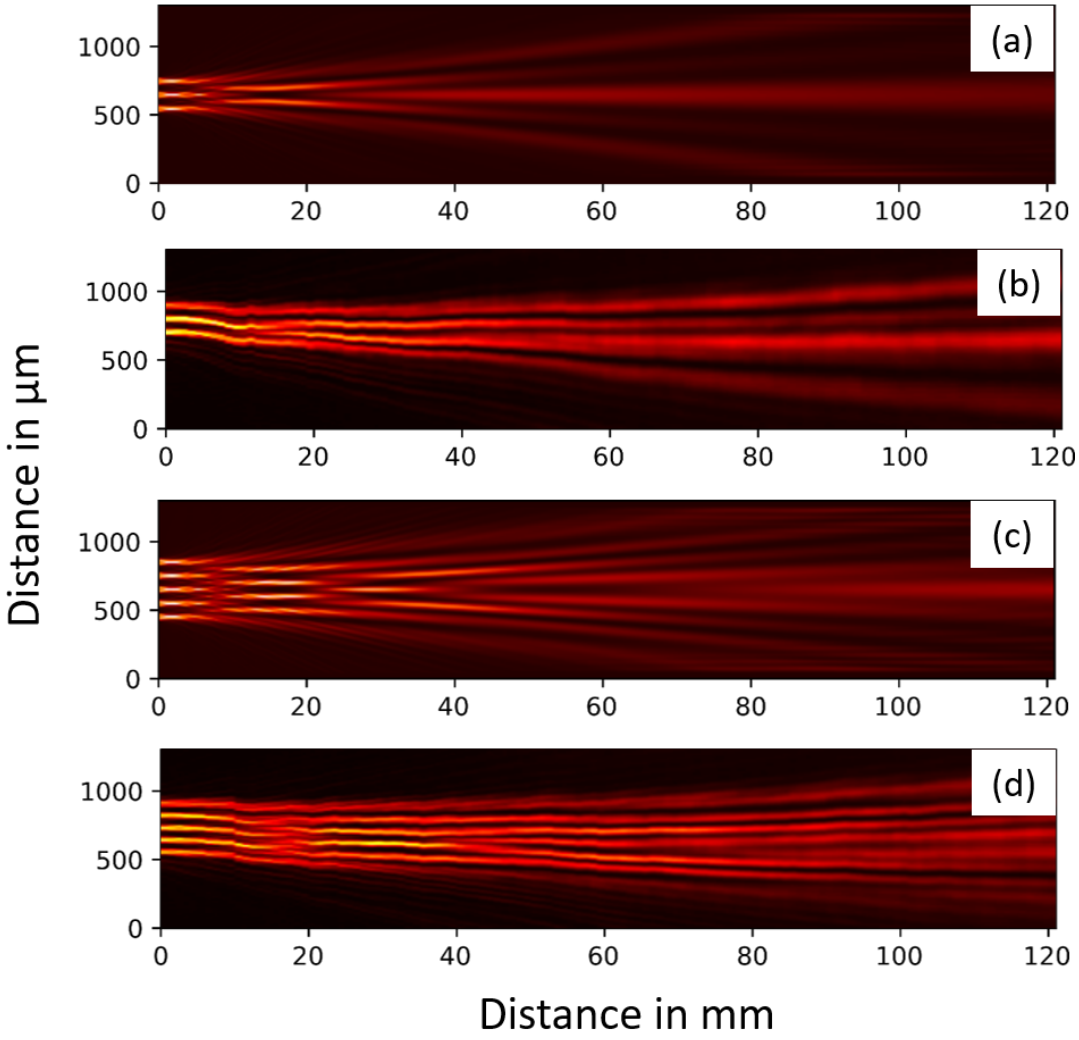

Figure 3.4: Near field diffraction for two different number of slits illuminated. (a) and (b) correspond to simulated and experimental images respectively, illuminating three slits; (c) and (d) correspond to simulated and experimental images respectively, illuminating five slits

3.5 Implications

The experimental demonstration of the tunable Talbot range through control of the variable parameter d offers a significant advancement by enabling continuous tuning of

the Talbot length beyond the fixed constraints of grating period and wavelength. This method, verified by Fourier theory, opens up new possibilities for dynamic control in imaging, sensing, and lithography applications, where variable Talbot lengths would play a crucial role. We will see two specific applications of this architecture in chapters 4 and 5 of the thesis.

3.6 Conclusion

With the help of a suitable theoretical frame work, we have developed a generic experimental scheme based on Fourier transform technique, to independently control the Talbot lengths of any periodic structure in a continuous manner, overcoming the stringent dependence on grating period and wavelength on the self-images. With a grating of period 25 μm, we have produced tunable Talbot lengths of a wide range from 1.97 mm to 49 mm, hence, realizing a range up to 25 times greater than the original range. This generic technique can be useful in application areas such as Talbot lithography, Talbot-lau interferometry and various other applications of metrology. In the next two chapters we will extend this technique for nonlinear frequency upconversion of Talbot effect with tunable Talbot length, and sensing variation in periodicity of smaller grating periods.

Chapter 4

Nonlinear Upconversion of Talbot Effect with Flexible Talbot Lengths

4.1 Introduction

Microlens arrays (MLAs), a 2D array of close-packed lenslets, are optical elements designed to split the wavefront into multiple beamlets of equal energies. MLAs have found a great deal of attention for their wide range of applications in wavefront sensing [78], digital holography [79], and also as a tool for fundamental studies in supercontinuum generation [80]. Having a series of periodic lenslets, they are also being used as array illuminators and in ultrafast laser filamentation experiments [81]. In 1836, H. F. Talbot observed a unique self-imaging effect while working on periodic structures [9]. When a plane wave is incident on a periodic grating, the image of the grating field is replicated at fixed positions in the propagation direction, known as the Talbot planes appearing at the distances, $z = N\Lambda^2/\lambda$. Here, Λ is the period of the grating object, λ is the wavelength of the input radiation, and N is a positive inte-

ger. For odd values of N, the Talbot images are shifted laterally by an amount of $\Lambda/2$ with respect to the grating position. Therefore, the distance between two consecutive non-shifted image planes is $z_T = 2\Lambda^2/\lambda$, referred to as Talbot length [22]. The Talbot effect, being a near-field effect, is observed as a consequence of the diffraction of the input field from the periodic object and the subsequent interference between the diffracted fields. Near-field diffraction is enriched with several important properties. For example, if one explores the strong imaging regime [32], where frequencies are higher than $1/\lambda$, superoscillation of the state can be used for subwavelength imaging with grating waves, can access certain advantages over imaging with evanescent waves [82]. Imaging exploiting the superoscillation has been demonstrated a few years ago [83]. The Talbot effects have been observed in varies research areas. For example, in atomic physics, the manipulation of Talbot phenomena in cold atomic systems represents a promising frontier in optical imaging and manipulation at the quantum level [84]. As such, efforts have been made with theoretical and experimental studies of first- and second-order Talbot effects using electromagnetically induced grating [68], and the spontaneous parametric four-wave mixing by modulating the third order nonlinear optical coefficient [85] through a strong standing wave in cold atomic medium and molecules. Nonlinear Talbot effect has been observed in rouge waves to explore the relation between intensity of breathers and transverse period, and Talbot length [86]. Talbot effect has been used in experimental demonstration of increased accuracy in modulation instability gain in nonlinear beams [87]. Researchers have also explored surface gravity water wave packets in linear and nonlinear regimes producing Talbot carpets and Akhmediev breather waves respectively, by simply varying steepness of the waves [88]. Additionally, the experimental observations on dynamic behaviors of wave packets in non-Hermitian photonic graphene 2D honeycomb optical lattice structures realized in three-level Λ-type atomic vapor configurations [89] shows the

possibility of the development of all-optical-controllable Talbot–Lau interferometers, and also improvement in the performance of cold atom imaging and lithography.

On the other hand, MLAs, being 2D periodic objects, are also expected to produce self-imaging effects. It has been verified that MLAs also exhibit the Talbot effect with almost similar properties [90, 91], however, the additional phases in the case of lenslets that are not closely packed resulted in quasi-Talbot effects. This self-imaging property of MLAs has been found useful in a variety of applications in science and technology. Employing the Talbot effect in X-ray Talbot interferometers, the phase structures of 3D samples can be identified from the Moiré fringe patterns [92]. Similarly, using fractional Talbot images, high-resolution fluorescence images are obtained in fluorescence Talbot microscopy [93]. Although Talbot imaging with MLAs has been studied in the past, no significant efforts have been made on single-pass image upconversion of periodic objects through the second harmonic generation (SHG) and retaining Talbot effect [84] in the new wavelength where the high-efficiency image sensors are abundant. In 2010, the SH Talbot effect was observed for the first time in periodically poled lithium tantalate (PPLT) crystals commonly used for highly efficient nonlinear frequency conversion processes. However, in this case, the poling periodicity of the crystal was used as the periodic structure for the study of the Talbot effect [58] by illuminating the crystal in the direction orthogonal to the poling direction. As a result, the direct benefit of periodic poling of the nonlinear crystal after accessing the highest nonlinear gain and long crystal length was unexplored, resulting in low nonlinear frequency conversion efficiency. Recently, SHG of Talbot images with pump beam modified by spatial light modulator (SLM) has been reported [60]. Again, the lower damage threshold of SLM has restricted such studies to lower power levels. As a result, the control over the Talbot planes in both pump and SHG with high nonlinear upconversion efficiency over long distances has not been addressed so far. Given that the Talbot length is propor-

tional to the square of the period of the object for a fixed wavelength [94], one can vary the Talbot length by using MLAs of different periods in different array architecture as observed [89] in case of atomic coherence gratings instantaneously tunable complex honeycomb potential in atomic and atomic-like ensemble. However, it is essential to access tunable Talbot length while keeping all physical parameters of the grating constant at fixed wavelength for high resolution imaging and lithographic application.

Here, we report, for the first time to our knowledge, high-power, single-pass frequency-upconversion of the periodic object producing Talbot planes with controllable lengths. Using the MLA as the 2D periodic object and 1.2 mm long BiBO crystal for frequency upconversion, we have demonstrated Talbot effect in both pump and upconversion wavelength with Talbot lengths tunable across $z_T = 26$ cm to $z_T = 62.4$ cm at the pump and $z_T = 12.4$ cm to $z_T = 30.8$ cm at the green wavelength.

4.2 Experimental configuration

The schematic of the experimental setup is shown in Fig. 4.1. A 5 W Yb-fiber laser with a spectral bandwidth of 15 nm centered at 1064 nm providing femtosecond pulses of ~ 260 fs duration at a repetition rate of 78 MHz is used as the pump radiation [95]. The input power to the setup is varied using a half-wave plate $(\lambda/2)$ and a polarizing beam-splitter (PBS) cube. The input beam is expanded and collimated using a telescopic lens combination comprising two lenses, L1 and L2, of focal length, $f_1 = 50$ mm, and $f_2 = 100$ mm, respectively, to collimate the laser beam into a near plane wavefront. The second $\lambda/2$ plate is used to control the polarization of the laser beam depending upon the orientation of the nonlinear crystal for optimum phase-matching in the experiment. A lens, L3, of focal length, $f_3 = 150$ mm, is used to Fourier transform the phase profile of the microlens array (MLA) (Thorlabs MLA 300-14AR) placed at a

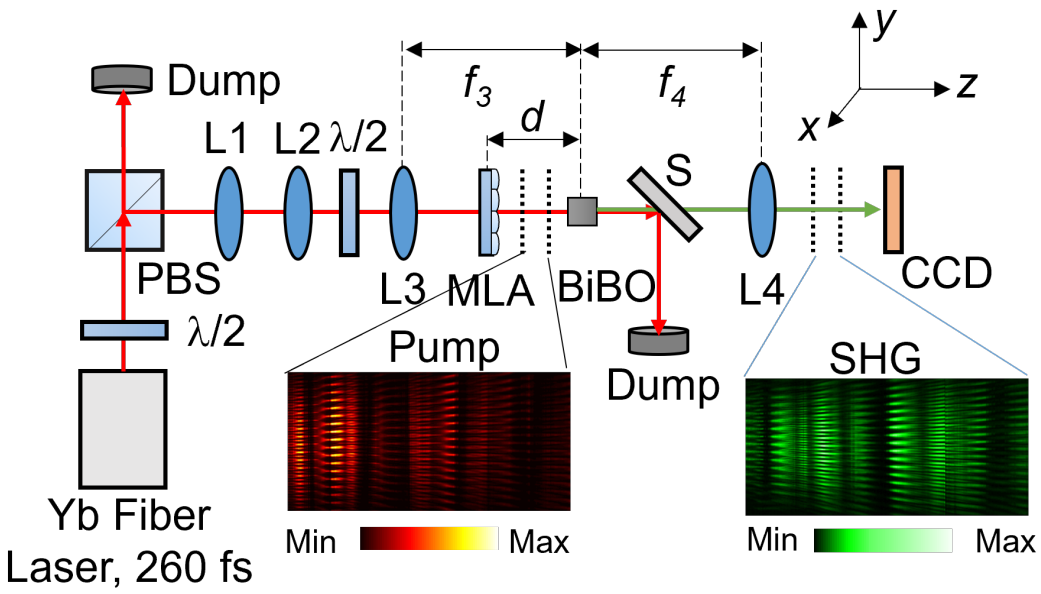

Figure 4.1: Schematic of the experimental setup to study the nonlinear interaction of the Talbot effect. $\lambda/2$, half-wave plate; PBS, polarizing beam splitter cube; L1-4, plano-convex lenses; MLA, microlens array; BiBO, nonlinear crystal; S, wavelength separator. (Inset) Images of light carpet at pump and upconversion wavelength.

distance, d, from the back focal plane of the lens. The MLA consisting of 391 lenslets of focal length, $f_{MLA} = 18.6$ mm, with a lenslet period of $\Lambda = 300$ μm [75], is used as the periodic object to generate the Talbot images. A 1.2-mm-long bismuth triborate (BiBO) crystal [96] with an aperture of 4×8 mm^2 is placed at the back focal plane of the lens, L3. The crystal is cut for type-I ($e + e \rightarrow o$) frequency-doubling in the optical yz-plane ($\Phi = 90^o$) with an internal angle of $\theta = 168.5^o$ to the normal incidence and is used for second harmonic generation (SHG) of the Talbot images at 1064 nm into the green at 532 nm. The frequency-doubled green beam is extracted from the undepleted pump using a wavelength separator, S, and subsequently imaged using a CCD camera after the lens, L4, of focal length, $f_4 = 150$ mm. The lens, L4, is placed at a distance, f_4, from the crystal to inverse Fourier transform the array of the spatial structure of the input beam (here Gaussian beam) generated due to the Fourier transform of the MLA

at the back focal plane of the lens, L3. To record the Talbot images of both pump and SHG beams along the propagation distance, the CCD camera is placed on a translation stage. The insets of Fig. 4.1 shows the line profiles of the self-images of both the pump and the SHG beams recorded along with propagation distance at an interval of 1 mm.

4.3 Results and discussion

To verify the Talbot effect of the MLA at the pump wavelength, we illuminated the MLA with the collimated pump beam by removing the lenses, L3 and L4, and recorded the images right after the MLA at an interval of 1 mm along the propagation direction. The results are shown in Fig. 4.2. To avoid the mechanical constraint of the experiment, the images were recorded starting from at a distance of about ~ 5 cm from the MLA, up to a distance of 45 cm, covering a range of 40 cm. However, such a delayed start of the image recording does not affect the overall experimental results, as the Talbot planes are replicated at every Talbot length irrespective of the initial position of occurrence. To improve the visibility and exact detection of the Talbot planes, we plot the line profiles of the CCD images along propagation distance by extracting the intensity profile of the CCD images from a fixed pixel line (here, pixels in the vertical line) of width 4.4 μm (corresponding to the size of a single pixel) and concatenate the line intensity images with propagation distance forming a continuous image (light carpet). The results are shown in Fig. 4.2(a). As evident from Fig. 4.2(a), the image locations identified with dashed white lines are almost identical, indicating the positions of Talbot planes of the pump beam. The intensity profiles, indicated by the first and third dashed lines, are almost identical, indicating the positions, z = 1 mm and 171 mm respectively. Therefore, the experimental Talbot length of the MLA with a pitch of Λ = 300 μm is z_{T_p} = 170 mm. As reported previously [97], the microlens

array can be approximated as a 2D sinusoidal phase grating. Therefore, the Talbot images recorded in the present study form a 3D light carpet comprising both self and fractional Talbot images and complicated fractal intensity distribution appearing as a function of distance across the image [62], confirming the successful generation of light carpet for MLA. For the lenslet pitch of $\lambda = 300\ \mu$m, the theoretical Talbot length for the pump wavelength of $\lambda_p = 1064$ nm can be calculated to be, $z_{T_p} = 2\Lambda_p^2 = 169.1$ mm, in close agreement to the experimental value, z_{T_p} = 170 mm.

To observe the upconversion of the Talbot effect, we placed the nonlinear crystal at the focal plane, $f_{MLA} = 18.6$ mm, of MLA, and recorded the intensity profile of the SHG beam along the propagation direction, with an increment of 1 mm, after extraction from the undepleted pump using the wavelength separator, S. However, due to the mechanical constraints in positioning the wavelength separator, the nearest attainable limit of the CCD camera position was about 15 mm from the crystal plane. Using the same technique of extracting the line profile of fixed pixel line from the CCD images along propagation and concatenating the images, we observed the variation of the SHG beam along propagation, with the result shown in Fig. 4.2(b).

As evident from Fig. 4.2(b), the images of the SHG beam are almost identical, as marked by the dashed lines along the propagation axis, indicating the positions of Talbot planes. However, from Fig. 4.2(a) and Fig. 4.2(b), it is evident that the SHG images are reproduced at a propagation distance twice that of the pump images. Theoretically, the Talbot length of the SHG beam, $z_{T_{SH}} = 2\Lambda^2/\lambda_{SH} = 2z_{T_p} = 338$ mm, is twice that the Talbot length of the pump beam, $z_{T_p} = 169.1$ mm, since $\lambda_{SH} = \lambda_p/2$. Using the results of Fig. 4.2(b), we measured the Talbot length of the single-pass frequency-doubled Talbot effect to be $z_{T_{SH}} = 330$ mm, close to the theoretically predicted value of $z_{T_{SH}} = 338$ mm. By carefully analyzing the line profiles, one can clearly

see the change in the spatial frequencies of the SHG beam in fractional Talbot planes along the propagation distance. The decrease in the intensities with propagation distance can be attributed to the divergence effect of the lenslets of MLA. It is evident

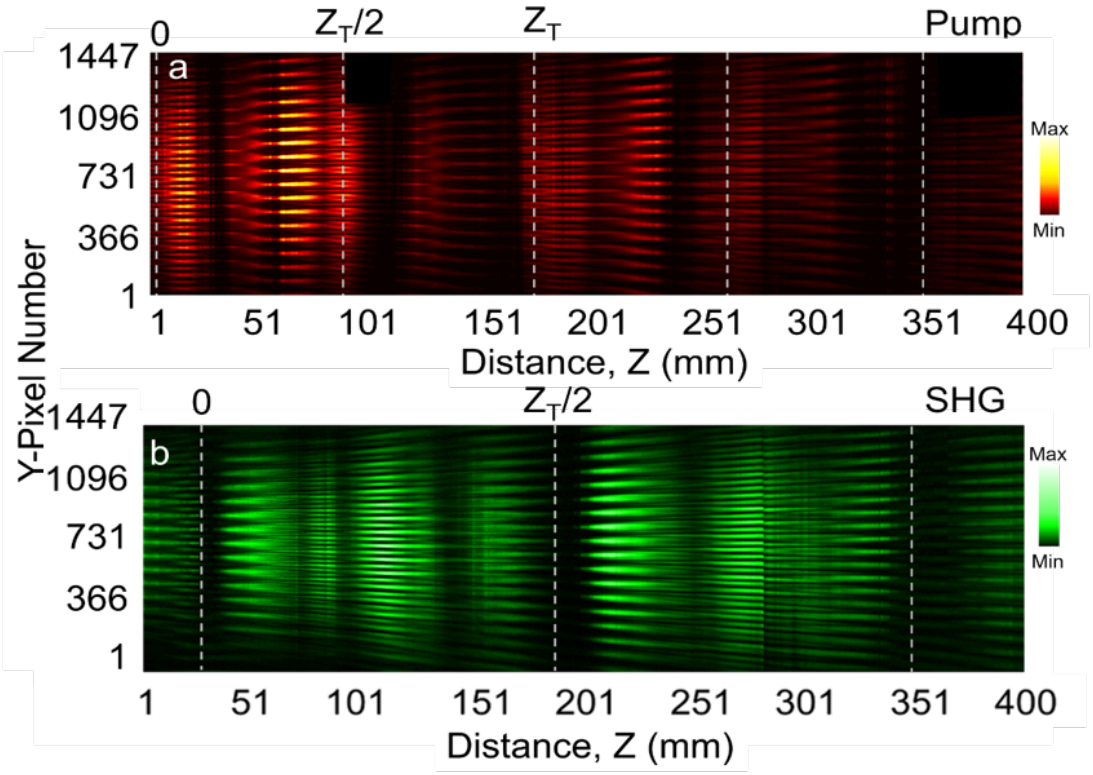

Figure 4.2: Light carpet along propagation distance for the periodic object (microlens array) at (a) pump, and corresponding (b) upconversion wavelengths confirming Talbot effect. The white dashed lines identify different Talbot planes.

from the experimental results of Fig. 4.2 that the Talbot lengths of the pump and the SHG beams strictly depend on the input parameters of the MLA. To overcome this stringent dependence and to obtain long-range self-images with tunable Talbot lengths, we controlled the scale of the Fourier transform of the MLA by placing it after the lens L3 at a distance d from the back focal plane of the lens. According to the Fourier transformation theory [10], adjusting the separation distance, $f_3 - d$, between the MLA and lens L3, we can control the scale of the Fourier transform at the focal plane of the lens L3 due to the change in the illuminated region of the MLA. As reported previously

[75], the Fourier transform of the MLA will produce the array of spots. Each spot of the array has an intensity profile same as the input beam (here Gaussian). The pitch of the Gaussian arrays can be represented as [76],

$$\Lambda' = \frac{\lambda_p d}{\Lambda} \tag{4.1}$$

Here, Λ is the pitch of the MLA. Now, the inverse Fourier transform of the Gaussian array using the lens L4, of focal length, f_4, placed at a distance, f_4, from the Fourier plane of the lens L3, produces scaled Talbot effect due to the scaling of the spatial distribution of the MLA. The effective lenslet period of the MLA at the back focal plane of the lens L4 can be written as,

$$\Lambda_{eff} = \frac{f_4 \lambda_p}{\Lambda'} = \frac{f_4}{d}\Lambda \tag{4.2}$$

Consequently, the modified Talbot length of the pump beam can be expressed as,

$$z_{T_p}^M = \frac{2\Lambda_{eff}^2}{\lambda_p} = 2(\frac{f_4}{d})^2 \frac{\Lambda^2}{\lambda_p} = (\frac{f_4}{d})^2 z_{T_p} \tag{4.3}$$

As evident from Eq. 4.3, the Talbot length, z_{T_p}, is modulated with a factor, $(f_4/d)^2$, the ratio of the focal length of the inverse Fourier transforming lens, L4, and the position of the MLA away from the back focal plane of the Fourier transforming lens, L3. Therefore, for a fixed focal length of the lens, L4, the Talbot length can be controlled by simply adjusting the position of the MLA. For the SH Talbot effect, the crystal is placed at the Fourier plane of lens L3, keeping the rest of the experimental setup fixed. Similar to Eq. 4.2, the effective lenslet period of the MLA in the SHG process, can be obtained as,

$$\Lambda_{eff} = \frac{f_4 \lambda_{SH}}{\lambda_p d}\Lambda = \frac{1}{2}\frac{f_4}{d}\Lambda \tag{4.4}$$

and the corresponding Talbot length of the SH beam can be written as,

$$z^M_{T_{SH}} = \frac{2\Lambda^2_{eff}}{\lambda_{SH}} = \frac{1}{2}(\frac{f_4}{d})^2 \frac{\Lambda^2}{\lambda_{SH}} = \frac{1}{2} z^M_{T_p} \tag{4.5}$$

It is interesting to note that the variable Talbot length in the upconversion process, as indicated by Eq. 4.5, is precisely one-half of the variable Talbot length of the pump beam. While our experimental results in Fig. 4.2 demonstrate the doubling of the Talbot length in the upconversion process, the frequency-doubling of the array and the inverse Fourier transform at the upconverted wavelength effectively reduce the pitch of the microlens array (MLA) to one-half. Consequently, the Talbot length of the upconverted beam is halved compared to the Talbot length at the pump wavelength.

To gain further insight of controlled Talbot effect, we measured the period of the MLA (MLA300-14AR-M) used in the experiment and validated the performance of the imaging setup with the object positioned between lenses L3 and L4, of focal length $f_3 = f_4 = 150$ mm, as depicted in Fig. 4.1. In doing so, we removed the BiBO crystal and the wavelength separator, S, and placed the CCD at the back focal plane of the lens, L4, to record the intensity pattern of the MLA at the pump wavelength. The results are shown in Fig. 4.3. The pictorial design of the MLA, as reproduced in Fig. 4.3(a) from the vendor (Thorlabs), has a two-dimensional array of convex lenses at a pitch of 300 μm. However, using a microscope, we imaged a section of the MLA, as shown in Fig. 4.3, and found the pitch to be 300 μm. A closer look at the image shows concentric circular rings confirming the convex shape of the lens. Now, placing the MLA at two distances, d before the back focal plane of the lens $L3$, we recorded the image of the MLA, with the results shown in Fig. 4.3(c) and (d). As evident from the images of Fig. 4.3(c) and (d) corresponding to the d value of 132 mm and 120 mm, respectively, we clearly see the change in the pitch of the MLA. Counting the number of pixels and

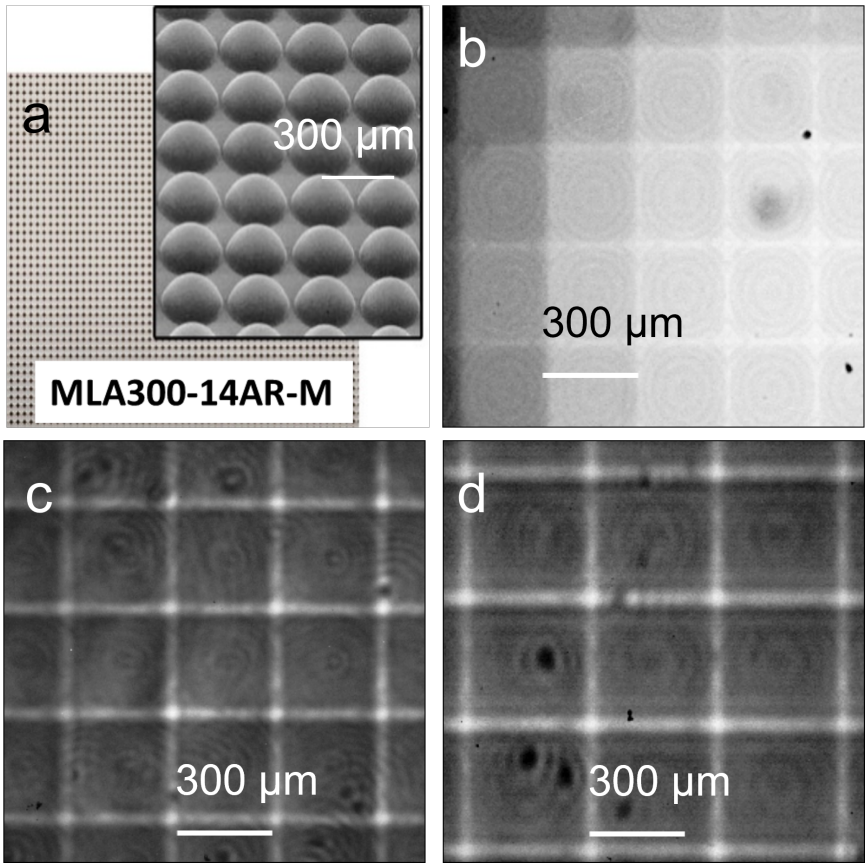

Figure 4.3: a) Schematic design of microlens array (MLA) as provided by the vendor (Thorlabs). b) Microscopic image of the MLA showing the circular diffraction rings due to each microlens. Images recorded at the back focal plane of the lens, L4 for the MLA position, c) $d = 132$ mm and d) $d = 120$ mm, respectively.

multiplying the pixel size, we experimentally measured the change of MLA pitch from 340 μm to 375 μm due to the change of d from 132 mm to 120 mm. Dividing the measured pitches with the magnification factor, (f_4/d), we can find the actual pitch of the MLA to be 300 μm, the same as the value specified by the vendor and also measured using the microscope. Additionally, a closer look at the images of Fig. 4.3(c) and (d) shows the concentric rings, as observed in the microscopic image (see Fig. 4.3(b)) due to the convex shape of the microlenses in the array. The high-quality imaging with the object in between the imaging lens pair, L3 and L4, coupled with simple control of the magnification factor, confirms the possibility of measurement and control of the

Talbot length of the periodic object. This novel experimental scheme facilitates the measurement of extremely small pitches of the periodic object by circumventing the limitations imposed by mechanical constraints in the experiment.

The Talbot carpets in both pump and SHG beam for d = 120 mm, are shown in the Fig. 4.4. The modified Talbot lengths are given by Eq. 4.3 and Eq. 4.5 for Pump and SHG respectively. As mentioned earlier also, The SH Talbot length is half of the pump Talbot length here in this technique whereas the direct SHG of MLA appears to be twice of the pump beam, as shown in Fig. 4.2

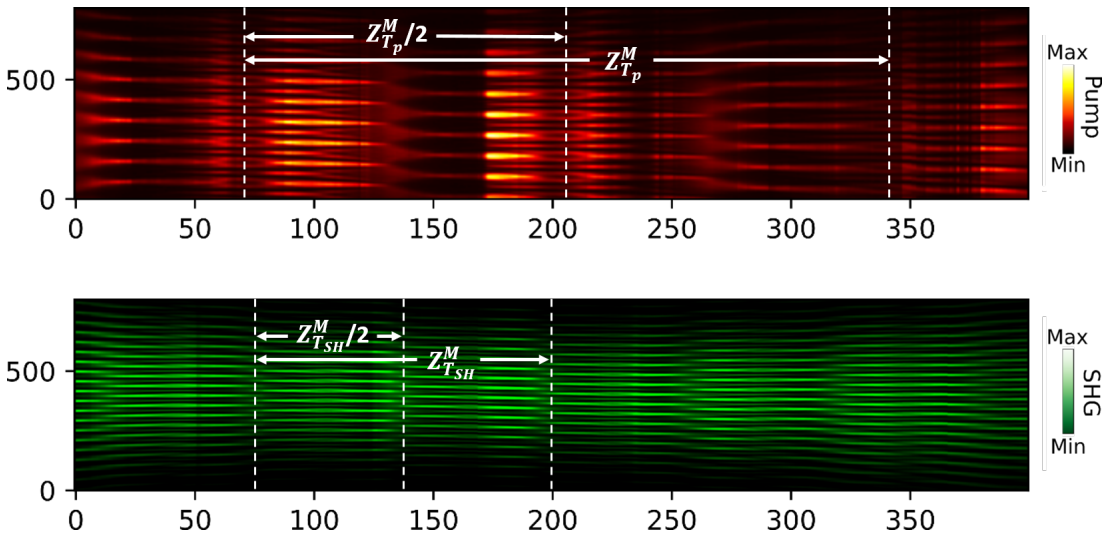

Figure 4.4: Modified Talbot carpets along propagation distance for the periodic object (microlens array) for d = 120 mm. Talbot lengths are modified according to Eq. 4.3 and Eq. 4.5. Note that the SHG Talbot length is halved now as predicted by Eq. 4.5 unlike Fig. 4.2

Confirming the performance of the experimental scheme in terms of simple control of the Talbot length, we recorded the images of the MLA at different fractional Talbot planes and the Talbot planes for both pump and upconverted wavelengths. We removed the BiBO crystal and the wavelength separator to identify the Talbot planes for the pump. But for the upconverted Talbot effect, we placed the BiBO crystal at

the back focal plane of the lens (L_3) and the wavelength separator after the crystal to remove the undepleted pump. Keeping the MLA at a distance, d = 120 mm and 132 mm, from the back focal plane of the lens, L_3, we recorded the Talbot images, with the results shown in Fig. 4.5. As evident from the first row of Fig. 4.5, the image of the MLA placed at d = 120 mm illuminated by the pump wavelength changes with propagation distance, z. Interestingly, the images at $z = 0$ and $z = z_T$ are identical, confirming the Talbot effect. The Talbot length of the MLA for the pump wavelength for d = 120 mm is measured as $z_T = z_{T_p} = 268$ mm. As expected, for $z \neq z_T$, we observe the image recorded at $z = 0.5z_T$ has a transverse shift with respect to the image recorded at $z = 0$. A similar shift is observed between the images recorded at $z = 0.75z_T$ and $z = 1.25z_T$ due to the π phase shift, as commonly observed in Talbot effect [9, 10]. This observation confirms the presence of the Talbot effect. It is to be noted that the circular diffraction pattern due to the convex surface of microlenses, as observed at z = 0 plane, is not visible at other planes along propagation distance. It is evident from Eq. 4.5 that the Talbot length of the periodic object during the upconversion process is half of the Talbot length observed for the object at the pump wavelength. In fact, the images of the upconverted Talbot effect, as shown in the second row of Fig. 4.5, show a 2D array of one-half of MLA's pitch due to the frequency doubling process. As expected, the upconverted Talbot images are identical at $z = 0$ and $z = z_T$, and for propagation distance, $z \neq z_T$, the images vary. Like the Talbot images for MLA at the pump wavelength, in the upconversion process, we also observe the expected transverse shift among the images recorded at $z = 0.5z_T$ and $z = 0$, and $z = 0.75z_T$ and $z = 1.25z_T$, due to the π phase shift. The Talbot length of the upconverted MLA with its position at d = 120 mm is measured to be $z_T = z_{T_{SH}}$ = 124 mm, close to half of the Talbot length at pump wavelength. Having the MLA at d = 132 mm, we observed the Talbot effect for pump and upconverted wavelengths, as shown in the third and fourth rows of Fig.

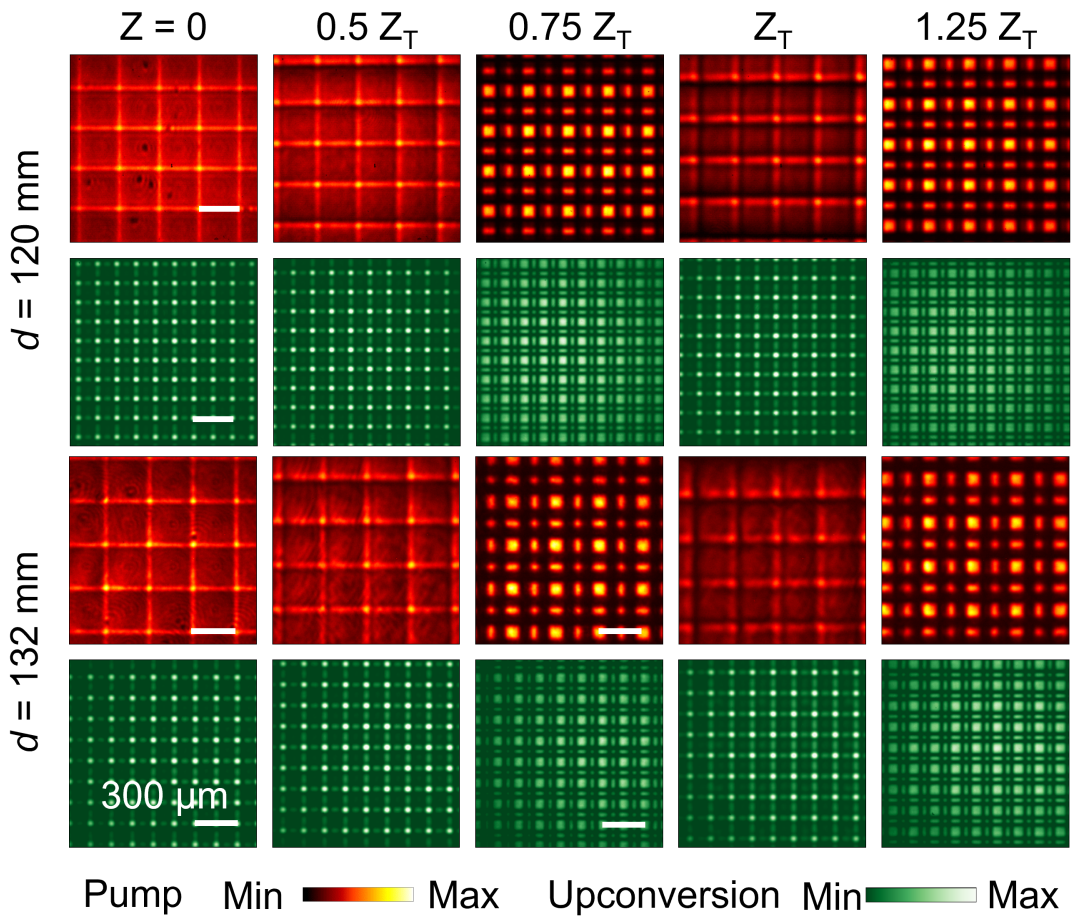

Figure 4.5: Transverse intensity distributions along propagation distance at pump (first and third rows) and SHG (second and fourth rows) wavelengths for two different MLA positions, $d = 120$ mm, and $d = 132$ mm. Self-image planes at 0, $z_T/2$, z_T and fractional Talbot images at $0.75z_T$, and $1.25z_T$ are shown along different columns, at both pump and SHG beam

4.5, respectively. However, due to the decrease in the d value while other parameters remain constant, we expect a decrease in the Talbot length due to the decrease in the effective pitch of the MLA, as predicted by Eq. 4.2 and Eq. 4.3. Experimentally, we measured the Talbot length to be z_T = 220 mm and 104 mm for the pump and upconversion wavelength, respectively. The slight variation in the upconverted Talbot length compared to half of the pump Talbot length can be attributed to the precise positioning of the crystal center concerning the focal plane of lens L_4, considering the focal length

of the MLA lenslets at 18.6 mm and the associated beam shift induced by the crystal. Other contributing factors to the error may include human error in accurately identifying the Talbot plane at SH wavelength, which is more pronounced at lower values of d due to higher longitudinal magnification of the Talbot plane range. It is noteworthy that the upconverted Talbot images lack the circular diffraction pattern typically observed for the pump wavelength. In addition, the boundaries of the arrays appear blurred. This phenomenon can be attributed to the spatial filtering effect inherent in the nonlinear frequency conversion process. It is well known that for any grating structure, the intensity of higher-order spatial frequencies diminishes inversely with the order of the spatial frequency. On the other hand, in the nonlinear parametric process, the efficiency depends on the intensities of the pump beam at the nonlinear crystal plane (in this case, the Fourier plane of lens L_3). Therefore, the intensity of higher-order spatial frequencies of the periodic object is significantly lower in the upconversion process, as if the higher-order spatial frequencies of the object undergo natural spatial filtering during the nonlinear process, leading to the blurring of array boundaries observed in the upconverted Talbot images. This study also demonstrates the potential to control the Talbot length at both the fundamental and upconversion wavelengths by adjusting the position of the periodic object.

To gain a deeper understanding and verify the predicted simple control of the Talbot length according to Eq. 4.3 and Eq. 4.5, we conducted measurements of the Talbot length at both pump and upconversion wavelengths while varying the MLA distance. The results, depicted in Fig. 4.6, corresponds to the MLA distances, d, of 80 mm, 90 mm, 100 mm, 120 mm, and 125 mm for both pump and upconversion wavelengths. It is evident from Fig. 4.6 that the pump Talbot length (represented by black dots), L_T, decreases from 62.4 cm to 26 cm as the MLA separation, d, increases from 80 mm to 125 mm. The theoretical (experimental) magnification factor of the pitch of the

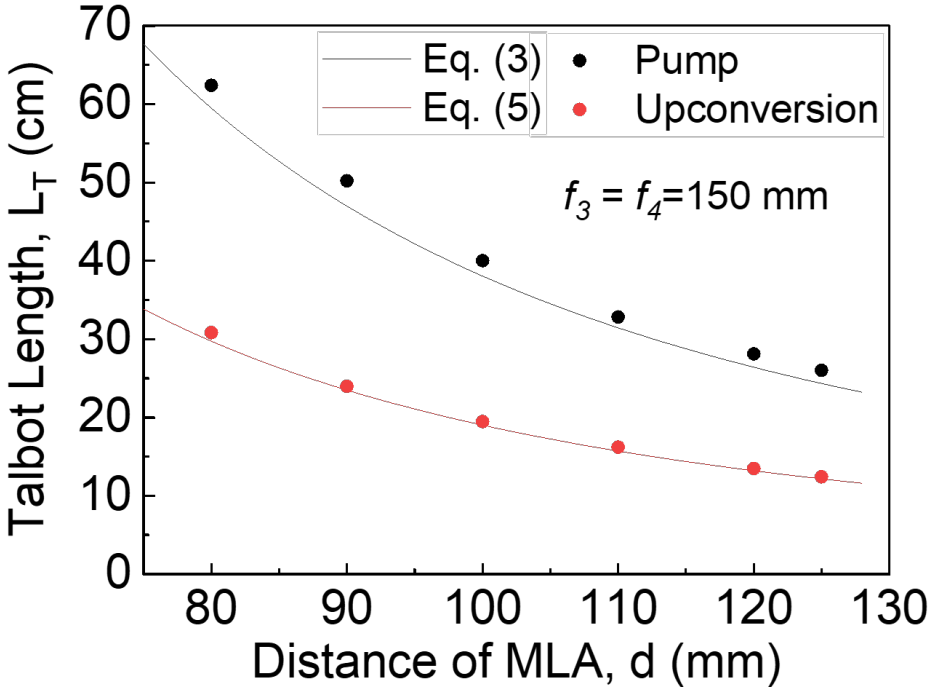

Figure 4.6: Variation of Talbot length at pump and upconversion wavelength as a function of distance, d of MLA away from the back focal plane of the lens, $L3$. The black and red lines are the theoretical results derived using Eq. 4.3 and Eq. 4.5, respectively.

periodic object, ranging from 1.87 (1.91) to 1.2 (1.23) due to the current experimental geometry, results in a magnification of Talbot length from 3.51 (3.67) to 1.44 (1.52) at the pump wavelength. Similarly, the upconverted Talbot length (indicated by red dots) decreases from 30.8 cm to 12.4 cm for the same MLA separation. Both the pump and upconverted Talbot lengths exhibit an inverse square law dependence on the MLA separation, d, closely aligning with the theoretical predictions given by Eq. 4.3 (black line) and Eq. 4.5 (red line). This observation convincingly confirms the potential of the current technique for the simple control of Talbot lengths without altering the parameters of the periodic object. While our study focused on the MLA position, d, at a distance of 80 mm, further reduction in the d value can increase the magnification factor of the pitch of the periodic object. It is essential to note that there is a lower

limit for the d value to ensure the Talbot effect by illuminating the object with a beam size much larger than the pitch of the periodic object. Since the increase in the Talbot length signifies the amplification of the periodicity of the object, this technique offers the potential to measure periodic objects with a small pitch.

Furthermore, it was reported previously [96] that the upconversion (here, SHG) process with very high efficiency is feasible by controlling the input pump intensity and employing a nonlinear crystal with a high figure-of-merit. While periodically poled crystals offer higher figure-of-merit, their low aperture poses a limitation. In our setup, we opted for a BiBO crystal, which, although possessing a moderately high figure-of-merit, features a larger clear aperture. To boost the pump intensity, we replaced lenses L3 and L4 with shorter focal length lenses, setting $f_3 = f_4 = 25$ mm. With an average pump power of 3.47 W, our setup produced upconverted Talbot images with an average power of 0.351 W, achieving a single-pass nonlinear frequency upconversion efficiency as high as $2.91\%W^{-1}$. This efficiency represents a substantial improvement, exceeding the efficiency reported in the prior study [60] by a factor of 10^6.

4.4 Implications

The demonstrated method enables precise control of Talbot planes at both fundamental and second harmonic wavelengths, offering a powerful tool for high-resolution imaging and measurement of fine periodic structures without reliance on sophisticated microscopy. The high-efficiency nonlinear upconversion technique holds strong potential for advancing Talbot lithography, high-energy beam shaping, optical metrology, and future integrated optical systems requiring compact, efficient nonlinear Talbot-based architectures.

4.5 Conclusion

In summary, our study has successfully demonstrated single-pass second harmonic generation of the Talbot effect with notable conversion efficiency. We employed the microlens array as a two-dimensional periodic object illuminated with pump radiation at a wavelength of 1064 nm and investigated the single-pass upconversion of the periodic object in a 1.2-mm-long BiBO crystal. We confirmed the doubling of the Talbot length in the upconversion (SHG) process, at first. Then, using the theory of Fourier transform, we generated an experimental method to produce tunable Talbot lengths in both pump and upconverted wavelengths while accessing significantly enhanced nonlinear conversion efficiency. Our technique enabled precise adjustments of the Talbot planes for specific distances, allowing measurements of periodic objects with low pitch without sophisticated microscopes. The highly efficient nonlinear upconversion of Talbot imaging demonstrated in this study holds potential for applications in Talbot lithography and other high-energy scenarios involving Talbot effect.

Chapter 5

Sensing Periodicity using Tunable Talbot Lengths

5.1 Introduction

Talbot effect has emerged as a versatile tool with diverse applications in the realms of metrology and sensing. This self-imaging phenomenon, in which a periodic optical pattern is reproduced at equidistant planes along the propagation axis, has found innovative uses in various fields, including coherent optical signal processing, device technology,and the monitoring of physical quantities [23]. One of the key contributions of the Talbot effect has been in the field of metrology, where it has enabled the development of advanced wavefront sensing techniques. By leveraging the periodic nature of the Talbot pattern, researchers have devised electro-optical processors capable of precisely measuring displacement with resolutions better than 10 μm and dynamic ranges of up to 1.5 mm [98]. This method utilises the linear relationship between the Talbot pattern and the measured displacement, hence creating a simple and effective solution

without the need for complex numerical signal processing. The Talbot effect has also found applications in the field of optical sensing, where it has been utilized to develop innovative spectrometric and holographic techniques. Using a tilted absorption grating and a CCD camera, researchers have developed a compact transform spectrometer that utilizes Talbot self-images, ensuring consistent resolution across wavelengths and supporting spectrometer arrays without any moving parts [99]. In digital holography, the Talbot self-imaging phenomenon has been observed and investigated, leading to the proposal of a simple spectrometer based on this principle. By numerical reconstruction of holograms, the Talbot self-imaging effect can be used to extract spectral information, offering a compact and versatile solution for spectroscopic applications [100]. Recently, a miniaturised version of Talbot spectrometer has been employed, using Fourier transform of the Talbot lengths, to measure wavelengths below 1 nm [72]. Talbot effect has been also explored in the context of Fibonacci geometry, where the self-similarity of the scaling Fourier spectrum leads to the emergence of multiscale Talbot patterns [101]. Furthermore, parallel phase-shifting digital holography based on the fractional Talbot effect has been reported [102], which leverages the periodic phase distribution in the fractional Talbot image of a grating, allowing simultaneous reconstruction of objects located at different distances from the CCD sensor. Use of Talbot effect has also been reported for measurement of precise displacements [103]. Very small gratings and shapes can be measured using x-ray Talbot interferometry for small angle scattering [104]. In the strong imaging regime, where frequencies exceed $1/\lambda$, super-oscillations allow sub-wavelength imaging with grating waves, offering advantages over imaging with evanescent waves. In the last decade, many attempts have been made to create super-oscillatory lens and further exploit it for super-resolution or sub-wavelength imaging [83, 105]. However, sensing subwavelength variations in periodicity through direct measurement of Talbot length has not been delved into yet.

Here, we extend our scheme of tunable Talbot length to measure the variation of a grating period on subwavelength scale. In chapter 3 we have seen the theoretical and experimental aspects of tunable Talbot lengths and in chapter 4 we have seen the nonlinear upconversion of Talbot effect with tunable Talbot lengths. To produce tunable Talbot length, we use the same technique as discussed in chapter 3. We measure variations of 300 nm with grating periods of a multi grating crystal using a 632.8 nm wavelength laser.

5.2 Theory and experimental scheme

The effective periodicity, Λ_{eff} on the image plane as derived in chapter 3, Eq. 3.3, is given by

$$\Lambda_{eff} = \frac{f_4 \lambda}{\Lambda'} = \frac{f_4}{d}\Lambda \tag{5.1}$$

and consequently the modified Talbot length,

$$Z_T^M = \frac{2\Lambda_{eff}^2}{\lambda} = \left(\frac{f_4}{d}\right)^2 \left(\frac{2\Lambda^2}{\lambda}\right) = \left(\frac{f_4}{d}\right)^2 Z_T. \tag{5.2}$$

From Eq. 5.2, it is evident that the magnification factor, (f_4/d), validates the relatively longer range of Talbot length. Hence for a small variation of the grating period ($\Delta\Lambda$) would be more conveniently detectable using the following equation,

$$\Delta\Lambda = \frac{1}{2\sqrt{2}} \sqrt{\frac{\lambda}{Z_T^M}} \left(\frac{d}{f_4}\right) \Delta Z_T^M. \tag{5.3}$$

Here ΔZ_T^M is the variations in modified Talbot length due to the variations in periodicity. Evidently, the increased magnification factor (f_4/d) and modified Talbot length (Z_T^M) probe into smaller values of variation in grating period of the object ($\Delta\Lambda$). Such

observations indicate that this system architecture can be used as a sensor to measure small variations in grating period.

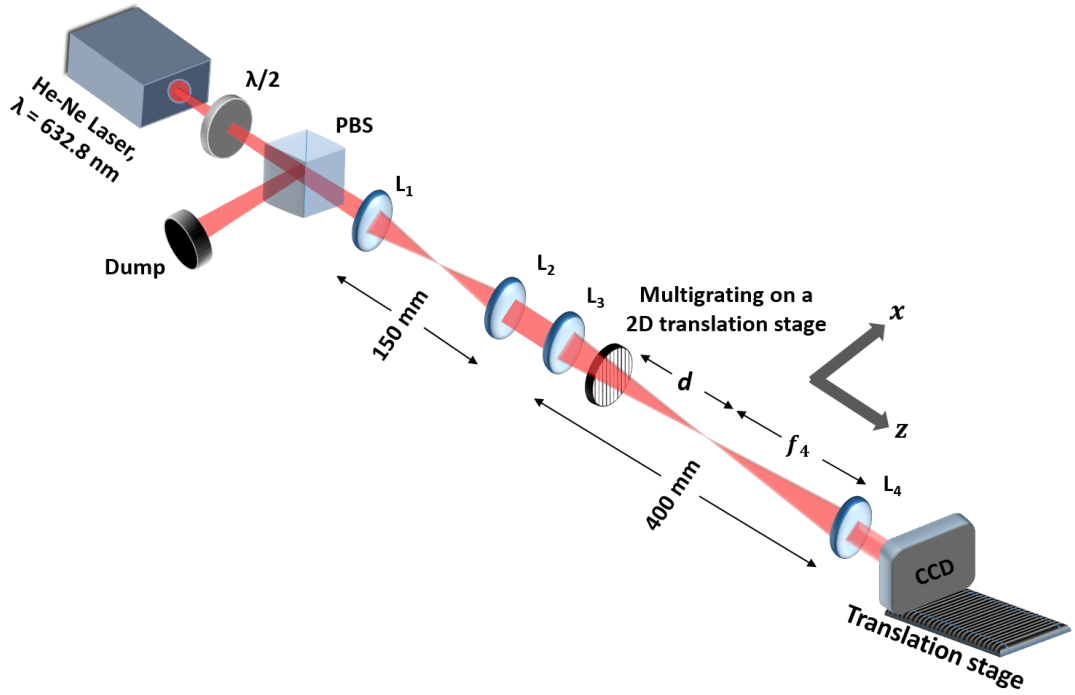

Figure 5.1: Schematic of the experimental setup for sensing variation in grating period using tunable Talbot effect. $\lambda/2$, half-wave plate; PBS, polarizing beam splitter cube; L_{1-4}, plano-convex lenses

To experimentally verify the ability of this architecture for sensing small variations of grating period, In the absence of a suitable periodic object, we used a 1D multi-grating periodically poled Lithium Niobate (PPLN) crystal with the grating period varying from 18.2 μm to 19.7 μm with an increment of 300 nm. The schematic of the experimental setup is shown in Fig. 5.1. A He-Ne laser with wavelength 632.8 nm is used as the input radiation for the setup, with its power varied using a half-wave plate ($\lambda/2$) and a polarizing beam-splitter (PBS) cube. The input beam is expanded and collimated using a telescopic lens combination comprising two lenses, L_1 and L_2, of focal length, $f_1 = 50$ mm, and $f_2 = 100$ mm, respectively, to collimate the laser beam into a near plane wavefront. A lens, L_3, of focal length, $f_3 = 200$ mm, is used

to Fourier transform the phase profile of the multi grating crystal of periods lying in the range of 18.2 μm to 19.7 μm with an increment of 300 nm. We illuminated the multi grating crystal across the periods, placed on a two dimensional translation stage at a distance, d, from the back focal plane of the lens L_3. The lens, L_4, is placed at a distance, f_4, from the Fourier plane of L_3, to inverse Fourier transform the array of the spatial structure of the input beam (here Gaussian beam) generated due to the Fourier transform of the multi grating crystal at the back focal plane of the lens, L_3. At the image plane of the lens L_4, we placed the CCD camera on another translation stage along the beam propagation to record the Talbot planes. We recorded the Talbot lengths for three different values of control parameter, d = 40 mm, 70 mm and 100 mm and also for $4f$ imaging. To create the Talbot carpets, we plotted the line profiles of CCD images along the propagation distance, by extracting the intensity profile from a fixed horizontal pixel line from each CCD image and concatenating these lines to form a continuous image.

It is evident from Eq. 5.3, that the magnification factor, (f_4/d), with the control parameter d, plays a crucial role in high-resolution sensing of variation in the periodicity. The value of d can vary from $d = f_3 - t$ (where t is the combined distance of mechanical constraints to approach the object to the effective plane of lens), to $d = 0$ (while the object placed at the back focal plane of the lens, L_a), scaling the magnification factor from 1 to infinity. However, a decrease of d results in a decrease in illuminated area and hence the number of periods of the periodic object. Thus we restricted the value of d being very small, so that effective number of grating periods illuminated are large enough to produce Talbot effect. Also, the longitudinal magnification gets affected due to very small value of d, which we will discuss in the result section.

5.3 Results and discussion

The longitudinal magnification of the Talbot range empowers us for sensing small variation of the grating period. The modified Talbot length following Eq. 5.2 provides the necessary insight for effective periodicity, Λ_{eff} given by, $\Lambda_{eff} = \sqrt{\frac{\lambda Z_T^M}{2}}$. The Talbot lengths for each period of grating, and correspondingly the effective periodicities, Λ_{eff} for all three d values and for $4f$ imaging were measured. Talbot carpets for all the six grating periods are not shown here. Only for periods 18.8 μm and 19.1 μm are shown in the Fig. 5.2 and Fig. 5.3 respectively.

Experimentally, for the grating position of $4f$ condition, d = 100 mm, 70 mm, and 40 mm, we measured respective Talbot length variation of 1.07 - 1.25, 4.20 - 4.99, 8.71 - 10.04 and 26.15 - 30.87 mm for the grating period variation from 18.2 - 19.7 μm. As evident, we observe a large Talbot length variation (4.72 mm) for a grating period variation of 1.5 μm while placing the object at d = 40 mm, indicating the possibility of high measurement resolution for a Talbot-based sensor. Using Eq. 5.2 and the measured Talbot length Z_T^M, we have calculated the effective grating period (Λ_{eff}) for the change of period Λ with the results shown in Fig. 5.4

As shown in Fig. 5.4, the experimentally measured effective Talbot length, Λ_{eff}, varies linearly with the actual grating period, Λ, over ranges of 18.44 - 19.91, 36.44 - 39.75, 52.50 - 56.36, and 90.97 - 98.82 μm. Using Eq. **??**, the fitting (solid line) to the experimental data (dots) demonstrates a close agreement between theory and experiment, with slopes of 1, 2, 2.85, and 5, precisely matching the values of (f_b/d) for changes in the grating period from 18.2-19.7 μm, and the object positions satisfying the $4f$ imaging condition, d = 100 mm, 70 mm, and 40 mm. It is also interesting to note that the measured effective grating period lies within the measurement error bar for all

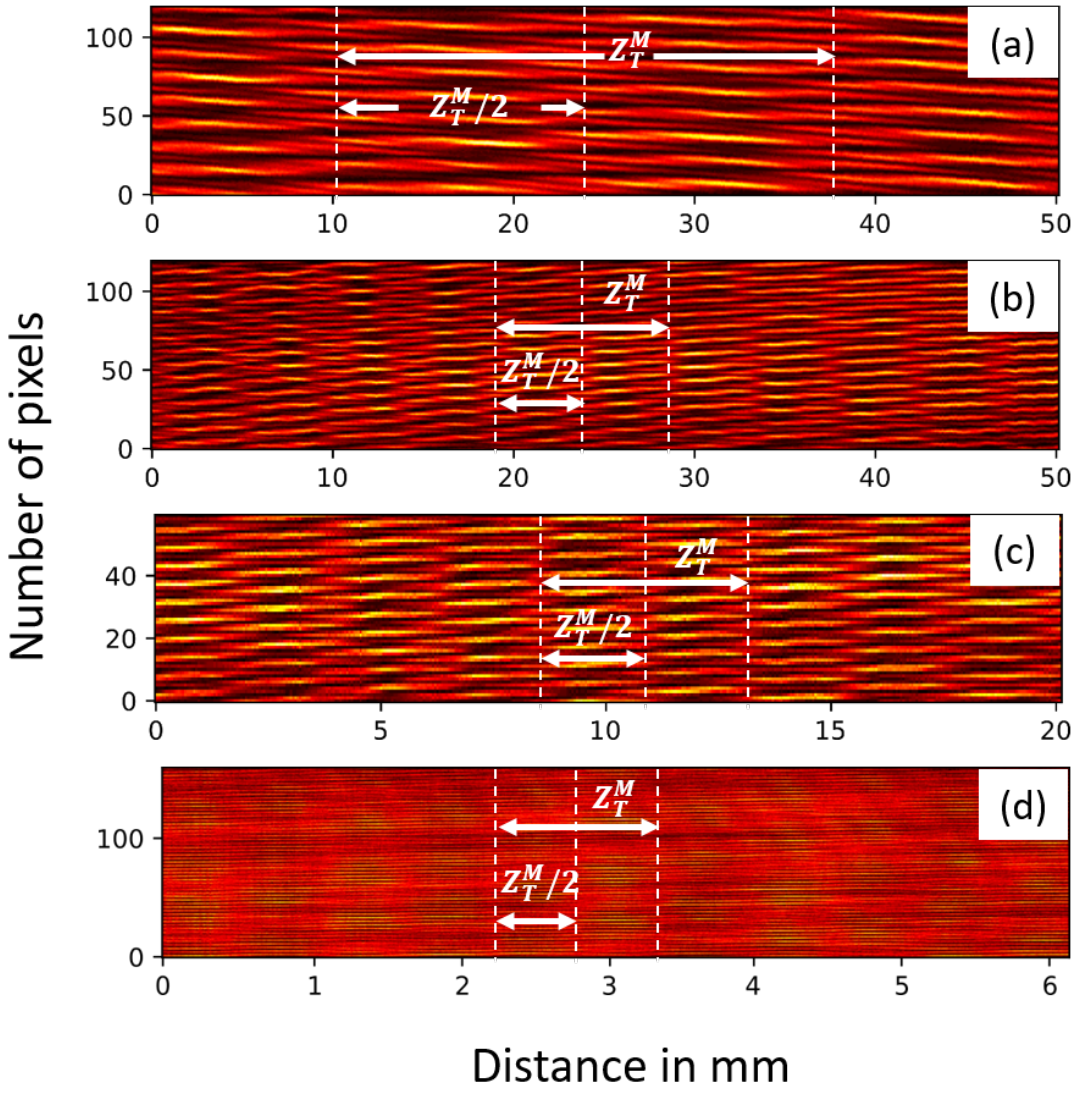

Figure 5.2: Talbot carpets of 18.8 μm grating period for different values of the control parameter, d. (a), (b), (c) and (d) represents d = 40 mm, d = 70 mm, d = 100 mm and $4f$ imaging respectively

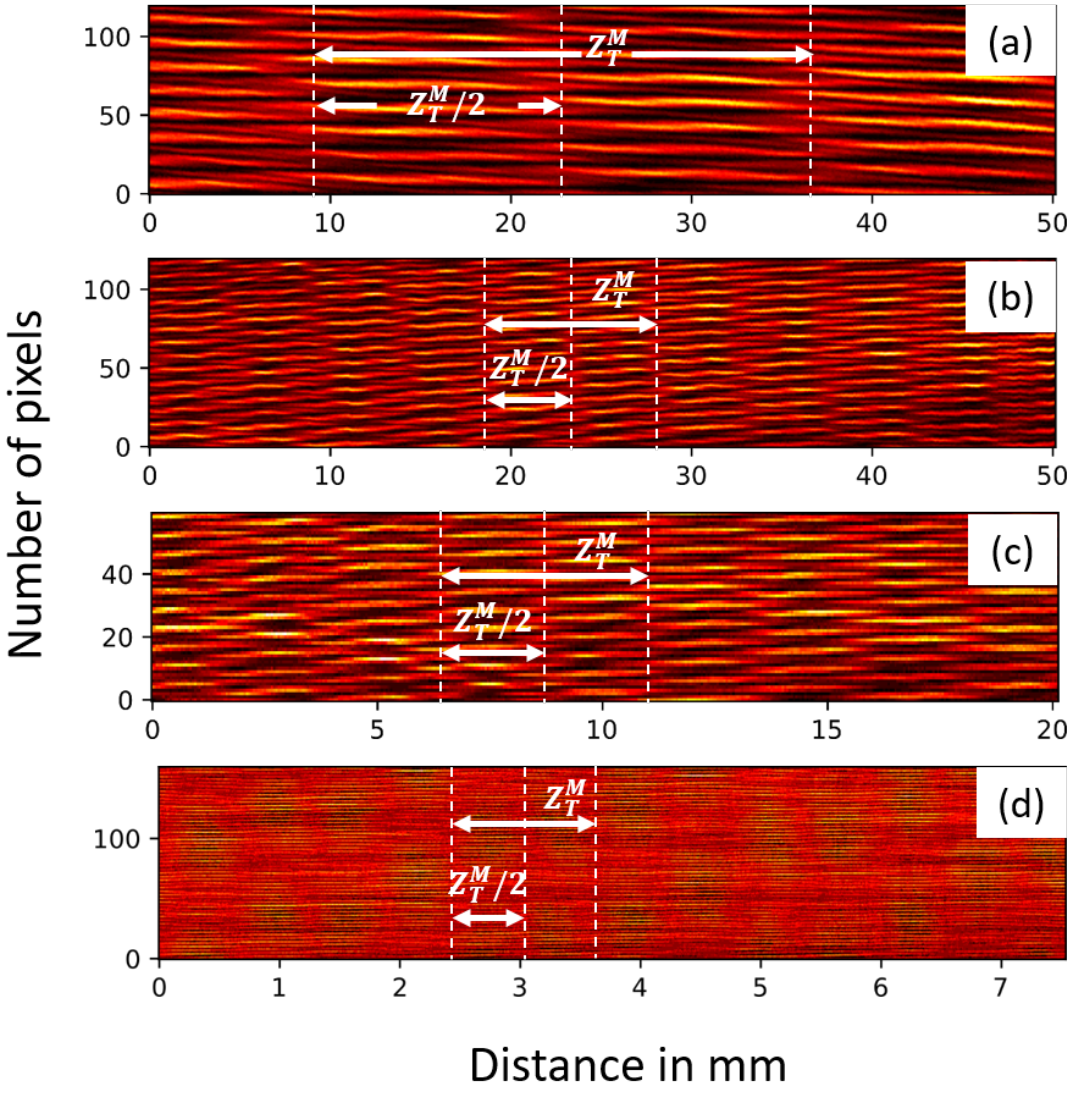

Figure 5.3: Talbot carpets of 19.1 μm grating period for different values of the control parameter, d. (a), (b), (c) and (d) represents d = 40 mm, d = 70 mm, d = 100 mm and $4f$ imaging respectively

d values except d = 40 mm. In fact, for d = 40 mm, as evident from the purple line and dots of Fig. 5.4, one can clearly distinguish two grating periods (see the black dash and black arrows) with a difference of 600 nm. However, to get a better perspective on the resolution of the Talbot-based sensor, we have summarized the measurement data in Table 5.1. As evident from the table 5.1, the measured grating period for the object position satisfying $4f$-imaging condition has an error of $\pm$ 1.3 μm. Such high error can be attributed to the measurement inaccuracy resulting from the lower resolution ($\sim$10 µm) of the transnational stage used to measure the relatively small Talbot length of the grating under the $4f$-imaging condition. On the other hand, the increase in Talbot length due to the use of shorter d values — 100 mm, 70 mm, and 40 mm — we observe an improvement in measurement accuracy from $\pm$0.65 μm, $\pm$0.42 μm to $\pm$0.21 μm, respectively.

Table 5.1: Measured grating periods for different positions of the object

Grating period, Λ (μm)	Measured grating period from experiment, $\frac{d}{f_4}\Lambda_{\text{eff}}$ (μm)			
	$d = 40$ mm	$d = 70$ mm	$d = 100$ mm	4f imaging
18.2	18.19 ± 0.21	18.34 ± 0.42	18.10 ± 0.65	18.45 ± 1.37
18.5	18.47 ± 0.20	18.44 ± 0.42	18.39 ± 0.64	18.67 ± 1.35
18.8	18.77 ± 0.20	18.64 ± 0.41	18.92 ± 0.62	19.02 ± 1.33
19.1	18.98 ± 0.20	19.26 ± 0.40	19.13 ± 0.61	19.34 ± 1.31
19.4	19.52 ± 0.19	19.33 ± 0.40	19.40 ± 0.60	19.64 ± 1.29
19.7	19.76 ± 0.19	19.69 ± 0.39	19.74 ± 0.59	19.91 ± 1.27

In fact, for d = 40 mm, the Talbot-based sensor can measure a change in the grating period as small as $\sim$450 nm for a grating period of 18.2 μm. It is also evident from the Table that for a constant value d, the measurement error or the resolution, as also evident from Eq. 5.3, improves with the increase in the grating period. For example, as evident from the second column of Table 5.1, the measurement error improves from $\pm$0.21 μm to $\pm$ 0.19 μm for the increase of grating period from 18.2 μm

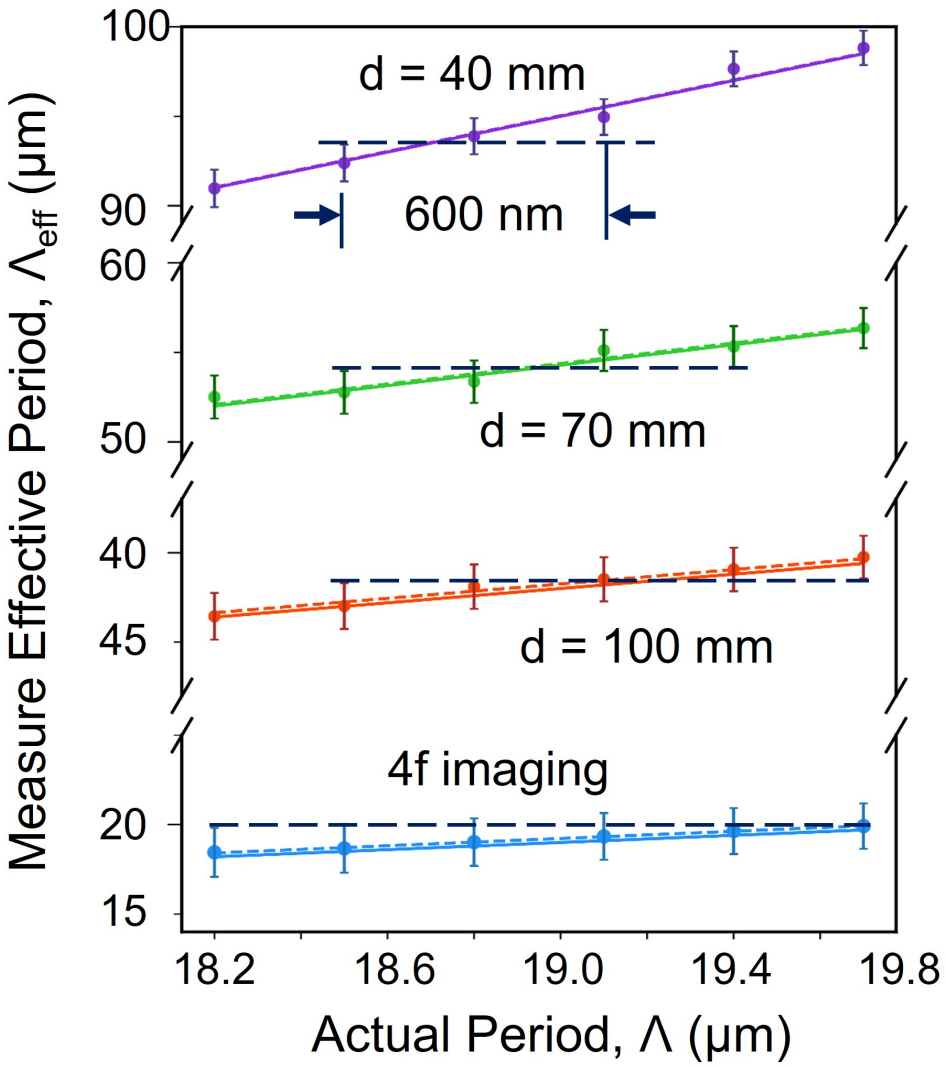

Figure 5.4: Variation of effective periodicity, Λ_{eff} as a function of the actual periodicity, Λ of the multi-grating crystal, for different position of the object satisfying $4f$ imaging condition, d = 100 mm, 70 mm and 40 mm. The solid lines are the theoretical results derived using the experimental parameters in Eq. 5.1. The black dash line and black arrows are used to identify the measurement resolution.

to 19.7 μm. The experimental errors in measuring the modified Talbot length (ΔZ_T^M) vary for different d values, as we mentioned earlier in chapter 3 that the error while detecting the Talbot length increases for a higher longitudinal magnification of Talbot range. The errors in measuring modified Talbot length, ΔZ_T^M are 0.3 mm, 0.2 mm, 0.15 mm and 0.08 mm respectively for d = 40 mm, d = 70 mm, d = 100 mm and for $4f$ imaging. Although the error in Z_T^M increases for higher longitudinal magnification, the measured grating period has a decreasing trend with increasing magnification, due to higher value of $(\frac{f_4}{d})$ in Eq. 5.3. These results establish the reliability of the Talbot-based sensor in measuring changes in the grating period, or any physical parameter influencing the grating period of an object, by 450 nm without requiring complex microscopic measurement systems. While large magnification factors in microscopic systems involving intricate lens designs and aberration control have traditionally been necessary for such precision, the current results demonstrate the potential for achieving similar measurements for a periodic object systematically placed between two long focal-length lenses.

5.4 Implications

The ability to sense subwavelength variations in grating periodicity using a tunable Talbot length opens new possibilities for precision metrology, structural characterization, and quality control in microfabrication and nanophotonics. This technique offers a compact, non-invasive alternative to conventional microscopy for detecting fine spatial features and can be adapted for dynamic sensing in material science, optical inspection, and biosensing platforms.

5.5 Conclusion

We produced tunable Talbot length for a range of grating periods which allowed the sensor to detect periodicity variations of 450 nm for a grating period as small as 18.2 μm with a 632.8 nm wavelength laser, demonstrating the capability to operate in the subwavelength regime without relying on microscopic systems. This sensing technique can be extended to other areas of research where high precision measurement is required with dynamic sensitivity.

Chapter 6

Sensing Aberration of a Thick Lens using Non-paraxial Talbot Effect

6.1 Introduction

Aberrations in optical systems are deviations from the ideal performance, where light rays fail to converge at a single point after passing through lenses or mirrors, leading to blurred or distorted images. Among the various types of aberrations, spherical aberration is particularly significant in optical design. It occurs when light rays passing through a lens near its edge are refracted more than those passing near the center, causing them to focus at different points along the optical axis. This phenomenon degrades image quality and is a critical challenge in high-precision optical systems such as telescopes, microscopes, and cameras.

To address aberrations, various corrective methods have been developed. Spherical aberration is a major concern in optical systems that require high resolution. The

Talbot effect can be leveraged to analyze and correct spherical aberrations by studying the self-imaging patterns of periodic structures under aberrated wavefronts. The Talbot effect's sensitivity to wavefront distortions makes it a valuable diagnostic tool. When an optical system with spherical aberration is illuminated by coherent light, the resulting Talbot image can reveal the nature and extent of the aberration.

As previously discussed, the Talbot effect, first observed in the 19th century, is characterized by the periodic reproduction of an image when light passes through a structured grating. This self-imaging occurs at regular intervals, with the specific distances, known as Talbot planes, marking the points where these images reappear. The length at which this replication occurs, the Talbot length, is a key factor in understanding the propagation of light through periodic structures, as derived by Lord Rayleigh [22],

$$z_T = \frac{\lambda}{1-\sqrt{\left(1-\frac{\lambda^2}{\Lambda^2}\right)}} \approx \frac{2\Lambda^2}{\lambda}. \tag{6.1}$$

In Eq. 6.1 the approximation does not hold for non-paraxial Talbot effect where the grating period is not much greater than the incident wavelength, $\Lambda \not\gg \lambda$ [35].

In conventional optical systems, the Talbot effect is typically observed under the paraxial approximation, which assumes that light rays make small angles with the optical axis. However, many real-world optical systems operate outside these small-angle conditions, necessitating an understanding of the Talbot effect in non-paraxial contexts [106]. It has been found that the self-imaging phenomenon persists even in non-paraxial conditions, though with altered characteristics due to the impact of aberrations. This extension of the Talbot effect opens new possibilities for measuring and correcting aberrations in optical systems where paraxial assumptions do not hold, such as in wide-angle lenses and deep-field microscopes.

The practical application of the Talbot effect has been effectively demonstrated in the measurement of wavefront aberrations, particularly within the human eye [107]. By employing a two-dimensional grating to produce Talbot images, this method enables precise measurement of wavefront aberrations within the optical system of the eye. This technique is especially valuable in ophthalmology, where accurate assessment of aberrations is essential for the design of corrective lenses and the optimization of surgical procedures.

Adaptive optics systems, which are critical for correcting real-time aberrations in fields such as astronomy and microscopy, rely heavily on precise wavefront sensing. The Talbot effect has been successfully incorporated into wavefront sensors, significantly improving their sensitivity to aberrations [108]. These sensors can dynamically adjust to correct for aberrations, thereby enhancing image quality in environments where wavefront distortions are constantly fluctuating, such as in astronomical observations where atmospheric turbulence affects incoming light.

In post-paraxial regimes, the Talbot effect has been shown to produce complex aberration-like cusped focusing patterns [109]. These patterns, which closely resemble aberrations themselves, offer new insights into the understanding and correction of higher-order aberrations. By analyzing these cusped focusing patterns, more effective strategies can be developed for controlling aberrations in advanced optical systems, including those used in quantum optics and high-precision lithography.

For a higher magnification, we generally use thick lenses as the objective lens of a telescopic lens systems. When the radius of curvature of the lens becomes comparable to the radius of the aperture of the lens, we have to consider such a lens to be a thick lens. While imaging non-paraxial Talbot effect, with a thick lens, the diffracted beams undergo spherical aberration of the lens. Hence, we could use our measurement of

Talbot length for sensing spherical aberration of the lens. Here, we used non-paraxial Talbot effect for sensing spherical aberration of a thick lens and hence predicted its focal length for variable grating periodicity theoretically, and verified it experimentally by measuring the magnified Talbot lengths.

6.2 Theory and experimental scheme

The scheme of tunable Talbot length has the constraints of a limited decrement of the control parameter (d), as discussed in the last part of the section 5.2 of the previous chapter. Therefore, to obtain magnified Talbot length for a grating period compared to 10 μm or even smaller, we used a different approach of magnification, i.e., using $4f$ imaging technique with two lenses f_a and f_b. The ratio of the focal lengths of the lenses, $(\frac{f_b}{f_a})$ is much higher compared to our previous scheme of tunable Talbot effect, providing a much higher but constant magnification. We used the $4f$ imaging technique in this case unlike the tunable Talbot scheme because we are not going to explore the potential applications on lithography or tunable Talbot interferometry, rather we need a higher magnification here to explore non-paraxial Talbot range for sensing aberration of a lens. We used a Yb fiber laser of wavelength 1064 nm as the source and used the 1st lens, L_a of focal length, f_a = 25.86 mm (for 1064 nm wavelength) with aperture size of 25.4 mm. We used lenses, L_b of two different focal lengths, i.e. 304.95 mm and 507.86 mm (both for 1064 nm laser) for appropriate magnification of respective grating periods. The experimental scheme is depicted in Fig. 6.1 From specifications of the collecting lens, L_a having focal length, f_a = 25.86 mm and aperture size 25.4 mm, it appears to be a thick lens and hence gives rise to spherical aberration. The measured Talbot lengths enable to measure the change in effective focal length and hence to detect the spherical aberration.

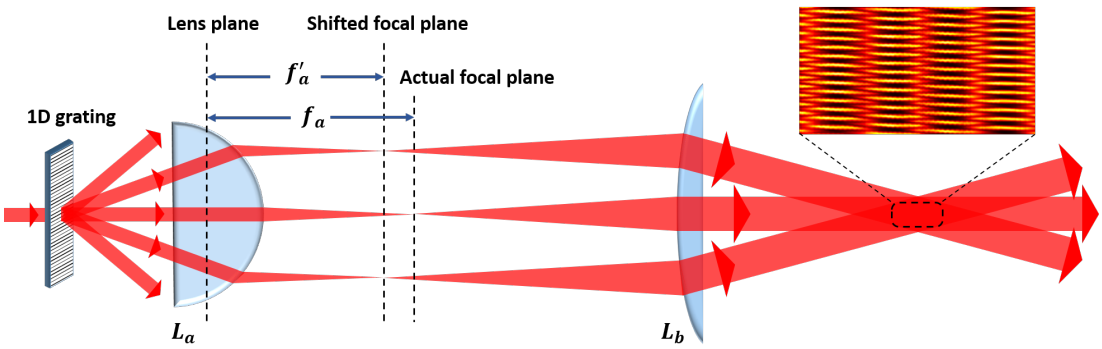

Figure 6.1: Experimental scheme for sensing spherical aberration of a thick lens. Diffracted beams from a 1D grating are collected and superposed to produce magnified Talbot length (shown in the inset intensity profile), using the lenses L_a and L_b . The effective focal length, f'_a, of the lens L_a, is reduced as shown due to spherical aberration.

A lens with focal length of 25.86 mm and aperture size of 25.4 mm (as given in Thorlabs website), has variable focal length as one increases the beam width, resulting to spherical aberration. A lens yields a multiplicative phase transformation factor given by $E(x,y) \sim \exp\left[\frac{ik}{2f_a}\left(x^2+y^2\right)\right]$ under paraxial approximation, where x and y are the transverse position coordinate of the beam with wave-vector k on the lens plane and f is the focal length of the lens. This approximation holds under the condition of $x,y << f_a$. But to use the lens as the collecting optics for diffracted beams of higher spatial frequencies emerging from a grating element of a very small grating period (less than 10 μm or so) placed at the back focal plane of the lens, we need to get rid of the paraxial approximation and modify the formula for focal length. Without any approximation, the phase transfer function due to a lens is given by,

$$E(x,y) \sim \exp\left[\frac{ik}{f_a}R^2\left[1-\sqrt{1-\frac{x^2+y^2}{R^2}}\right]\right] \tag{6.2}$$

for a plano convex lens (since we are using plano convex lens only in the experiment) with radius of curvature R. Physically, we observe aberration, i.e. the focal length getting shortened ($f_a \rightarrow f'_a$) to be valid for paraxial approximation and thus the multi-

plicative phase factor, with the modified focal length f', can be written as

$$E(x,y) \sim \exp\left[\frac{ik}{2f'_a}\left(x^2+y^2\right)\right]. \tag{6.3}$$

Comparing Eqs. 6.2 and 6.3, the modified focal length due to aberration comes to be,

$$f'_a = \frac{f_a\left(x^2+y^2\right)}{2R^2[1-\sqrt{1-\frac{x^2+y^2}{R^2}}]}. \tag{6.4}$$

In our case, the diffraction is taking place from a 1D grating and thus y-coordinate is not required. The 1st order diffraction maxima emerging from a grating (placed at the focal plane of the lens) of grating period, Λ, appear at a horizontal position x in the transverse plane of the lens which is f distance apart from the grating. The position x can be determined from the diffraction equation given by,

$$\frac{x}{f_a} = \tan(\sin^{-1}(\frac{\lambda}{\Lambda})) \tag{6.5}$$

and thus the effective focal length, f'_a is plotted against the grating period, Λ using the Eq. 6.4 (where x comes from Eq. 6.5), as shown in the Fig. 6.2. The simulation shows that the effective focal length of the thick lens reduces drastically, for grating periods shorter than 10 μm or in better words, as we approach the non-paraxial Talbot regime.

In experiment, we used different gratings with known periods and measured the Talbot length for each case, with the experimental scheme depicted in Fig. 6.1. As the grating is placed at the back focal plane of the lens L_a, the diffracted beams get parallel to each other after the lens L_a. Each diffracted beams are supposed be focused at the focal plane of L_a, but due to the thickness of the lens, the higher order spatial frequencies get focused at a smaller distance and hence we call it effective focal length,

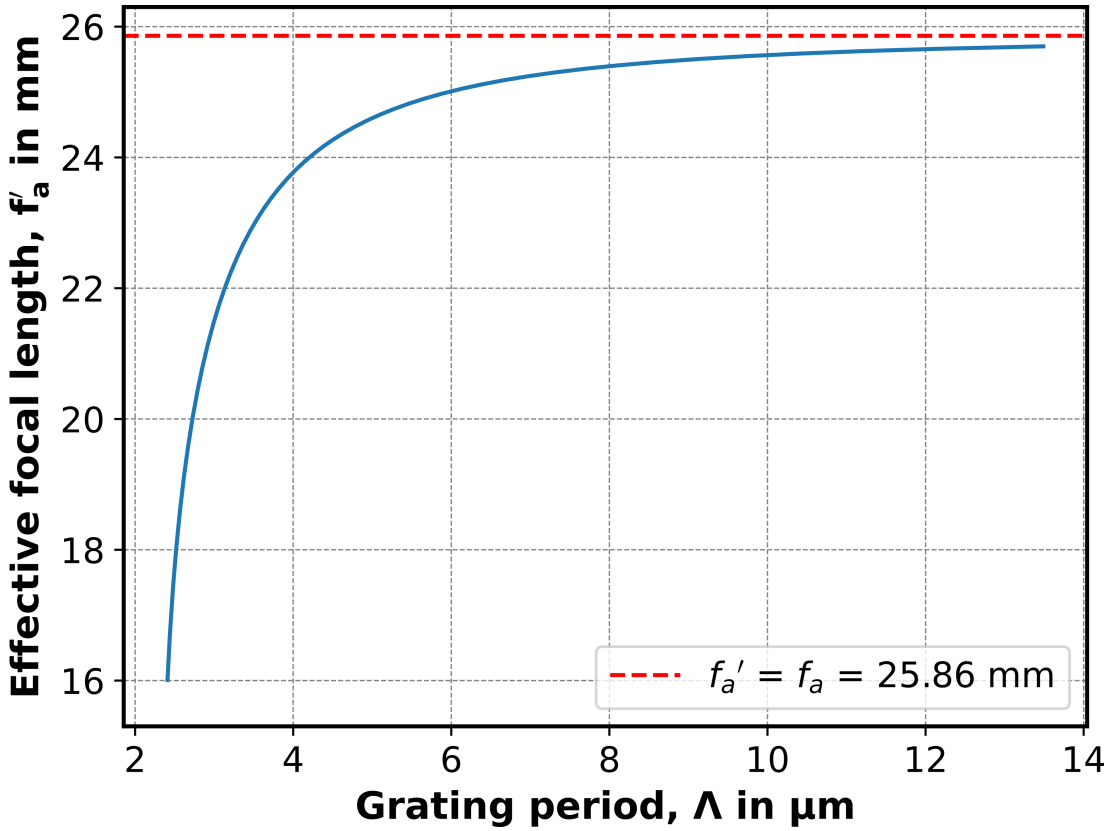

Figure 6.2: Effective focal length, f_a' is simulated against the grating period, Λ, revealing aberration of the lens L_a

f_a', because the spatial frequencies are responsible to recreate the image of the grating at the image plane (not the dc part of the beam). From this experimental scheme, the magnified Talbot length (Z_T'), for any known period (Λ), can be measured as,

$$Z_T' = \left(\frac{f_b}{f_a'}\right)^2 \left(\frac{2\Lambda^2}{\lambda}\right)$$

and the measured Talbot length at the image plane infers the effective focal length, f_a' given by,

$$f_a' = \frac{f_b \Lambda}{\sqrt{\frac{\lambda Z_T'}{2}}}. \tag{6.6}$$

We used ronchi gratings of periods 11.11 μm, 10 μm, 9.09 μm, 8.33 μm, 7.69 μm and 6.67 μm respectively (a part of Thorlabs R1S1L1N Negative Test Target). Due to unavailability of a grating of period less than those of mentioned above, we used a PPKTP crystal of period 3.425 μm as a grating, placed across the beam to illuminate the grating periods. In this scheme as depicted in Fig. 6.1, We used the first lens, L_a, of focal length f_a = 25.86 mm. To record the image in CCD, we used the second lens L_b, of two kind of focal lengths, f_b = 304.95 mm for grating period 11.11 μm to 6.67 μm and f_b = 507.86 mm for grating period 3.425 μm respectively, for necessary magnification in respective cases. These focal lengths are for 1064 nm wavelength light.

6.3 Experimental results

As discussed in the section 6.2, for sensing aberration experimentally, the magnified Talbot length has been measured for the respective grating periods. For the given grating periods of 11.11 μm, 10 μm, 9.09 μm, 8.33 μm, 7.69 μm and 6.67 μm, the measured Talbot lengths are 32.9 mm, 26.9 mm, 22.1 mm, 18.7 mm, 16.2 mm and 12.3 mm respectively, which are shown in the Fig. 6.3. For the PPKTP crystal with length 3.425 μm (used as a grating), the lens L_b with a different focal length (f_b = 507.86 mm) was used to image the grating and subsequently the Talbot carpet as shown in the Fig. 6.4. For the 3.425 μm grating, curved lines appear which are possibly manifested due to some other spatial frequencies generated from the PPKTP crystal since it is a periodically poled phase grating. However, this effect can not inhibit the measurement of Talbot length since the pixel size of the CCD camera is 6.45 μm, which is negligible compared to 1 mm (comparing y-axis and x-axis). On the other hand, Fig. 6.3 shows more clear Talbot carpets which is generated from amplitude grating (a part of Thorlabs R1S1L1N Negative Test Target). From the measured Talbot lengths, the effective

focal length, f_a' of the lens L_a using Eq. 6.6, have been derived for each grating period and tabulated in the Table 6.1 with respective errors.

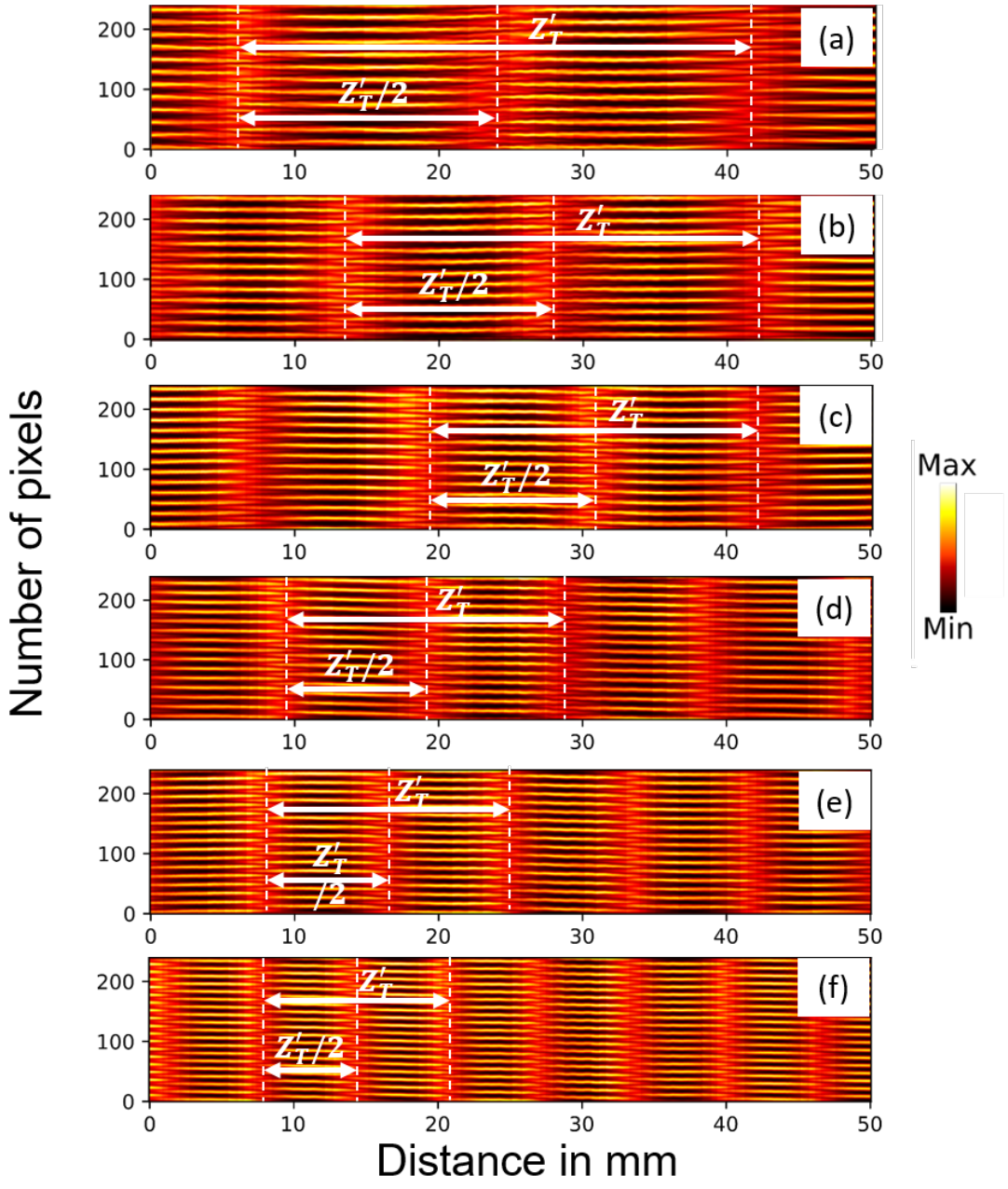

Figure 6.3: Experimental Talbot lengths for (a) 11.11 μm, (b) 10 μm, (c) 9.09 μm, (d) 8.33 μm, (e) 7.69 μm and (f) 6.67 μm grating periods

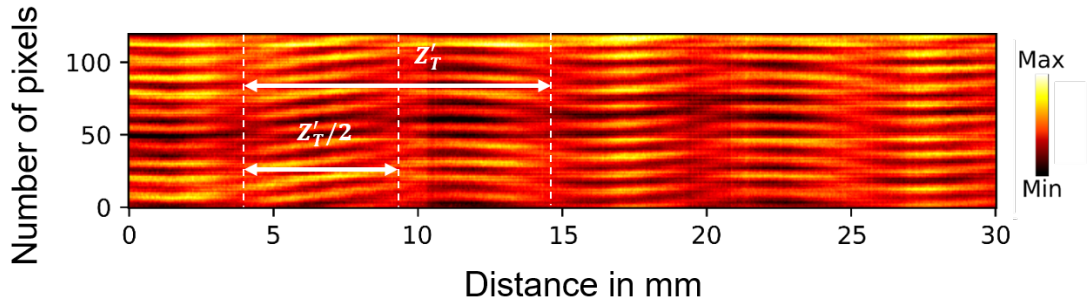

Figure 6.4: Experimental Talbot length for PPKTP crystal of 3.425 μm grating period

Table 6.1: Measured Talbot Lengths and Effective Focal Lengths for Different Grating Periods

Grating period, Λ (μm)	Talbot length, Z'_T (mm)	Effective focal length, f'_a (mm)
3.425	10.7	23.01 ± 0.22
6.67	12.3	25.14 ± 0.22
7.69	16.2	25.28 ± 0.18
8.33	18.7	25.45 ± 0.16
9.09	22.1	25.54 ± 0.14
10.00	26.9	25.50 ± 0.13
11.11	32.9	25.58 ± 0.11

The experimental values show a very good agreement with the theoretical plot as shown in the Fig. 6.5. The result confirms the aberration due to the lens, L_a. In this experiment we not only showed that a simple setup like $4f$ imaging, with significant magnification, allow us to produce magnified Talbot length at image plane to measure Talbot length accurately, but also brings out the effective change in focal length of the collecting lens due to spherical aberration. Using phase transfer function through a lens, we mathematically predicted a general form of the effective focal length, f'_a of a lens implemented in imaging non-paraxial Talbot regime, given by Eq. 6.4, and verified it using non-paraxial Talbot effect by a 1D grating of multiple grating periods. Note that the denominator of the effective focal length, f'_a given by Eq. 6.6, is modified similarly like the denominator of the non-paraxial Talbot length, given by Eq. 6.1,

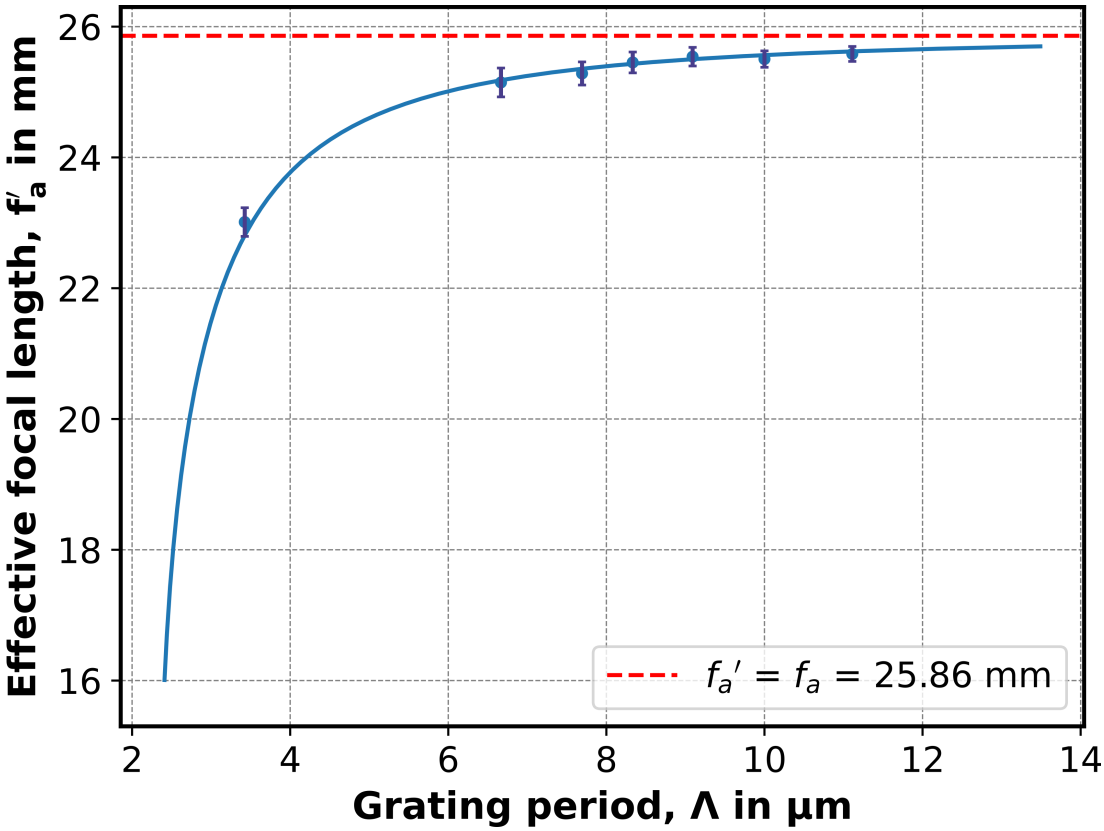

Figure 6.5: Experimentally measured effective focal length, f_a' is plotted against the grating period, Λ, comparing with the simulated curve

with the factor $\left(1-\sqrt{1-\frac{\lambda^2}{\Lambda^2}}\right)$. Thus, whenever we investigate non-paraxial Talbot domain with a $4f$ imaging-like set up, using any thick lens as collecting optics, we must take care of the aberration effect and modify our magnification factor accordingly.

6.4 Implications

The derived relation between effective focal length and grating period, validated through the non-paraxial Talbot effect, provides a novel optical method for characterizing spherical aberration in thick lenses. This approach offers a sensitive and experimentally accessible technique for lens diagnostics, with potential applications in optical system design, quality assurance in lens manufacturing, and advanced wave-

front sensing.

6.5 Conclusion

We have derived a mathematical expression for the effective focal length of a thick lens, specifically in the context of spherical aberration, by analyzing how this aberration affects the imaging of the non-paraxial Talbot effect. How the effective focal length of the thick lens vary with the the grating period, is given by the expression and the simulation is supported by our experiment. From the Talbot lengths for various known grating periods, we produced the effective focal length. The experimental data were then compared with the theoretical predictions, and the results confirmed that the calculated effective focal length corresponds closely to the focal lengths observed experimentally. This verification process not only validates the derived expression for the effective focal length but also emphasizes the significant influence of the non-paraxial Talbot effect on detecting spherical aberration in thick lenses.

Chapter 7

Summary and Future Scope

7.1 Summary

This thesis is mainly focused on producing a solution to placing Talbot planes at desired locations by introducing an architecture with tunable Talbot lengths, applicable both in linear and nonlinear processes and also applying this device for sensing applications. Sub-wavelength level variation in grating period has been measured using this technique. Also, Talbot effect has been extended to non-paraxial regime for sensing spherical aberration of a thick lens and to correct its focal length for imaging smaller grating periods.

In chapter 3, We developed the theoretical framework for a generic experimental setup, based on Fourier transform, to independently control the Talbot lengths of a periodic structure in a continuous manner, to overcome the stringent dependence on wavelength and grating period on the self-images. With a grating of period 25 μm, we have produced tunable Talbot lengths of a wide range from 1.97 mm to 49 mm,

hence, realizing a range up to 25 times greater than the original range. Some of the potential application areas of this generic architecture are Talbot lithography, Talbot-Lau interferometry and various other applications of metrology. Chapter 4 and chapter 5 are the extension of this architecture in the regimes of nonlinear second harmonic generation and its use as a sensing device for variation of grating periods respectively.

In chapter 4, we demonstrated single-pass second harmonic generation of the Talbot effect with significant conversion efficiency. We utilized a microlens array with 300 μm grating period as a two-dimensional periodic structure, illuminated by pump radiation at a wavelength of 1064 nm, and explored the single-pass upconversion of this periodic object using a 1.2-mm-long BiBO crystal. We first confirmed the doubling of the Talbot length in the upconversion (SHG) process. Then, we developed an experimental approach to achieve tunable Talbot lengths at both the pump and upconverted wavelengths, while simultaneously attaining significantly enhanced nonlinear conversion efficiency. We achieved it by using theory of Fourier Transform, particularly equating the spatial frequencies at the BiBO crystal plane at both pump and SHG wavelength. Our technique allowed for precise tuning of the Talbot planes at specific distances, facilitating the measurement of periodic objects with small pitch without the need for advanced microscopy. The highly efficient nonlinear upconversion of Talbot imaging demonstrated in this study shows potential applications in Talbot lithography and other high-energy scenarios involving the Talbot effect in both linear and nonlinear regimes.

In chapter 5, we produced a tunable Talbot length across a range of grating periods 18.2 μm to 19.7 μm with an increment of 300 nm, which allowed the sensor to detect periodicity variations as small as 450 nm for a grating period of 18.2 μm, utilizing a laser with a wavelength of 632.8 nm. We demonstrated the ability to operate in the sub-

wavelength regime without the need for microscopic systems. This sensing technique can be extended to other research areas requiring high-precision measurements with dynamic sensitivity.

In chapter 6, we used non-paraxial Talbot effect for sensing spherical aberration of a thick lens. We derived a mathematical expression for the effective focal length of a thick lens while imaging a grating period not very much greater than the wavelength of the laser. The expression describes how the effective focal length varies with the grating period, and our simulation is supported by experimental data. By measuring the Talbot lengths for various known grating periods, we calculated the effective focal length. Comparing the experimental data with theoretical predictions, we found that the calculated effective focal length closely matched the experimentally observed focal lengths. This verification process not only validates the derived expression for the effective focal length but also emphasizes the significant influence of the non-paraxial Talbot effect on detecting spherical aberration in thick lenses.

7.2 Future scope

While working on the Talbot effect in both the linear and nonlinear regimes, several potential future directions came to mind that require further exploration. Quantum Talbot imaging, Talbot propagation with vector beams, and superoscillation are three areas that deserve deeper investigation.

7.2.1 Quantum Talbot imaging

Quantum Talbot imaging has several potential future directions, particularly in areas where quantum interference and wavefront modulation play a crucial role. In quantum metrology, entangled photon sources can enhance precision measurements be-

yond classical limits. Quantum Talbot imaging may also advance quantum information processing by enabling more efficient quantum gate operations and secure communication protocols through multi-photon interference. Furthermore, the exploration of nonlocal and nonclassical imaging in quantum Talbot setups may revolutionize remote sensing and low-light imaging, opening new possibilities in biological imaging and other fields. Quantum ghost imaging is also a possible direction for Talbot effect. Researchers have already demonstrated several experiments of ghost imaging [110–112], although quantum ghost imaging of Talbot effect is still unexplored.

7.2.2 Talbot effect with vector beam

Near field diffraction is well understood by scalar diffraction theory, essentially Fresnel-Huygens principle derived from Helmholtz equation. In recent years, generation and manipulation of a vector beam in lab is quite feasible [113]. If a vector beam illuminates the grating, the electric field equation in near field can not be derived from scalar diffraction theory. Also, it will be interesting to know how the filed propagates with space and time while emerging from each grating slit, incorporating the vector nature of tyhe field. Illuminating a grating with a vector beam can give rise to several questions in near-field diffraction and also bring more clarity to fundamental physics overall.

7.2.3 Superoscillation

Through a simple imaging system, a grating period is much well resolved than any other object having the same dimension. This observation can be explained by superoscillation, a phenomenon where a wave oscillates faster than its highest Fourier component [114]. It offers promising future applications across various fields. In

super-resolution imaging, researchers have already shown that superoscillation has the potential to surpass the diffraction limit [83]. It can be further extended to enable nanometer-scale visualization of biological structures and nanomaterials. Also, in optical communications, superoscillatory signals may enhance data transmission density, improving system capacity. Near field diffraction of a periodic object has played a pivotal role to understand and applications of superoscillation [105, 115]. One important future aspect of Talbot effect could be to understand the exotic phenomenon like superoscillation in more depth.

List of Publications

(Thesis related Publications)

Published

1. Harshith Bachimanchi, **Saumya J. Sarkar**, M. Ebrahim-Zadeh, and G. K. Samanta, "Harnessing nonlinear frequency upconversion of Talbot effect with flexible Talbot lengths", Opt. Express **32**, 15967-15977 (2024)
   DOI: https://doi.org/10.1364/OE.518005

2. **Saumya J. Sarkar**, M. Ebrahim-Zadeh, and G. K. Samanta, "Talbot effect based sensor measuring grating period change in subwavelength range", *Sci Rep* **14**, 30872 (2024).
   DOI: https://doi.org/10.1038/s41598-024-81722-2

Bibliography

[1] E. Hecht, *Optics* (Pearson, 2012).

[2] F. M. Grimaldi, *Physico-mathesis de lumine, coloribus et iride* (Victorii Benatii, 1966).

[3] C. Huygens, *Traité de la lumière* (Gressner & Schramm, 1885).

[4] I. Newton, *Opticks, or, a treatise of the reflections, refractions, inflections & colours of light* (Courier Corporation, 1952).

[5] T. Young, *Ii. the bakerian lecture. on the theory of light and colours,* Philosophical transactions of the Royal Society of London pp. 12–48 (1802).

[6] G.-A. Boutry, *Augustin fresnel: his time, life and work, 1788-1827,* Science Progress (1933-) **36**, 587–604 (1948).

[7] M. Born and E. Wolf, *Principles of optics: electromagnetic theory of propagation, interference and diffraction of light* (Elsevier, 2013).

[8] J. Worrall, *Fresnel, poisson and the white spot: The role of successful predictions in the acceptance of scientific theories,* The uses of experiment pp. 135–157 (1989).

[9] H. F. Talbot, *Facts relating to optical science,* Philos. Mag. **9**, 401–407 (1836).

[10] J. W. Goodman, *Introduction to Fourier optics* (Roberts and Company publishers, 2005).

[11] A. Leitner, *The life and work of Joseph Fraunhofer (17871826),* American Journal of Physics **43**, 59–68 (1975).

[12] J. C. Maxwell, *Viii. a dynamical theory of the electromagnetic field,* Philosophical transactions of the Royal Society of London pp. 459–512 (1865).

[13] C. Davisson and L. H. Germer, *The scattering of electrons by a single crystal of nickel,* Nature **119**, 558–560 (1927).

[14] W. H. Bragg and W. L. Bragg, *The reflection of x-rays by crystals,* Proceedings of the Royal Society of London. Series A, Containing Papers of a Mathematical and Physical Character **88**, 428–438 (1913).

[15] B. Fultz and J. M. Howe, *Transmission electron microscopy and diffractometry of materials* (Springer Science & Business Media, 2012).

[16] Y. A. Izyumov, *Magnetic neutron diffraction* (Springer Science & Business Media, 2012).

[17] D. Gabor, *A new microscopic principle.* (1948).

[18] S. A. Maier *et al.*, *Plasmonics: fundamentals and applications*, vol. 1 (Springer, 2007).

[19] N. I. Zheludev and Y. S. Kivshar, *From metamaterials to metadevices,* Nature materials **11**, 917–924 (2012).

[20] J. D. Joannopoulos, P. R. Villeneuve, and S. Fan, *Photonic crystals,* Solid State Communications **102**, 165–173 (1997).

[21] T. Ozawa, H. M. Price, A. Amo, N. Goldman, M. Hafezi, L. Lu, M. C. Rechtsman, D. Schuster, J. Simon, O. Zilberberg *et al.*, *Topological photonics,* Reviews of Modern Physics **91**, 015006 (2019).

[22] L. Rayleigh, *Xxv. on copying diffraction-gratings, and on some phenomena connected therewith,* The London, Edinburgh, and Dublin Philosophical Magazine and Journal of Science **11**, 196–205 (1881).

[23] J. Wen, Y. Zhang, and M. Xiao, *The talbot effect: recent advances in classical optics, nonlinear optics, and quantum optics,* Advances in optics and photonics **5**, 83–130 (2013).

[24] K. Patorski, *I the self-imaging phenomenon and its applications,* Progress in optics **27**, 1–108 (1989).

[25] A. Winkelmann, *Über einige erscheinungen, die bei der beugung des lichtes durch gitter auftreten,* Annalen der Physik **332**, 905–954 (1908).

[26] H. Weisel, *Über die nach Fresnelscher Art beobachteten Beugungserscheinungen der Gitter* (Christ & Herr, 1910).

[27] M. Wolfke, *Über die abbildung eines gitters außerhalb der einstellebene,* Annalen der Physik **345**, 194–200 (1913).

[28] J. Cowley and A. Moodie, *Fourier images iv: the phase grating,* Proceedings of the Physical Society **76**, 378 (1960).

[29] J. Cowley and A. Moodie, *Fourier images: I-the point source,* Proceedings of the Physical Society. Section B **70**, 486 (1957).

[30] J. Cowley and A. Moodie, *Fourier images: Ii-the out-of-focus patterns,* Proceedings of the Physical Society. Section B **70**, 497 (1957).

[31] J. Cowley and A. Moodie, *Fourier images: Iii-finite sources,* Proceedings of the Physical Society. Section B **70**, 505 (1957).

[32] W. D. Montgomery, *Self-imaging objects of infinite aperture,* JOSA **57**, 772–778 (1967).

[33] M. Testorf and J. Ojeda-Castañeda, *Fractional talbot effect: analysis in phase space,* JOSA A **13**, 119–125 (1996).

[34] C.-S. Guo, X. Yin, L.-W. Zhu, and Z.-P. Hong, *Analytical expression for phase distribution of a hexagonal array at fractional talbot planes,* Optics letters **32**, 2079–2081 (2007).

[35] M. V. Berry and S. Klein, *Integer, fractional and fractal talbot effects,* Journal of modern optics **43**, 2139–2164 (1996).

[36] K. Pelka, J. Graf, T. Mehringer, and J. von Zanthier, *Prime number decomposition using the talbot effect,* Optics Express **26**, 15009–15014 (2018).

[37] M. Testorf, *Designing talbot array illuminators with phase-space optics,* JOSA A **23**, 187–192 (2006).

[38] T. Jannson and J. Jannson, *Temporal self-imaging effect in single-mode fibers,* JOSA **71**, 1373–1376 (1981).

[39] F. Mitschke and U. Morgner, *The temporal talbot effect,* Optics and Photonics News **9**, 45–47 (1998).

[40] J. Azaña, *Spectral talbot phenomena of frequency combs induced by cross-phase modulation in optical fibers,* Optics letters **30**, 227–229 (2005).

[41] J. A. Bolger, P. Hu, J. T. Mok, J. L. Blows, and B. J. Eggleton, *Talbot self-imaging and cross-phase modulation for generation of tunable high repetition rate pulse trains,* Optics communications **249**, 431–439 (2005).

[42] L. A. Hall, M. Yessenov, S. A. Ponomarenko, and A. F. Abouraddy, *The space–time talbot effect,* APL Photonics **6** (2021).

[43] A. Momose, S. Kawamoto, I. Koyama, Y. Hamaishi, K. Takai, and Y. Suzuki, *Demonstration of x-ray talbot interferometry,* Japanese journal of applied physics **42**, L866 (2003).

[44] A. Momose, W. Yashiro, Y. Takeda, Y. Suzuki, and T. Hattori, *Phase tomography by x-ray talbot interferometry for biological imaging,* Japanese journal of applied physics **45**, 5254 (2006).

[45] P. Cloetens, J. Guigay, C. De Martino, J. Baruchel, and M. Schlenker, *Fractional talbot imaging of phase gratings with hard x rays,* Optics letters **22**, 1059–1061 (1997).

[46] C. David, B. Nöhammer, H. Solak, and E. Ziegler, *Differential x-ray phase contrast imaging using a shearing interferometer,* Applied physics letters **81**, 3287–3289 (2002).

[47] T. Weitkamp, B. Nöhammer, A. Diaz, C. David, and E. Ziegler, *X-ray wavefront analysis and optics characterization with a grating interferometer,* Applied Physics Letters **86** (2005).

[48] M. S. Chapman, C. R. Ekstrom, T. D. Hammond, R. A. Rubenstein, J. Schmiedmayer, S. Wehinger, and D. E. Pritchard, *Optics and interferometry with na 2 molecules,* Physical review letters **74**, 4783 (1995).

[49] L. Deng, E. W. Hagley, J. Denschlag, J. Simsarian, M. Edwards, C. W. Clark, K. Helmerson, S. Rolston, and W. D. Phillips, *Temporal, matter-wave-dispersion talbot effect,* Physical Review Letters **83**, 5407 (1999).

[50] B. Brezger, L. Hackermüller, S. Uttenthaler, J. Petschinka, M. Arndt, and A. Zeilinger, *Matter-wave interferometer for large molecules,* Physical review letters **88**, 100404 (2002).

[51] P.-M. Coulon, B. Damilano, B. Alloing, P. Chausse, S. Walde, J. Enslin, R. Armstrong, S. Vézian, S. Hagedorn, T. Wernicke *et al.*, *Displacement talbot lithography for nano-engineering of iii-nitride materials,* Microsystems & Nanoengineering **5**, 52 (2019).

[52] Z. Zhang, Y. Feng, S. Ning, G. Malpuech, D. Solnyshkov, Z. Xu, Y. Zhang, and M. Xiao, *Imaging lattice switching with talbot effect in reconfigurable non-hermitian photonic graphene,* Photonics research **10**, 958–964 (2022).

[53] W. Zhang, C. Zhao, J. Wang, and J. Zhang, *An experimental study of the plasmonic talbot effect,* Optics express **17**, 19757–19762 (2009).

[54] S. Cherukulappurath, D. Heinis, J. Cesario, N. F. van Hulst, S. Enoch, and R. Quidant, *Local observation of plasmon focusing in talbot carpets,* Optics express **17**, 23772–23784 (2009).

[55] T. Gao, E. Estrecho, G. Li, O. A. Egorov, X. Ma, K. Winkler, M. Kamp, C. Schneider, S. Hoefling, A. Truscott *et al.*, *Talbot effect for exciton polaritons,* Physical Review Letters **117**, 097403 (2016).

[56] W. Zhao, X. Huang, and Z. Lu, *Super talbot effect in indefinite metamaterial,* Optics Express **19**, 15297–15303 (2011).

[57] R. W. Boyd, A. L. Gaeta, and E. Giese, *Nonlinear optics,* in "Springer Handbook of Atomic, Molecular, and Optical Physics," (Springer, 2008), pp. 1097–1110.

[58] Y. Zhang, J. Wen, S. Zhu, and M. Xiao, *Nonlinear talbot effect,* Physical Review Letters **104**, 183901 (2010).

[59] Z. Chen, D. Liu, Y. Zhang, J. Wen, S. Zhu, and M. Xiao, *Fractional second-harmonic talbot effect,* Optics Letters **37**, 689–691 (2012).

[60] L. Li, H. Liu, and X. Chen, *Dynamic manipulation of nonlinear talbot effect with structured light,* Optics Letters **46**, 1281–1284 (2021).

[61] U. Bortolozzo, S. Residori, and J. Huignard, *Enhancement of the two-wave-mixing gain in a stack of thin nonlinear media by use of the talbot effect,* Optics letters **31**, 2166–2168 (2006).

[62] M. Berry, I. Marzoli, and W. Schleich, *Quantum carpets, carpets of light,* Physics World **14**, 39 (2001).

[63] K.-H. Luo, J. Wen, X.-H. Chen, Q. Liu, M. Xiao, and L.-A. Wu, *Second-order talbot effect with entangled photon pairs,* Physical Review A—Atomic, Molecular, and Optical Physics **80**, 043820 (2009).

[64] C. R. Ooi and B. L. Lan, *Intense nonclassical light: controllable two-photon talbot effect,* Physical Review A—Atomic, Molecular, and Optical Physics **81**, 063832 (2010).

[65] V. Torres-Company, J. Lancis, H. Lajunen, and A. T. Friberg, *Coherence revivals in two-photon frequency combs,* Physical Review A—Atomic, Molecular, and Optical Physics **84**, 033830 (2011).

[66] E. Poem and Y. Silberberg, *Photon correlations in multimode waveguides,* Physical Review A—Atomic, Molecular, and Optical Physics **84**, 041805 (2011).

[67] X.-B. Song, H.-B. Wang, J. Xiong, K. Wang, X. Zhang, K.-H. Luo, and L.-A. Wu, *Experimental observation of quantum talbot effects,* Physical Review Letters **107**, 033902 (2011).

[68] J. Wen, S. Du, H. Chen, and M. Xiao, *Electromagnetically induced talbot effect,* Applied Physics Letters **98** (2011).

[69] P. Berglund, A. Geraci, T. Hübsch, D. Mattingly, and D. Minic, *Triple interference, non-linear talbot effect and gravitization of the quantum,* Classical and Quantum Gravity **40**, 155008 (2023).

[70] Y. Nakano and K. Murata, *Talbot interferometry for measuring the small tilt angle variation of an object surface,* Applied optics **25**, 2475–2477 (1986).

[71] A. Wang, P. Gill, and A. Molnar, *Light field image sensors based on the talbot effect,* Applied optics **48**, 5897–5905 (2009).

[72] E. Ye, A. H. Atabaki, N. Han, and R. J. Ram, *Miniature, sub-nanometer resolution talbot spectrometer,* Optics Letters **41**, 2434–2437 (2016).

[73] P. Franken, A. E. Hill, C. e. Peters, and G. Weinreich, *Generation of optical harmonics,* Physical review letters **7**, 118 (1961).

[74] T. Maiman, *Stimulated optical radiation in ruby,* SPIE milestone series pp. 61–61 (2002).

[75] B. S. Harshith and G. K. Samanta, *Controlled generation of array beams of higher order orbital angular momentum and study of their frequency-doubling characteristics,* Scientific Reports **9**, 10916 (2019).

[76] M. Jabir, N. Apurv Chaitanya, A. Aadhi, and G. K. Samanta, *Generation of "perfect" vortex of variable size and its effect in angular spectrum of the down-converted photons,* Scientific Reports **6**, 21877 (2016).

[77] L. S. Brea, *Diffractio, python module for diffraction and interference optics,* (2019).

[78] J. Liang, B. Grimm, S. Goelz, and J. F. Bille, *Objective measurement of wave aberrations of the human eye with the use of a Hartmann–Shack wave-front sensor,* JOSA A **11**, 1949–1957 (1994).

[79] L. Martínez-León, M. Araiza-E, B. Javidi, P. Andrés, V. Climent, J. Lancis, and E. Tajahuerce, *Single-shot digital holography by use of the fractional Talbot effect,* Optics Express **17**, 12900–12909 (2009).

[80] A. Camino, Z. Hao, X. Liu, and J. Lin, *High spectral power femtosecond supercontinuum source by use of microlens array,* Optics Letters **39**, 747–750 (2014).

[81] T. Xi, Z. Zhao, and Z. Hao, *Femtosecond laser filamentation with a microlens array in air,* JOSA B **32**, 163–166 (2015).

[82] M. Berry and S. Popescu, *Evolution of quantum superoscillations and optical superresolution without evanescent waves,* Journal of Physics A: Mathematical and General **39**, 6965 (2006).

[83] E. T. Rogers, J. Lindberg, T. Roy, S. Savo, J. E. Chad, M. R. Dennis, and N. I. Zheludev, *A super-oscillatory lens optical microscope for subwavelength imaging,* Nature Materials **11**, 432–435 (2012).

[84] J. Wen, Y. Zhang, and M. Xiao, *The Talbot effect: recent advances in classical optics, nonlinear optics, and quantum optics,* Adv. Opt. Photon. **5**, 83–130 (2013).

[85] H. Chen, X. Zhang, D. Zhu, C. Yang, T. Jiang, H. Zheng, and Y. Zhang, *Dressed four-wave mixing second-order Talbot effect,* Phys. Rev. A **90**, 043846 (2014).

[86] Y. Zhang, M. R. Belić, H. Zheng, H. Chen, C. Li, J. Song, and Y. Zhang, *Nonlinear talbot effect of rogue waves,* Physical Review E **89**, 032902 (2014).

[87] R. Schiek, *Excitation of nonlinear beams: from the linear talbot effect through modulation instability to akhmediev breathers,* Optics express **29**, 15830–15851 (2021).

[88] G. G. Rozenman, W. P. Schleich, L. Shemer, and A. Arie, *Periodic wave trains in nonlinear media: Talbot revivals, akhmediev breathers, and asymmetry breaking,* Physical Review Letters **128**, 214101 (2022).

[89] Z. Zhang, Y. Feng, S. Ning, G. Malpuech, D. D. Solnyshkov, Z. Xu, Y. Zhang, and M. Xiao, *Imaging lattice switching with Talbot effect in reconfigurable non-Hermitian photonic graphene,* Photon. Res. **10**, 958–964 (2022).

[90] E. Bonet, P. Andrés, J. Barreiro, and A. Pons, *Self-imaging properties of a periodic microlens array: versatile array illuminator realization,* Optics Communications **106**, 39–44 (1994).

[91] B. Besold and N. Lindlein, *Practical limitations of Talbot imaging with microlens arrays,* Pure and Applied Optics: Journal of the European Optical Society Part A **6**, 691 (1997).

[92] Y. Takeda, W. Yashiro, T. Hattori, A. Takeuchi, Y. Suzuki, and A. Momose, *Differential phase X-ray imaging microscopy with X-ray Talbot interferometer,* Applied Physics Express **1**, 117002 (2008).

[93] S. Pang, C. Han, M. Kato, P. W. Sternberg, and C. Yang, *Wide and scalable field-of-view Talbot-grid-based fluorescence microscopy,* Optics Letters **37**, 5018–5020 (2012).

[94] H. F. Talbot, *Facts relating to optical science,* Philosophical Magazine and Journal of Science **9**, 401–407 (1836).

[95] A. Aadhi and G. K. Samanta, *High power, high repetition rate, tunable broadband mid-IR source based on single-pass optical parametric generation of a femtosecond laser,* Opt. Lett. **42**, 2886–2889 (2017).

[96] N. A. Chaitanya, A. Aadhi, M. Jabir, and G. K. Samanta, *Frequency-doubling characteristics of high-power, ultrafast vortex beams,* Optics Letters **40**, 2614–2617 (2015).

[97] S. Teng, N. Zhang, Q. Dong, and C. Cheng, *Diffraction of a one-dimensional phase grating in the deep Fresnel field,* JOSA A **24**, 3636–3643 (2007).

[98] P. Rodriguez-Montero, D. S. de-la Llave, and S. Mansurova, *Electro-optical processor for measuring displacement employing the talbot and the nonsteady-state photo-electromotive force effects,* Opt. Lett. **39**, 104–107 (2014).

[99] H. L. Kung, A. Bhatnagar, and D. A. Miller, *Transform spectrometer based on measuring the periodicity of talbot self-images,* Optics letters **26**, 1645–1647 (2001).

[100] P. Ferraro, G. Coppola, D. Alfieri, S. D. Nicola, S. Grilli, A. Finizio, and G. Pierattini, *A novel interferometric spectrometer obtained by imaging Talbot effect in digital holography,* in "Optical Metrology in Production Engineering," , vol. 5457, W. Osten and M. Takeda, eds., International Society for Optics and Photonics (SPIE, 2004), vol. 5457, pp. 651 – 659.

[101] I.-L. Ho and Y.-C. Chang, *Multiscale talbot effects in fibonacci geometry,* Journal of Optics **17**, 045601 (2015).

[102] L. Martínez-León, M. Araiza-E, B. Javidi, P. Andrés, V. Climent, J. Lancis, and E. Tajahuerce, *Parallel phase-shifting digital holography based on the fractional talbot effect,* Journal of Physics: Conference Series **206**, 012023 (2010).

[103] G. S. Spagnolo and D. Ambrosini, *Talbot effect application: measurement of distance with a fourier-transform method,* Measurement Science and Technology **11**, 77 (2000).

[104] D. F. Sunday, S. List, J. S. Chawla, and R. J. Kline, *Determining the shape and periodicity of nanostructures using small-angle x-ray scattering,* Journal of Applied Crystallography **48**, 1355–1363 (2015).

[105] F. M. Huang, N. Zheludev, Y. Chen, and F. Javier Garcia de Abajo, *Focusing of light by a nanohole array,* Applied Physics Letters **90** (2007).

[106] Y. Hua, J. Y. Suh, W. Zhou, M. D. Huntington, and T. W. Odom, *Talbot effect beyond the paraxial limit at optical frequencies,* Optics express **20**, 14284–14291 (2012).

[107] R. Sekine, T. Shibuya, K. Ukai, S. Komatsu, M. Hattori, T. Mihashi, N. Nakazawa, and Y. Hirohara, *Measurement of wavefront aberration of human eye using talbot image of two-dimensional grating,* Optical review **13**, 207–211 (2006).

[108] D. V. Podanchuk, A. A. Goloborodko, M. M. Kotov, A. V. Kovalenko, V. N. Kurashov, and V. P. Dan'ko, *Adaptive wavefront sensor based on the talbot phenomenon,* Applied optics **55**, B150–B157 (2016).

[109] J. D. Ring, J. Lindberg, C. J. Howls, and M. R. Dennis, *Aberration-like cusped focusing in the post-paraxial talbot effect,* Journal of Optics **14**, 075702 (2012).

[110] R. S. Aspden, *Heralded quantum imaging,* Ph.D. thesis, University of Glasgow (2015).

[111] P.-A. Moreau, E. Toninelli, T. Gregory, R. S. Aspden, P. A. Morris, and M. J. Padgett, *Imaging bell-type nonlocal behavior,* Science Advances **5**, eaaw2563 (2019).

[112] C. Moodley and A. Forbes, *Super-resolved quantum ghost imaging,* Scientific Reports **12**, 10346 (2022).

[113] C. Rosales-Guzmán, B. Ndagano, and A. Forbes, *A review of complex vector light fields and their applications,* Journal of Optics **20**, 123001 (2018).

[114] M. Berry, *Faster than fourier,* Quantum Coherence and Reality pp. 55–65 (1994).

[115] F. M. Huang, Y. Chen, F. J. G. De Abajo, and N. I. Zheludev, *Optical super-resolution through super-oscillations,* Journal of Optics A: Pure and Applied Optics **9**, S285 (2007).